

CENPA

Center for Experimental Nuclear Physics and Astrophysics



Annual Report 2023

University of Washington

CENPA ANNUAL REPORT 2023

Center for Experimental Nuclear Physics and Astrophysics
University of Washington
October 1, 2023

Sponsored in part by the United States Department of Energy
under Grant #DE-FG02-97ER41020.

This report was prepared as an account of work sponsored in part by the United States Government. Neither the United States nor the United States Department of Energy, nor any of their employees, makes any warranty, expressed or implied or assumes any legal liability or responsibility for accuracy, completeness or usefulness of any information, apparatus, product or process disclosed, or represents that its use would not infringe on privately-owned rights.

Cover: All photos courtesy of David Hertzog, Director. *Left:* Svende Braun setting up for the CENPA test-beam run to test Low-Gain Avalanche Diodes (LGADs) as R&D for the PIONEER experiment. *Top right:* Eric Smith calibrating beam for the PIONEER LGADs with student research assistants Arif Chu, Alex Morgan, and Anthony McKeirnan. *Bottom right:* Michael Huehn working on the CCA (Cavity CRES Apparatus) insert and vacuum chamber CAD design and simulations for Project 8.

FOREWORD

We are delighted to be preparing this Annual Report with the laboratory, the university, and basically all of life feeling somewhat back to normal. CENPA science has been proceeding vigorously, experiments are having great successes, students are defending theses, and the technical staff is continuing to display exceptional talent. In this Annual Report, you will see a snapshot of the latest findings and the detailed project individuals and groups are engaged in at the moment. Please enjoy.

-- David Hertzog, Director of CENPA --

CENPA Group Photo 2023



Back Row (Standing)

Sevende Braun, Joshua LaBounty, Brynn MacCoy, Peter Wu, Ian Paulson, Joshua LaBounty, Michaelangelo Traina, Blake Maxwell, David Peterson, Patrick Schwendimann, Heng Lin, Dan Zhang

Back 2nd Row (Standing)

Gray Rybka, Ryan Roehnell, Nate Midema, Sanshiro Enomoto, Louis Varriano, Sabrina Cheng, Joshua LaBounty, Tim Van Wechel, Christian Nave, Harry Ni, Nicole Nishihama, Gary Holman, Eric Smith, Yasin Chowdhury, Alex Morgan

Seated 3rd Row

Omar Beesley, Brittney Dodson, Heather Harrington, Alexander Marsteller, Christine Claessens, James Sinnis, Matt Kallander, Paul Kolbeck, Caleb Landsdell, Michael Ross, Erik Shaw

Seated 2nd Row

Meg Wynne, Clinton Wiseman, Hamish Robertson, Elise Novitski, David Hertzog, Erik Swanson, Luciano Malavasi, Audrey Cole, Conner Gettings, Shoshana Apple

1st Row

Michaela Guzzetti, Anthony McKeirnan, Alvaro Chavarria, Jens Gundlach, Alejandro Garcia, Arif Chu, Charles Hanretty, Cyrus Goodman, Peter Park

INTRODUCTION

The Nuclear Physics Lab at the University of Washington was established 1948. In 1998, it evolved into CENPA, the Center for Experimental Nuclear Physics and Astrophysics. CENPA is the institutional home for a broad program of research in nuclear physics and related fields. Research activities — with an emphasis on fundamental symmetries and neutrinos — are conducted locally and at remote sites. In neutrino physics, three experiments are related to measuring its mass. CENPA is the lead US institution in the KATRIN tritium beta decay experiment, the important and recently complete supportive local tritium decay experiment TRIMS, and the site for experimental work on Project 8. We also study neutrinoless double beta decay as a collaborating institution in the ^{76}Ge based LEGEND experiments, which derives from our extensive experience in the recently completed MAJORANA effort. Looking beyond the ton scale, we are exploring a next-generation R&D effort with the SELENA experiment. Finally, our neutrino group is involved in the COHERENT neutrino-nucleus scattering experiment. The Muon Physics group developed and completed the MuSun experiment to measure muon capture in deuterium at the Paul Scherrer Institute in Switzerland. A major focus of our group has been the high-precision measurement of the muon’s anomalous magnetic moment at Fermilab. The first results were reported in April 2021 and the latest 2023 results are discussed in this report. Much of this group’s attention has begun to be focused on the new PIONEER experiment that will measure lepton flavor universality to unprecedented levels in its first phase of rare pion decay studies. Our local fundamental symmetries program also includes an experiment using the local Tandem Van de Graaff accelerator to measure the Fierz interference in ^6He decay, using the CRES technique that was developed by Project 8.

In addition to the research directly supported by DOE’s Office of Nuclear Physics through the CENPA core grant, other important programs are located at CENPA, forming a broader intellectual center with valuable synergies. The “Gravity” group carries out, with both DOE and NSF support, studies of the weak and strong Equivalence Principles, fundamental precepts of General Relativity, as well as searches for non-Newtonian forces such as those predicted by theories with extra dimensions. In addition, they participate in LIGO with unique instrumentation that aids the functioning and stabilization of the interferometers. The DOE Office of High Energy Physics supports the unique ADMX axion search experiment. The NSF supports the DAMIC experiment that looks for light dark matter.

CENPA is home to a large number of faculty, research faculty, postdoctoral scholars, graduate, and undergraduate students. The core professional engineering and technical staff provide diverse capabilities and skills such as state-of-the-art detector development, fabrication of custom electronics, large-scale computing, and design engineering. New advancements, capabilities, and ideas are regularly shared at seminars by CENPA members and visitors alike. In Summer, 2022, the particle physics community came to our campus for the Snowmass process. Given our concentration in fundamental physics and neutrinos, many CENPA faculty were involved in the organization of relevant subtopics and provided talks and contributions to the reports. High-energy physicists from across the nation toured CENPA as part of the 10-day-long event. Elise Novitski contributed significantly to the event by serving as Accessibility Coordinator for the Local Organizing Committee of Snowmass 23.

0.1 Personnel updates

David Hertzog was selected to give the 2022 University of Washington Faculty Lecture.

Robertson Fellow Elise Novitski was selected as Research Assistant Professor at UW and took up her new position in September 2022. She leads the experimental coordination of the Project 8 Collaboration. As of this writing, Elise has been offered and has accepted a tenure-track Assistant Professorship in the Department and will begin her new role in September 2023.

Research Professor Peter Doe, Research Scientist Duncan Prindle, and machine shop manager Tom Burritt each retired in 2023. We owe them immeasurable thanks for decades of outstanding research, technical and computational developments, and for serving the mission of CENPA so well. They will be sorely missed.

Nicole Nishihama is our new Fiscal Specialist II. She works closely with Associate Director Gary Holman to keep the lab running in many dimensions, from fiscal to event planning, to facility maintenance.

Several postdoctoral scholars have left since the last Annual Report. They include Chelsea Bartram (ADMX), now at SLAC with a Panofsky Fellowship; Brent Graner (He-6), now at Nion; Tatsumi Nitta (ADMX), now a Research Professor at the University of Tokyo; Zach Hodge (Muon g-2), now a government scientist.

New postdoctoral scholars arriving in since the last Annual Report include Svende Braun (Muon / PIONEER), Nick Buzinsky (He-6), Heng Lin (DAMIC/Selena), Alexander Marsteller (Project 8 / KATRIN); Patrick Schwendimann (PIONEER), Erik Shaw (Gravity), Michelangelo Traina (DAMIC/Selena), Louis Varriano (LEGEND), Dan Zhang (ADMX). Recent graduates Brynn MacCoy (Muon) and Erik Shaw (Gravity) will continue as short-term postdoctoral scholars to complete important studies they initiated.

Since the last Annual Report, these CENPA graduate students completed their Ph.D. degrees: Hannah Binney (Muon g-2), Alex Hostiuc (MAJORANA), Brynn MacCoy (Muon g-2), Ethan Muldoon (MuSun), Alex Piers (DAMIC/Selena), Nick Ruof (MAJORANA / LEGEND), and Erik Shaw (Gravity)

0.2 Recent Accomplishments

- Following the publication in Nature Physics last year reporting the first sub-eV sensitivity measurement of the neutrino mass using the first two “campaign” data, KATRIN has continued the accumulation of statistics, completing the ninth campaign as of May 2023. The dataset up to the fifth campaign was unblinded, and the results will be released in the summer of 2023. The UW group processed all the raw data into fitting-ready spectra and distributed them to the collaboration, and constructed a detailed detector response model at 0.1% level accuracy.
- Project 8 has completed Phase II of its program toward a direct measurement of neutrino mass at the 40-meV sensitivity level. The analysis, in which CENPA played a

major role, of the first tritium spectrum taken with the Cyclotron Radiation Emission Spectroscopy (CRES) method was novel and complex, and has been summarized in a paper accepted by Phys. Rev. Lett. A companion 40-page paper has been submitted to Phys. Rev. C. The results show good agreement of the neutrino mass limit and the endpoint energy with literature values, and zero background events in 82 days of running.

- MAJORANA published “final results” on $0\nu\beta\beta$ decay in PRL in Feb. 2023; first results on our ^{180}mTa search have been submitted for publication.
- The LEGEND-200 apparatus has begun data taking at Gran Sasso, and its subsequent ton-scale phase LEGEND-1000 is preparing for CD1 in 2024.
- The Muon g-2 Experiment completed its 6-year data taking campaign, accumulating > 21 times the data that was obtained at BNL, thus exceeding its proposal goals. More than 1600 citations have been made to the papers reporting our first results published in April 2021. In August 2023 we released our Run-2/3 result that re-confirmed Run1, with halved uncertainty. (see articles in this report).
- In the PhD. thesis of Ethan Muldoon (June 2023) systematic effects in the MuSun experiment were comprehensively evaluated with uncertainties close to the proposal goal.
- The PIONEER Experiment to measure rare pion decays has been approved with high priority at the Paul Scherrer Institute. Our first beam time was used to develop tunes and measure pion flux. Significant hardware R&D is being carried out at CENPA and by collaborating partners across the world. We are presently using Rutherford back-scattering at CENPA to test ATAR prototype samples, and we are further preparing a LYSO calorimeter array for measurements at PSI in November 2023.
- Using Cyclotron Radiation Electron Spectroscopy (CRES) the He6-CRES experiment demonstrated detection of β^\pm from ^6He and ^{19}Ne with energies in the 5 keV to 2.3 MeV range. This sets the collaboration on their path to use CRES for sensitive searches of chirality-flipping interactions.
- The DAMIC group released results from its two CCD detectors operating underground at SNOLAB and Modane Lab, including world-leading constraints on sub-GeV dark matter particles scattering with electrons. The prototyping of the upcoming, 100x more sensitive DAMIC-M detector proceeds at CENPA.
- The Selena program continues its R&D toward a next-generation search for neutrino-less $\beta\beta$ decay. The first prototype CMOS sensors optimized for charge collection in amorphous selenium were successfully designed at CENPA and fabricated by Efabless.
- ADMX operated with sensitivity to DFSZ axions within the 800 MHz to 1020 MHz range, with one results paper published and another pending. Operations continue moving to higher frequency ranges. The Orpheus hidden photon search released the first results from a multi-wavelength haloscope, excluding new parameter space.

- CENPA also hosts a long-standing program in “tabletop gravity” using extraordinarily sensitive torsion balance pendulums to search for physics beyond the Standard Model and General Relativity. The group also conducts a torsion balance search for ultra-light dark matter. The group is also involved in developing technology to improve gravitational wave detection with LIGO.

As always, we encourage outside applications for the use of our facilities. As a convenient reference for potential users, the table on the following page lists the capabilities of our accelerators. For further information, please contact Gary Holman, Associate Director (holman@uw.edu) or Eric Smith, Research Engineer (esmith66@u.washington.edu) CENPA, Box 354290, University of Washington, Seattle, WA 98195; (206) 543 4080. Further information is also available on our web page: <http://www.npl.washington.edu>.

We close this introduction with a reminder that the articles in this report describe work in progress and are not to be regarded as publications nor to be quoted without permission of the authors. In each article the names of the investigators are listed alphabetically, with the primary author underlined in the case of multiple authors, to whom inquiries should be addressed.

David Hertzog, Director

Gary Holman, Associate Director and Editor

TANDEM VAN DE GRAAFF ACCELERATOR

Our tandem accelerator facility is centered around a High Voltage Engineering Corporation Model FN purchased in 1966 with NSF funds, with operation funded primarily by the U.S. Department of Energy. See W. G. Weitkamp and F. H. Schmidt, "The University of Washington Three Stage Van de Graaff Accelerator," *Nucl. Instrum. Methods* **122**, 65 (1974). The tandem was adapted in 1996 to an (optional) terminal ion source and a non-inclined tube #3, which enables the accelerator to produce high intensity beams of hydrogen and helium isotopes at energies from 100 keV to 7.5 MeV.

Some Available Energy Analyzed Beams

Ion	Max. Current (particle μA)	Max. Energy (MeV)	Ion Source
^1H or ^2H	50	18	DEIS or 860
^3He or ^4He	2	27	Double Charge-Exchange Source
^3He or ^4He	30	7.5	Tandem Terminal Source
^6Li or ^7Li	1	36	860
^{11}B	5	54	860
^{12}C or ^{13}C	10	63	860
$^{*14}\text{N}$	1	63	DEIS or 860
^{16}O or ^{18}O	10	72	DEIS or 860
F	10	72	DEIS or 860
* Ca	0.5	99	860
Ni	0.2	99	860
I	0.001	108	860

*Negative ion is the hydride, dihydride, or trihydride.

Several additional ion species are available including the following: Mg, Al, Si, P, S, Cl, Fe, Cu, Ge, Se, Br and Ag. Less common isotopes are generated from enriched material. We recently have been producing the positive ion beams of the noble gases He, Ne, Ar, and Kr at ion source energies from 10 keV to 100 keV for implantation, in particular the rare isotopes ^{21}Ne and ^{36}Ar . We have also produced a separated beam of 15-MeV ^8B at 6 particles/second.

Contents

FOREWORD	i
INTRODUCTION	iii
0.1 Personnel updates	iv
0.2 Recent Accomplishments	iv
1 Neutrino Research	1
Overview of neutrino mass	1
1.1 Neutrino mass overview	1
KATRIN	3
1.2 KATRIN overview	3
1.3 FPD Simulation Overhaul	7
1.4 Future improvements of FPD simulations	9
TRIMS	11
1.5 TRIMS	11
Project 8	12
1.6 Project 8 overview	12
1.7 Completion of Phase II analysis	13
1.8 Project 8: Cavity CRES Apparatus (CCA) and electron gun	17
1.9 Atomic source development	19
1.10 Simulation of Cavity signals	20
LEGEND	23
1.11 Commissioning and status of the LEGEND search for $0\nu\beta\beta$ in Ge-76	23
1.12 Pygama: Analysis Framework for LEGEND	23
1.13 Characterizing Low-Energy Surface Backgrounds in LEGEND with the Krypton String Test Cryostat (KrSTC)	25
1.14 CAGE	27
1.15 LEGEND L-1000 lock system	31
1.16 SpIS and 42-Ar	32
1.17 Characterization of silicon photomultipliers at LN temperatures for LEGEND-1000	34
Selena	35
1.18 3D track reconstruction in Selena	35
1.19 Hybrid aSe/CMOS devices in flip-chip package	37
1.20 Topmetal-Se pixelated CMOS charge sensor	39
COHERENT	40
1.21 NaI(Tl) Crystal Scintillators for the COHERENT Tonne-Scale NaI(Tl) Detector Subsystem	40

2	Fundamental symmetries and non-accelerator-based weak interactions	44
	Torsion-balance experiments	44
2.1	In-Vacuum Rotation Sensors for the LIGO Seismic Isolation	44
2.2	Update on the Rotating Equivalence Principle Experiment	45
2.3	Advancements in Gravity Gradiometry	46
3	Accelerator-based physics	48
3.1	^6He Overview	48
3.2	First CRES Data with ^6He and ^{19}Ne	51
3.3	CRES Track Slopes and Radiated Power	56
3.4	He6-CRES Phase II RF system	57
3.5	^{19}Ne source	60
4	Precision Muon Physics	62
4.1	Overview	62
4.2	The Muon $g - 2$ Experiment	62
4.3	Measurements of the Incoming Phase Distribution in Run-6	66
4.4	Beam dynamics studies with the MiniSciFi detector	69
4.5	Anomalous spin precession frequency comparisons	73
4.6	Rare Pion Decays: PIONEER	76
4.7	Development of the PIONEER Simulation Framework	79
4.8	Characterization of LYSO:Ce as a PIONEER Calorimeter Option	81
4.9	Example of a PIONEER simulation study: decay-in-flight muon background .	83
	MuSun	86
4.10	Muon capture and the MuSun experiment	86
5	Dark matter searches	90
	ADMX	90
5.1	Searching for QCD axions between 800 MHz and 1.4 GHz	90
5.2	Preparing for a high frequency axion search with ADMX Orpheus	92
	DAMIC	92
5.3	DAMIC-M CCD Array	92
5.4	DAMIC at SNOLAB upgrade with skipper CCDs	95
5.5	Search for sub-GeV dark matter particles with DAMIC-M	97
5.6	Response of CCDs to surface events	98
5.7	Low-energy electronic recoils from Compton scattering in silicon	100
6	Education	101
6.1	Use of CENPA facilities in education and coursework at UW	101

6.2	Accelerator-based lab class in nuclear physics	102
7	Facilities	104
7.1	miniSciFi development for g-2	104
7.2	Instrument Shop	106
7.3	CENPA electronic shop	111
7.4	Operation of the cenpa-rocks computer cluster	113
7.5	Van de Graaff accelerator and ion-source operations and development	114
8	CENPA Personnel	115
8.1	Faculty	115
8.2	Postdoctoral Research Associates	115
8.3	Predoctoral Research Associates	116
8.4	Professional staff	117
8.5	Technical staff	117
8.6	Administrative staff	117
9	Publications	118

1 Neutrino Research

Overview of neutrino mass

1.1 Neutrino mass overview

R.G.H. Robertson

The discovery of neutrino flavor change by the SNO and SuperKamiokande collaborations shows that neutrinos have mass, in contradiction to a prediction of the minimal Standard Model, and explaining the anomalies in atmospheric and solar neutrino fluxes. It is now clear that neutrino mass eigenstates $m_{i=1,2,3}$ exist, of which at least two have non-zero mass. The flavor eigenstates are linear combinations of m_i , with amplitudes given by the elements of a 3×3 unitary mixing matrix U , the Pontecorvo–Maki–Nakagawa–Sakata (PMNS) matrix.

Oscillation experiments can determine only the differences of the squares $m_i^2 - m_j^2$, not the mass scale. It is known from solar neutrino oscillations that $m_2 > m_1$, but whether m_3 is the lightest mass eigenstate (“inverted ordering”) or the heaviest (“normal ordering”) is presently unknown. Oscillation experiments also constrain the sum of the three neutrino masses, Σm_i , to be at least 0.05 eV because masses are positive definite. The neutrino constitutes the first and, so far, the only identified dark matter in the cosmos. Limits on Σm_i have been obtained from observations of the cosmic microwave background and large-scale cosmic structure (for example, the Planck collaboration reported a limit of <0.12 eV within the framework of the Λ CDM model).

The most sensitive technique for a direct and model-independent neutrino mass determination is the analysis of the endpoint region of the tritium beta decay spectrum. The signal for neutrino mass emerges as a phase-space modification of the spectral shape close to the beta endpoint. This signal is independent of whether neutrinos are Majorana or Dirac particles. When the energy resolution in a beta spectroscopy experiment is larger than the neutrino mass splitting, it measures the electron-weighted neutrino mass,

$$m_\beta = \sqrt{\sum_{i=1}^3 |U_{ei}|^2 m_i^2}. \quad (1)$$

Neutrino oscillation experiments impose an ultimate lower bound of $m_\beta \geq 0.009$ eV ($m_\beta \geq 0.05$ eV) for the case of normal (inverted) mass ordering.

As we describe below, the KATRIN experiment has set a new upper limit of 0.8 eV at 90% confidence level¹. KATRIN’s design goal is a 0.2-eV mass sensitivity limit, if the mass is not larger. KATRIN is expected to either exhaust the quasidegenerate range of neutrino masses, or to measure the neutrino mass if it lies in that range.

The neutrino mass might turn out to be smaller than the state-of-the-art experiment KATRIN can discover. While there may be ways to extend the reach of KATRIN somewhat,

¹M. Aker et al., Nature Phys. 18, 160 (2021).

this type of experiment approaches a fundamental limit as a result of its sheer size and use of molecular tritium (T_2). With T_2 , one relies on a theoretical prediction of the spectrum of excited molecular states produced in beta decay, which broadens the spectral response. The neutrino mass effect is spread over a range of slightly differing endpoints for the excitations, exacting both a statistical and a systematic price. An independent direct measurement of this spectrum of excited states is not possible, although specific tests can be performed such as the TRIMS experiment we have carried out at CENPA, and they are in excellent agreement with theory at the percent level. To advance significantly beyond KATRIN’s design sensitivity—which is the goal of a next-generation tritium endpoint experiment—requires a different approach. An experiment that sets a neutrino mass limit of $m_\beta < 0.04$ eV would reach the full range of neutrino masses allowed under the assumption of an inverted ordering of neutrino mass eigenvalues and would either measure neutrino mass or exclude the inverted ordering.

The Project 8 Collaboration has devised a new method called Cyclotron Radiation Emission Spectroscopy (CRES) to reach this goal. In CRES, the emitted beta electron’s energy is measured by detecting its cyclotron radiation as it spirals in a magnetic field. In special relativity, the cyclotron frequency f_c in a magnetic field B is related to kinetic energy E_{kin} as follows:

$$f_c = \frac{1}{2\pi} \frac{eB}{m_e + E_{\text{kin}}/c^2}, \quad (2)$$

where e is the magnitude of the electron charge, m_e is the mass of the electron, and c is the speed of light in vacuum. Project 8 aims to combine CRES with the use of atomic tritium as the beta decay source, to remove uncertainty from molecular states. Our work toward this end is described below.

KATRIN

1.2 KATRIN overview

A. Beglarian[†], T. H. Burritt, P. J. Doe, S. Enomoto, J. A. Formaggio*, F. M. Fränkle[†], A. Kopmann[†], A. Marsteller, E. L. Martin[§], D. S. Parno[¶], D. A. Peterson, A. W. P. Poon[‡], R. G. H. Robertson, M. Sun, T. D. Van Wechel, J. F. Wilkerson[§], and S. Wüstling[†]

The discovery of neutrino oscillations implies that the neutrino has mass, contrary to the Standard Model of particle physics. With a planned sensitivity of 0.2 eV, KATRIN is currently the world-leading experiment making a direct, model independent probe of the absolute mass scale of the neutrino. At this level of sensitivity, KATRIN will be able to distinguish the neutrino hierarchy, inverted or normal. Other physics beyond the Standard Model (BSM) being addressed, include limits on sterile neutrinos (a dark matter candidate), relic neutrinos, and Lorentz Invariance violation. A comprehensive overview of the KATRIN experiment and the physics goals was presented in a Snowmass white paper and is given in¹.

KATRIN utilizes an experimental technique, pioneered over a period of 30 years by the Mainz and Troitsk experiments, in which an extremely precise measurement of the electron energy spectrum from tritium beta decay is made. As illustrated in Fig. 1.2-1, the presence of a massive neutrino results in a distortion of the spectrum, which is best observed close to the end point. Since the event rate in the region of the end point is low, such a measurement requires an intense tritium source, an excellent energy resolution, and low backgrounds.

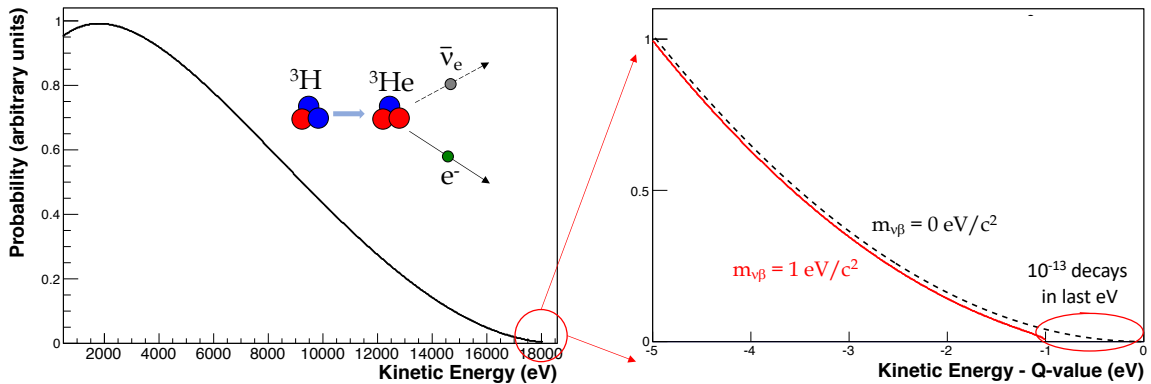


Figure 1.2-1. (Left) The tritium beta decay and resultant spectrum. (Right) The spectrum end point showing the effect of a 1 eV neutrino mass.

[†]Karlsruhe Institute of Technology, Karlsruhe, Germany.

*Massachusetts Institute of Technology, Cambridge, MA.

[§]University of North Carolina, Chapel Hill, NC.

[¶]Carnegie Mellon University, Chapel Pittsburgh, PA.

[‡]Lawrence Berkeley National Laboratory, Berkeley, CA.

¹M. Aker et al., J. Phys. G: Nucl. Part. Phys. **49**, 100501 (2022).

Proposed in 2001, “first light” operation of KATRIN began in 2016 and data taking with tritium commenced in 2018. The current neutrino mass program is expected to continue until 2025, after which the detector system will be upgraded to focus on the search for sterile neutrinos.

The layout of the KATRIN apparatus can be seen in Fig. 1.2-2. KATRIN is located at the Tritium Laboratory Karlsruhe, which has the license and expertise to handle the gaseous T_2 that is circulated at a rate of approximately 5 g per day through the 5 m long source tube in which the beta decays occur. Beta electrons escaping from the downstream end of the source are adiabatically transported towards the analyzing spectrometer by a chain of superconducting magnets.

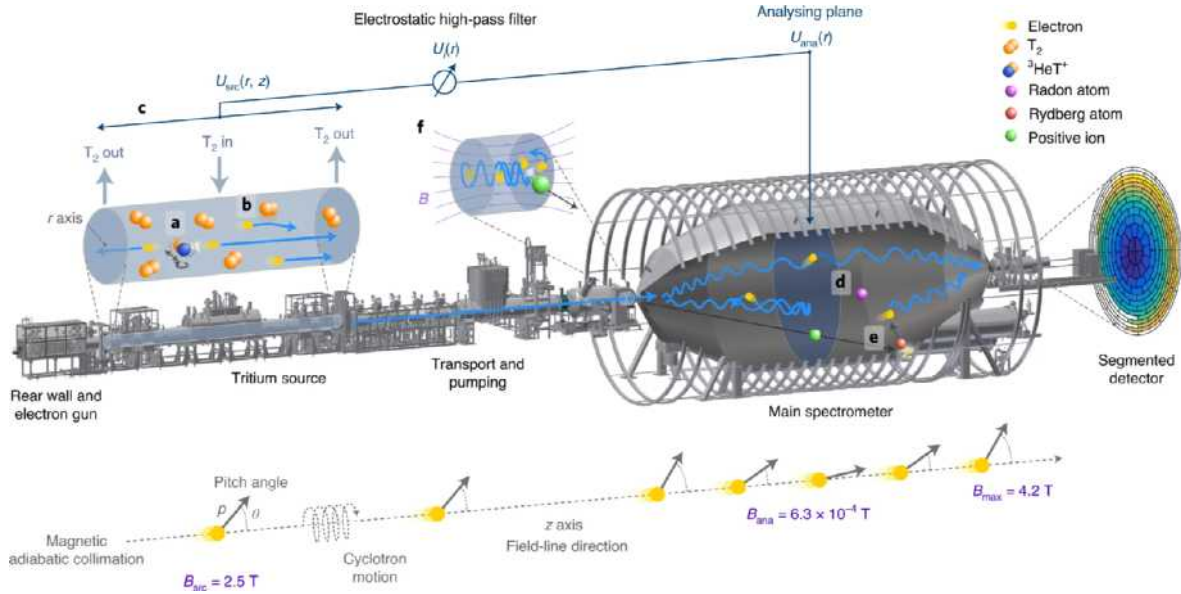


Figure 1.2-2. Principal features of the KATRIN apparatus.

T_2 molecules escaping from the source are removed by the differential pumping system (DPS) to be purified and returned to the source. Any tritium molecules escaping the DPS are trapped by the cryogenic pumping system (CPS) with beam-line walls coated by argon frost at 4.7 K, to which the T_2 molecules adhere. The combination of the DPS and the CPS reduces the T_2 entering and contaminating the spectrometers by 14 orders of magnitude. The two spectrometers are of the integral MAC-E filter type. Only electrons with energy above that of a retarding electrical potential pass through the spectrometer to be counted. The original purpose of the pre-spectrometer was to reduce the flux of electrons entering the main spectrometer, thus reducing backgrounds due to electron-gas interactions. Since the vacuum of the main spectrometer is around 1×10^{-11} mbar, that background is acceptable, and the pre-spectrometer is now operated close to ground potential to reduce backgrounds due to a Penning trap otherwise formed by the two spectrometers. The energy resolution of the spectrometer is approximately 2.8 eV, which is determined mainly by the ratio of the maximum magnetic field (4.2 T in the beamline) to the minimum field (0.63 mT at the

analyzing plane, the retarding potential plane of the spectrometer). To correct for external magnetic fields, the spectrometer vessel is surrounded by compensation coils.

Those electrons with sufficient energy to overcome the retarding potential exit the spectrometer and pass through a 10 kV post acceleration electrode, which raises them above local backgrounds before being counted by a monolithic p-i-n diode array consisting of 148 equal-area pixels. Gamma and electron sources calibrate and measure the efficiency of the detector array. CENPA was the US institute responsible for supplying this detector system and leads the study of its performance and associated systematic errors.

The primary means of calibrating the entire KATRIN system is by introducing gaseous $^{83\text{m}}\text{Kr}$ into the source, thereby providing monoenergetic electrons, and by using a variable energy electron gun situated in the rear section and capable of sending electrons down the entire length of the KATRIN beamline. The stability of the spectrometer retarding potential is monitored by a precision voltage divider. In parallel, a monitor spectrometer using $^{83\text{m}}\text{Kr}$ monitors the stability of the Kr line and hence the stability of the retarding potential.

Sources of background in KATRIN such as cosmic rays or environmental radiation were anticipated and designed against or identified and mitigated. KATRIN's sensitivity is currently limited by two backgrounds that are generated within the volume of the spectrometer vessel. These backgrounds result from magnetically trapped electrons scattering of the residual gas in the spectrometer, and from excited neutral atoms produced by radioactivity in the walls of the spectrometer that enter the spectrometer volume and are subsequently ionized by black body radiation or autoionization. These two sources of electrons dominate the background of 0.22 counts per second. Since the backgrounds are created throughout the volume of the detector, they were reduced to the present level by moving the analyzing plane downstream, albeit at a cost to energy resolution and event rate. The backgrounds remain an order of magnitude above expectation and ways of further reducing them are actively being developed, including a Transverse Energy Filter, described in ¹ with Hamish Robertson as a co-author.

Data taking is divided into “campaigns” which consists of tritium data taking, calibrations, systematic studies, and finally a maintenance period. A KATRIN Neutrino Mass (KNM) campaign lasts typically 3 to 4 months. KATRIN has just completed the 9th campaign. Combining data from KNM1 with KNM2 (see Fig. 1.2-3) provided the first sub-eV limit on the neutrino mass of <0.8 eV (90 % C.L.). The result of combining campaigns KNM1 to KNM5 is undergoing the final stages of analysis. All data used in these analyses are first preprocessed at CENPA to ensure data quality.

Two papers on BSM physics have been published: the “Search for Lorentz-Invariance violation” using KNM1 data², and “Search for keV-scale sterile neutrinos, using First Tritium data”³. The best direct limit on the local neutrino mass density in the galaxy has been

¹K. Gauda et al., Eur. Phys. J. C **82**, 10.1140/epjc/s10052-022-10858-0 (2022).

²M. Aker et al., Phys. Rev. D **107**, 082005 (2023).

³M. Aker et al., arxiv 10.48550/ARXIV.2207.06337 (2022).

published¹. A review of KATRIN has been published².

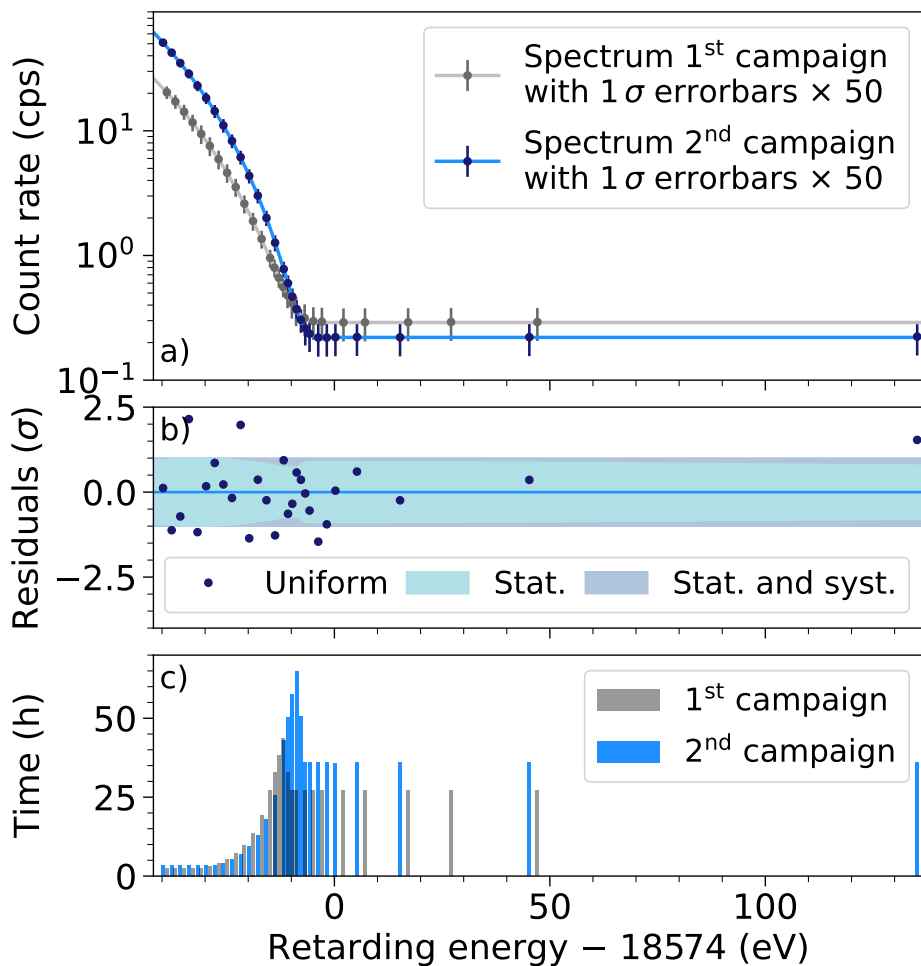


Figure 1.2-3. *Top:* The measured tritium beta spectra for KNM 1 (gray) and KNM2 (blue) along with (*middle*) the residuals of the KNM2 fits. *Bottom:* shows the time spent collecting data at the various retarding potentials. From ³.

The goal is to achieve 210 days of tritium data taking per year to achieve the original estimate of 1000 days required to meet the sensitivity goal of around 0.2 eV. The current neutrino mass campaigns are planned to continue until the end of 2025 after which KATRIN will undergo a major upgrade with the installation of the TRISTAN detector system, which is optimized for the search for sterile neutrinos and planned to extend through 2027.

¹M. Aker et al., Phys. Rev. Lett. **129**, 011806 (2022).

²A. Lokhov et al., Annu. Rev. Nucl. Part. Sci. **72**, 259–282 (2022).

1.3 FPD Simulation Overhaul

S. Enomoto and A. Marsteller

If the detection efficiency of the focal plane detector (FPD) changes during an integral spectrum scan, it deforms the measured spectrum shape and thus affects the neutrino mass estimation. The possible effects have been carefully investigated, including 1) the spectral coverage of the energy cut (region of interest, ROI) for varying spectrum shapes depending on the retarding potential of the spectrometer, 2) event counting inaccuracy due to the pileup of multiple electrons arriving within a short time interval, 3) loss or excess of counts due to the signal charge sharing among pixels, 4) changes of the detector properties due to temperature drift, etc., 5) systematics associated with back-scattering of the incident electrons, 6) influence of the cosmic muon veto, and 7) artifacts caused by the data acquisition electronics and software, including the dead-times.

The detector electronics simulation tool developed at CENPA, DRIPS, was used to describe and evaluate the effects of pileup at an accuracy better than 0.1%. All the other systematics were investigated in data-driven studies, to an accuracy at which the influence to the neutrino mass is negligible ($<10^{-4}$ eV²), except for one: the systematics induced by back-scattering cannot be fully characterized by measurements, and simulations of the FPD back-scattering process, combined with tracking of the back-scattered electrons in the KATRIN spectrometer, were not able to reproduce some of the measurements aimed to validate this part of the simulation, with a discrepancy of a factor of two.

Both a conservative upper limit set by the measurements and the simulation prediction were small enough to have only negligible effects on the current KATRIN uncertainties, but the discrepancy shows that there exist problems in our understanding of the apparatus, and it prevented us from using simulations to investigate any detector systematics. Thus, in 2022 at CENPA, we overhauled the entire simulation chain with careful step-by-step evaluations and redundancy at every step.

The simulation chain starts with interactions of the incident electrons with the FPD silicon detector. In addition to the KESS simulation package, which was developed in the KATRIN collaboration and has been used in KATRIN, we wrote a totally independent simulation with the Geant4 package, and the results on the back-scattered electrons, as well as the energy deposit in the detector were compared. A majority (>99%) of back-scattered electrons are immediately reflected back to the detector either magnetically by the pinch magnet field or electrically by the spectrometer retarding potential, to almost the same position on the detector due to the guidance of the magnetic field (displacement typically <10 μm) within a very short time interval, typically short enough (<1 μs) that the detector cannot resolve the signals as two separate hits. The remaining $\approx 0.1\%$ electrons that are not reflected will escape towards the source section and thus be lost from counting, constituting an important systematic of the detector because this will be a retarding-potential dependent detection efficiency change. This process is simulated using the KASSIOPEIA simulation package, which was developed in the KATRIN collaboration and has been extensively used, with and without detailed adiabatic tracking, and compared with an analytical model for redundancy. Finally, the hits of the primary incident electrons on the detector and all the subsequent

hits by the reflection of back-scattered electrons are fed into the DRIPS readout electronics simulation, which had been separately validated. The effects of the signal charge sharing over pixel boundaries were investigated using pixel-center spot beams from the e-gun and uniform illumination over the entire detector from the gaseous tritium and krypton sources.

During this process, we identified two serious software bugs in the previous simulation packages, and by fixing them, the factor of two discrepancies between the simulation and measurement has been resolved. Now with the simulation without known problems, a full chain of KESS/Geant4 - Kassiopeia/Analytical - Charge Sharing - DRIPS was constructed for the first time, and it indeed reproduced the measured energy spectra of tritium and e-gun well, as shown in Fig. 1.3-1.

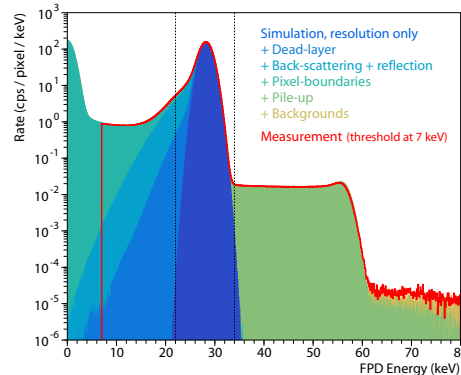


Figure 1.3-1. Measured FPD energy spectrum (red line histogram) for tritium beta decay electrons with an retarding potential of 18.3 keV and post-acceleration at 10 kV, and simulated spectra (filled histograms) for the measurement configuration. The two vertical dashed lines indicate the region of interest (ROI), fixed to 22 keV to 34 keV.

In addition, during this overhaul process, we noticed one physics process that had been overlooked; namely, if an electron is back-scattered, it happens more likely in a thin layer near the surface, where the dead layer lies, depositing a large fraction of energy due to the large angle change, possibly much larger than simple multiple passages in the dead layer. The multiple passages of the back-scattered electrons in the dead layer had been discussed previously and deemed to have negligible effects due to the small energy deposit in the dead layer, but the fact that the energy deposit could be larger if the electrons are back-scattered in there was not considered. This could be a systematic effect for KATRIN because the back-scattering probability changes depending on the incident electron angles, and the incident angles vary depending on the surplus energy of the electron in the spectrometer, leading to modification of the transmission function of the KATRIN spectrometer.

The new simulation chain was used to investigate the effect, and measurements were planned and performed according to the simulation prediction. The measurement results were in agreement with the simulation prediction, and the effect is now included in the systematics table. Fortunately, the effect was found to be negligible for the current KATRIN beta electron spectroscopy, but it could have significant impacts on other measurements, such as ones with krypton, and further investigations are going.

1.4 Future improvements of FPD simulations

S. Enomoto and [A. Marsteller](#)

Simulations of the KATRIN Focal-Plane Detector (FPD) have reached a stage at which they can estimate systematic effects on a level sufficient for KATRIN beta-scans. However, some discrepancies between simulation and measurement are still present, and can be of more importance for some of the KATRIN systematics measurements using mono-energetic and/or mono-angular electron sources. Therefore, based on the current simulation code, we are working on refining the involved physics processes to remove these discrepancies.

The first process that we have focused on is the electromagnetic reflection of electrons after they have backscattered from the FPD, in combination with the pixelation of our detector. In the simulations up to this point, the FPD wafer was a plane of infinite extent and electrons were immediately reflected at the location they left the silicon. This does not reflect the real measurement as electrons are guided along magnetic field lines on a cyclotron track during their movement in vacuum, displacing the point they are reflected to, in a first order approximation, by up to twice the cyclotron motion radius. We have experimentally clearly observed this during measurements with a low magnetic field at the FPD location. A lower magnetic field increases the cyclotron radius, causing electrons from a pencil-beam electron gun with an extent smaller than a single pixel which are backscattered to be detected on other pixels, all across the FPD. This is shown in Fig. 1.4-1. The majority of the events on the outer FPD pixels are coincident ($\Delta t < 1.6 \mu\text{s}$) with an event on the primary pixel hit by the electron gun.

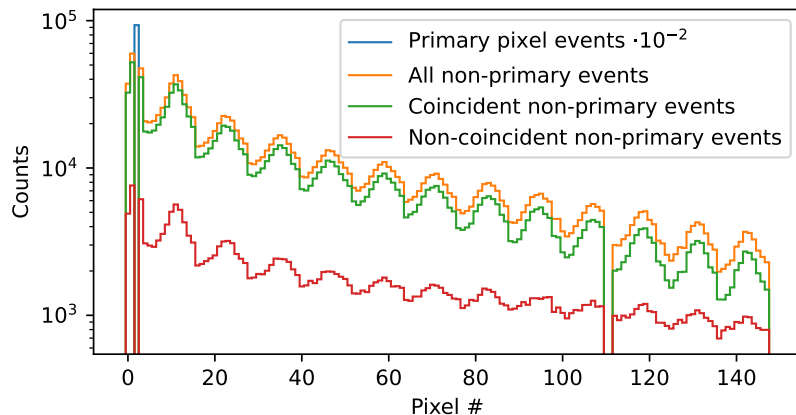


Figure 1.4-1. Measured KATRIN FPD data of the pencil-beam electron gun with the FPD in a reduced magnetic field of ≈ 0.006 T. Almost all events recorded on pixels other than the primary pixel hit by the electron gun are coincident with events on the primary pixel. Not all events are expected to be coincident as energy deposit in the primary pixel can be below the event trigger threshold.

As the electron gun emits electrons uniformly random in time with a rate of 5 keps in this measurement, random coincidences are expected to be $< 1\%$, which allows the conclusion that coincident events are caused by a single incident electron rather than a spreading of the pencil-

beam. To reflect these physics in our simulation, we have implemented an analytical model for the cyclotron motion in vacuum depending on the magnetic field strength at the FPD position, assuming adiabatic motion around a magnetic guiding center and an approximate randomization of the cyclotron phase. We have validated the use of an analytic model for the back reflection via dedicated Kassiopeia simulations of the electron motion with deviations on the %-level.

The next process we have refined is a second consequence of having a pixelated detector: Diffusion of charges created by the impinging electron across pixel boundaries on their way to the extraction electrode. If electrons hit the FPD close to a pixel boundary, the resulting cloud of charge carriers can be split between two or more adjacent pixels. The result of this can be either the detection of coincident events in multiple pixels if the split energy is above the detection threshold, or simply missing energy in the primarily hit pixel. We have approximated the diffusion of the charge cloud by a Gaussian with an effective charge cloud radius, the value of which can be extracted from data using a uniformly distributed electron source.

A final refinement step we are currently working on is the dead layer model used in our simulations. So far, a simple model using only a completely insensitive dead layer was in place. Measurements with a mono-angular electron source at different incident angles probe different effective dead layer thicknesses, and have shown that this simple model can not be used to explain the data. More complex models of the dead layer region with fractional charge collection (constant, linear, exponential, etc., see Fig. 1.4-2) are currently being implemented and will then be compared with high precision measurements.

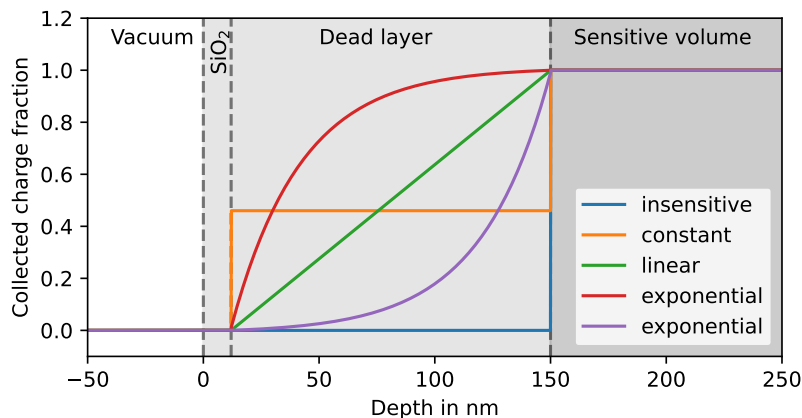


Figure 1.4-2. Illustration of models for fractional charge collection in the FPD dead layer.

By implementing these improvements to the physics in our simulation, we aim to accurately reproduce our experimental results while minimizing phenomenological descriptions. This will increase our confidence in the validity of our simulations and allow for a better estimation of the uncertainties on the KATRIN neutrino mass determination due to FPD related systematic effects.

TRIMS and the beta decay of molecular tritium

1.5 TRIMS

B. Daniel*, M. Kallander, Y.-T. Lin, D. S. Parno*, R. G. H. Robertson, and A. P. Vizcaya Hernández*

The most sensitive experiments to measure neutrino mass rely on the beta decay of tritium because it has a simple atomic structure. In practice, laboratory experiments such as KA-TRIN make use of molecular T_2 , and the initial state molecule may be thermally excited into accessible rotational states, while the final state has many possible electronic excitations, as well as vibrational and rotational excitations that are excited by the recoil momentum from the leptons. Each initial and final state corresponds to a slightly different endpoint energy, smearing the spectrum in the region where one looks for a distortion caused by neutrino mass. The excitation energies and probabilities are determined from theory. One test of this theory is the branching ratio to the bound molecular ion THe^+ . Two experiments carried out in the 1950s both gave branching ratios of $\sim 90\%$, whereas the present theoretical prediction is 57% , a striking and concerning disagreement¹.

The Tritium Recoil Ion Mass Spectrometer (TRIMS) was conceived and built at CENPA to make a comprehensive study with modern apparatus of the branching to ionic final states in the beta decay of HT and TT molecules. The apparatus construction and commissioning were completed at the end of 2017, followed by 18 months of data-taking.

A detailed analysis framework was built in parallel and the data analysis completed by the fall of 2019. The results, which form the thesis of Ying-Ting Lin, agree precisely with the theoretical prediction and disagree with the earlier measurements. These results have been published².

We consider that data-taking is complete, but the apparatus is in cold standby should further operation be called for. Diana Parno now holds a faculty position at Carnegie Mellon University, continuing her involvement in the experiment. Lin, Parno, Robertson, and two Carnegie Mellon students are working on a long paper on the TRIMS experiment. A semi-quantitative explanation for the failure of the historical experiments has been discovered and is set forth in the paper. Completion and publication of the paper was expected in 2022, but has taken longer than expected. The simulation of the dissociation in flight of quasi-bound states of HeT^+ is not complete.

*Carnegie Mellon University, Pittsburgh, PA.

¹L. I. Bodine, D. S. Parno, and R. G. H. Robertson, Phys. Rev. C **91**, 035505 (2015).

²Y. T. Lin *et al.*, Phys. Rev. Lett. **124**, 222502 (2021).

Project 8

1.6 Project 8 overview

E. Novitski and R.G.H. Robertson

Project 8 is a phased R&D program to measure neutrino mass by using Cyclotron Radiation Emission Spectroscopy (CRES) with atomic tritium. In Phase I the principle was demonstrated with $^{83\text{m}}\text{Kr}$, and in Phase II the first neutrino mass measurement was carried out, using in that case molecular T_2 . These experiments were done in small waveguide cells where the effective volume was a few mm^3 . To achieve in Phase IV the ultimate target neutrino mass sensitivity of 40 meV in Project 8, it is necessary to scale the CRES technique to volumes about a million times larger, and simultaneously to improve energy resolution by a factor of 10 and volume utilization efficiency by a factor of 60. These objectives are the goal of the Phase III stage.

In February 2022, the Project 8 Scientific Board recommended that the collaboration begin to focus on a resonant-cavity realization rather than an antenna array, and the decision to make the switch was finalized in the summer following further studies of the cavity concept. This was a difficult decision because of the substantial effort that had been devoted to the antenna array, but many of the analysis techniques (machine learning, matched filters) will carry over. The change was motivated initially by the need to move to lower fields to reduce the dipolar-interaction losses from the atomic trap, which are a strong function of magnetic field. That in turn re-opened the possibility of using a resonant cavity, not a practical method at high frequencies owing to the small characteristic size of cavities there. At low fields, free-space CRES radiation is weak and cavities offer orders of magnitude improvement in signal strength, along with reduced complexity.

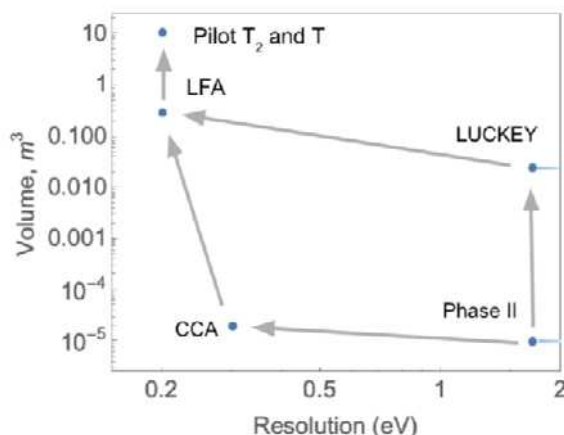


Figure 1.6-1. Project 8 CRES demonstrators plotted by resolution and cavity volume. Note that planned efficiency improvements are not represented on either axis.

A series of demonstrators of increasing size and capability will be built to address the goals outlined above. Figure 1 illustrates the steps along this path. The CCA (Cavity

CRES Apparatus) will make use of the existing 0.96-T MRI magnet at UW to test CRES in a resonant cavity. While small in scale, it is nevertheless intended to operate with a higher pitch-angle acceptance and higher resolution than Phase II and to show the viability of the cavity CRES approach. In parallel, a move to lower frequency (1.5 GHz) and larger size will be demonstrated in LUCKEY (Large UHR Cavity Krypton Experiment at Yale). The LUCKEY project calls for the design and construction of a 55-mT magnet. The Low-Frequency Apparatus (LFA) is a longer, higher-resolution version of LUCKEY to reach below 1 eV resolution with high acceptance and an effective volume of 0.05 m^3 . The first cavity CRES experiment with tritium is then at a lower frequency still and a volume $\sim 10 \text{ m}^3$. That experiment runs with molecular tritium. The final stage of Phase III is a comparable-size atomic T experiment supplied with low-temperature atomic tritium from an evaporative-cooling beam line developed at UW, Mainz, and UT Arlington. The last two experiments have world-class sensitivity in their own right.

1.7 Completion of Phase II analysis

C. Claessens, E. Novitski, and R.G.H. Robertson

The goal of the Phase II experiment was to demonstrate CRES spectroscopy of tritium beta decay. 2023 marks the completion of the Phase II tritium and krypton analysis and publication of the final results in PRL and PRC. After data taking had been completed in 2020, refining the analysis of the systematics was a continuous effort that resulted in a much improved understanding of the data and final uncertainties on the endpoint and neutrino mass results. Both are now statistics dominated.

Setup and data taking

The apparatus was similar to Phase I¹ in which a waveguide containing a gas cell was inserted into the bore of a superconducting ~ 1 T-solenoid. In Phase II the waveguide was circular with a radius of about 5 mm, allowing the transport of circularly polarized cyclotron radiation emitted by decay electrons from $^{83\text{m}}\text{Kr}$ or T_2 decays. The gas was contained by two calcium fluoride windows that are RF transparent and did not get degraded by tritium gas. The Phase II CRES cell is shown in Fig. 1.7-1. A gas system developed by UW enabled either T_2 gas, for the main measurement, or $^{83\text{m}}\text{Kr}$, a source of mono-energetic conversion electrons for calibration and systematic studies, to be fed to a cryogenic gas cell within the 1-T superconducting NMR magnet.

We took data in 2 magnetic trap configurations, a “shallow” trap of ≈ 0.04 mT and a “deep” trap of ≈ 1 mT. In the shallow trap, only electrons with pitch angles (i.e. angle between momentum vector and magnetic field vector) close to 90° are trapped. The deep trap retains electrons with pitch angles between $\approx 89^\circ$ and 90° . Since the reconstructed kinetic energy in Phase II is not corrected for the field variation experienced by the electrons in the

¹D. Asner et al., Phys. Rev. Lett. 114, 162501 (2014).

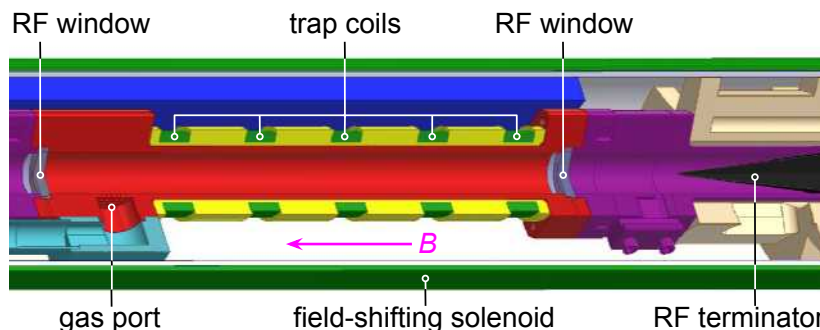


Figure 1.7-1. The Phase II CRES cell inside the waveguide is equipped with 5 copper coils to create trapping field geometries and closed off by two RF-transparent windows. The field-shifting solenoid was used to change the magnetic background field and measure the detection efficiency dependence on frequency.

trap, the shallow trap results in a better energy resolution, while the deep trap provides larger statistics at the cost of broadening of the recorded spectral lines. To increase the statistics in both traps, we used 2 coils to form a double shallow trap and 4 coils to form a quadruple deep trap. The currents in each coil were adjusted to bring the bottom of the traps to the same magnetic field level (Fig. 1.7-2) We performed many systematic studies in all trap configurations using the quasi-mono-energetic internal conversion decay lines of $^{83\text{m}}\text{Kr}$. In December 2019 we then switched to recording tritium data for 82 days using the quadruple deep trap.

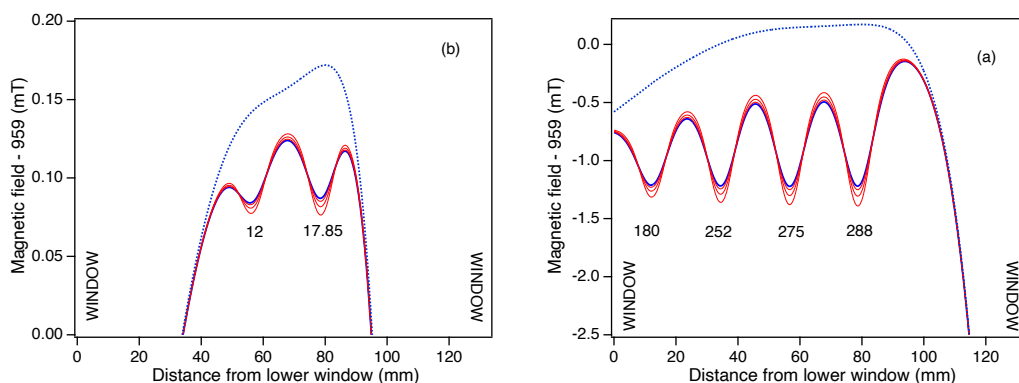


Figure 1.7-2. Magnetic field profiles of the double shallow (left) and quadruple deep (right) electron traps.

Analysis

Many of the experimental choices made in Phase II with the goal of increasing the number of detected tritium events turned out to make the analysis of the tritium data rather complicated. Due to reflections in the waveguide, the Signal-to-Noise Ratio (SNR) of events was very different in each of the four traps comprising the quadruple deep trap. Not only was the absolute value of the SNR different, but also its variation with frequency depended on the trap z -position in the waveguide. Overall, the detection efficiency was poor for pitch angles

of 89° or lower. Since many electrons had pitch angles smaller than that, they could scatter into a detectable pitch angle after having lost energy during scattering. This caused a wide tail in the traps' response function¹.

Many systematic studies and model refinements were needed in order to analyze the tritium data. The inputs to the analysis came from the systematic studies with krypton but had to be adjusted to the differences during tritium data taking (pressure, gas composition, electron energy, ...). Fig. 1.7-3 shows the detector response model fitted to the 17.8-keV krypton line in the double shallow and quadruple deep traps. Fig. 1.7-4 shows the detection efficiency as a function of frequency and energy. The tritium spectrum model has to be convolved with the detector response and multiplied with the detection efficiency before it can be fitted to the data. Fig. 1.7-5 shows the 3770 recorded tritium events fitted with the model and the resulting neutrino mass and endpoint contour. Two analyses of the tritium data were performed. A Bayesian analysis by T. Weiss (Yale University) found an endpoint result of 18553_{-19}^{+18} eV and an upper limit on the neutrino mass of $155 \text{ eV}/c^2$ (90% C.L.). A frequentist maximum-likelihood analysis performed in the local group at CENPA found an endpoint result of 18548_{-19}^{+19} eV and set an upper limit on the neutrino mass using the Feldman-Cousins method of $152 \text{ eV}/c^2$ (90% C.L.). The results are in excellent agreement with each other and with the sensitivity prediction for Phase II by H. Robertson of a standard deviation $\sigma_{m_\beta^2} \approx 10000 (\text{eV}/c^2)^2$

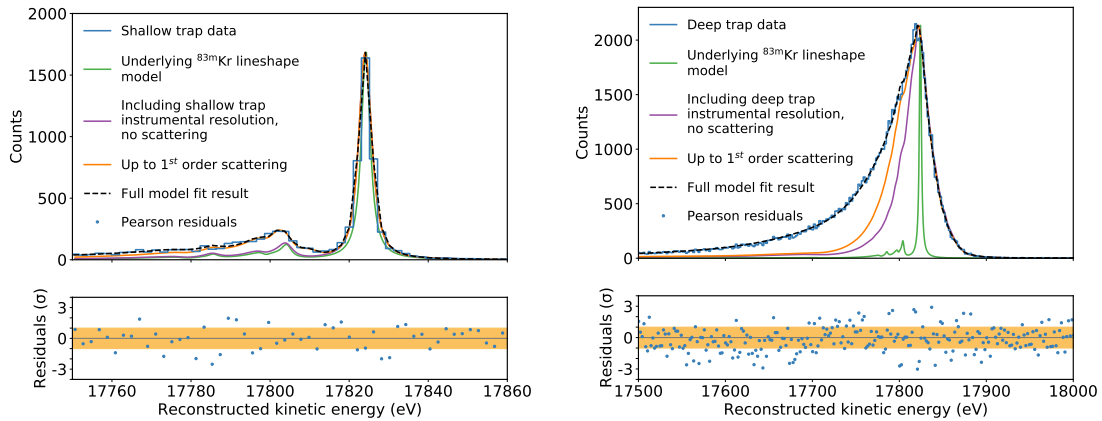


Figure 1.7-3. ^{83m}Kr K-line spectrum convolved with the detector response function in the double shallow (left) and quadruple deep trap (right) in comparison with data (blue, both sides). The shallow-trap data fit demonstrates an energy resolution of 1.7 eV at FWHM. Analysis by Yu-Hao Sun (Case Western Reserve University).

¹Spectral shape of a truly monoenergetic line after detection and reconstruction of the signals.

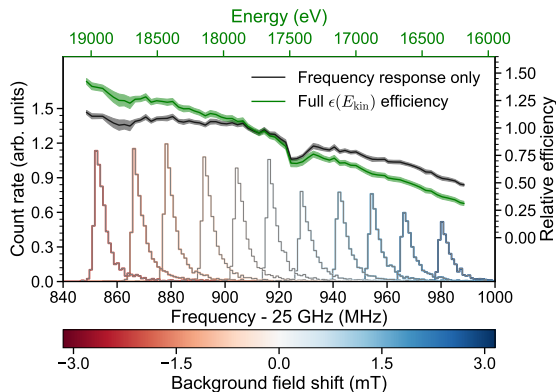


Figure 1.7-4. The detection efficiency dependence on frequency is extracted from the changing event rate in the K-line when shifting it across the frequency region of interest. A correction for the absence of the energy covariance with frequency is made before the relative efficiency curve (green) is used in the tritium data analysis. Analysis by C. Claessens.

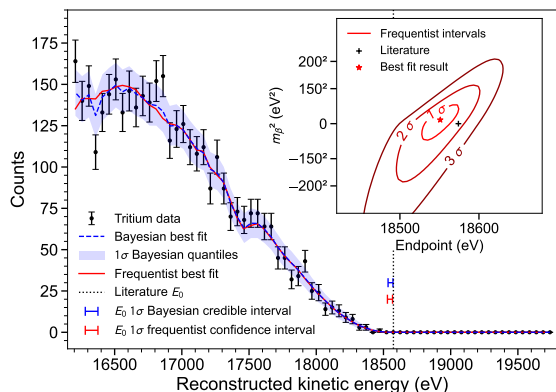


Figure 1.7-5. Tritium spectrum recorded in Phase II overlaid with fitted Bayesian and frequentist models. Inset: Frequentist neutrino mass and endpoint contour plot. The literature sources are given in the paper¹ and for the mass limit².

Publication

After a detailed internal review of the analysis and the paper drafts, the Phase II results were submitted in March to PRL [50] together with a full description of the analysis to PRC [51]. After one round of review comments, the PRL paper was accepted for publication. Acceptance of the PRC was also recommended by the reviewers but is awaiting several structural revisions. The publication of the Phase II results is a milestone for Project 8 and CRES that showcases that a neutrino mass limit can be obtained with CRES and that the systematics can be well controlled. In Phase III, the collaboration is charged to pick up where Phase II left and demonstrate the scalability of the technique and the compatibility with atomic tritium.

¹A. Ashtari Esfahani et al., Phys. Rev. Lett. 131, 102502 (2023).

²D. Asner et al., Phys. Rev. Lett. 114, 162501 (2014).

1.8 Project 8: Cavity CRES Apparatus (CCA) and electron gun

C. Claessens, S. Enomoto, M. Huehn, M. Kallander, A. Marsteller, E. Novitski, and R.G.H. Robertson

The first major milestone of Project 8's Phase III will be a demonstration of CRES in a resonant cavity environment. This Cavity CRES Apparatus (CCA) (Fig. 1.8-1) at UW will be used to verify predictions based on custom simulation packages of the achievable effective volume and the basic phenomenology required for an endpoint measurement: energy resolution, position sensitivity, rate capability, low-background operation, as well as testing calibration techniques. The CCA is being designed and constructed, with commissioning to start in Fall 2023. It is expected to start scientific operations no later than early 2024 and to complete with results by the end of 2025.

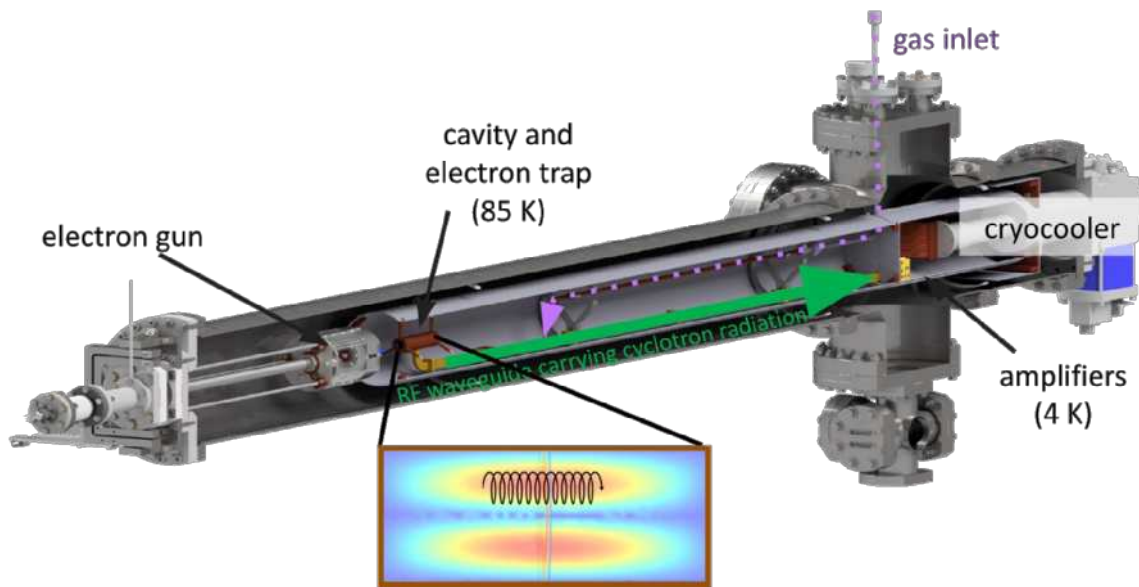


Figure 1.8-1. Layout of the Cavity CRES Apparatus (CCA).

Although the demands of the atomic source will drive Project 8 to frequencies of 1 GHz or less, it is most expedient to do this first cavity CRES demonstration at about 26 GHz. Project 8 already has a repurposed MRI magnet charged to the corresponding field 0.96 T, and the analog receiver and digital DAQ from Phase II are transferable with minor modifications. Monoenergetic conversion electrons from $^{83\text{m}}\text{Kr}$ and from the Mott-scattering of an electron beam will be used to demonstrate energy resolution, rate capability, and position reconstruction.

The CCA will require the design and production of cavities, with prototypes tested on the lab bench before any CRES measurements. Key performance parameters are the frequencies

and Q -values of the TE_{01p} modes and the suppression of all others. The CCA will need an electron trap, which can be reliably designed with existing tools.

The CCA will be a novel instrument with new capabilities. Three scientific measurements of ^{83m}Kr are planned: observation of the weak 42 keV crossover transition from the 1.8-hr isomer to the ground state, the absolute energy of the 32 keV transition, and the shape of the shakeup and shakeoff satellite spectra¹. The absolute energy is of interest to KATRIN as it will allow comparison of their measured endpoint energy with the $T-^3\text{He}$ mass difference, an important systematic test².

CENPA has designed and built an electron gun to serve as a calibration source for the Phase III demonstrators and as a prototype for Phase IV. (Fig. 1.8-2) Spatial variations in electric potential and magnetic field within order m^3 trap volumes must be understood, as must variations in detection efficiency with energy. The electron gun is a near-ideal calibration source for this purpose: it will introduce monoenergetic electrons at a known energy into the trap volume, which can then be detected using CRES. It will produce a $1\ \mu\text{A}$ current of electrons at an energy tunable between 18 and 30 keV, with a narrow 0.3-eV beam energy spread expected from the BaO or LaB₆ cathode. A small fraction of these electrons will Mott-scatter from low-density He or Ne gas into trappable pitch angles within the trap volume and will be detected.

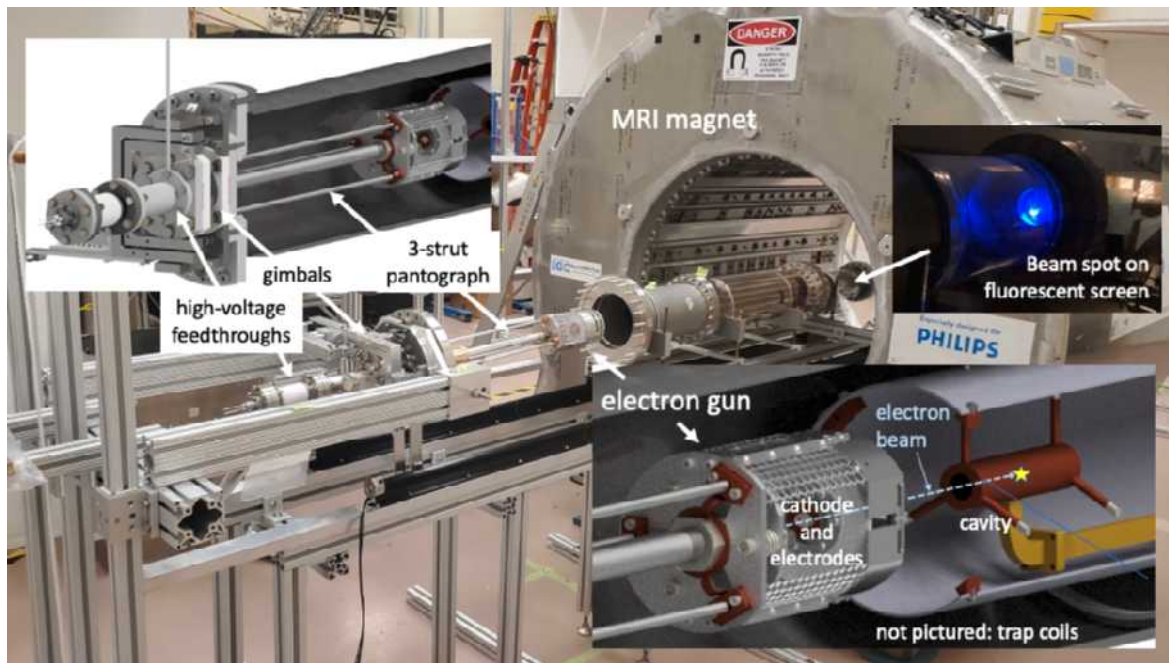


Figure 1.8-2. Electron gun during assembly.

¹R. G. H. Robertson and V. Venkatapathy, Phys. Rev. C 102, 035502 (2020).

²C. Rodenbeck, Eur. Phys. J. C 82, 700 (2022).

1.9 Atomic source development

C. Claessens, P.J. Doe, S. Enomoto, M. Kallander, A. Marsteller, and R.G.H. Robertson

Atomic tritium will play an essential role in pushing the sensitivity of Project 8 below the inverted neutrino mass hierarchy by avoiding a broadening from molecular final states of the beta-decay. Furthermore, the difference in endpoint between atomic and molecular tritium of several eV, which would result in a sensitivity degrading molecular background spectrum, requires a low fraction of molecular tritium. While the creation of atomic hydrogen is an established procedure and some of the knowledge can be transferred to tritium, the Project 8 requirements of a very high flux of $\approx 10^{19}$ Atoms/s and a low fraction of molecular tritium pose a challenge. For our development of such a source, we will at first only use the inactive hydrogen isotopes.

As Project 8 requires neutral atoms, the flux rate makes dissociation of molecules via ionization followed by neutralization an unlikely path to success. We have therefore decided to make use of thermal dissociation by flowing gas through a tungsten capillary heated to >2000 K, which is a technique used in commercially available sources for atomic hydrogen. We have acquired such a commercial source and installed it in a test setup where the beam of atomic hydrogen is guided through skimmers into a mass spectrometer¹. Since then, we have improved the setup by adding a dedicated beam stop chamber, which drastically improves the background of hydrogen hitting the backstop inside the mass spectrometer chamber an increasing the background pressure. This has allowed us to take data showing dissociation of molecular deuterium at a flow rate of 1 sccm. The results of this measurement are shown in Fig. 1.9-1.

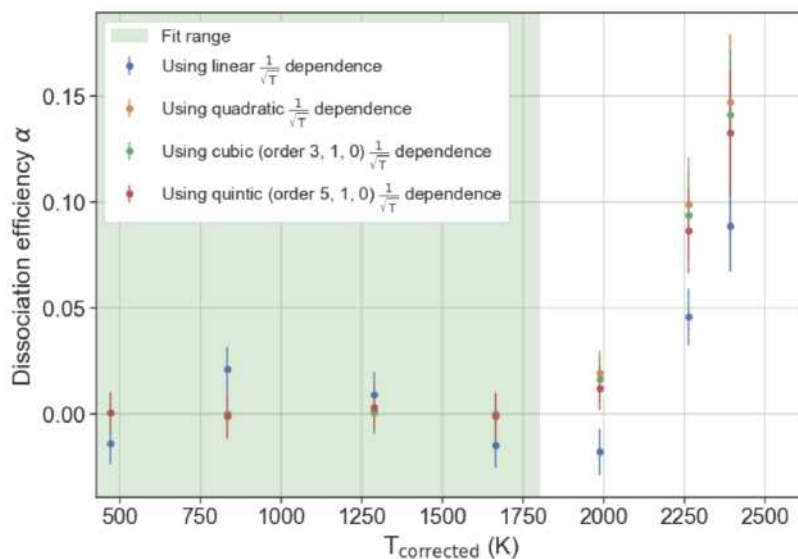


Figure 1.9-1. Dissociation measurement of deuterium. Shown is the dissociation efficiency α in dependence of the capillary temperature. Dissociation starts to set in at around ≈ 2000 K.

¹CENPA Annual Report, University of Washington (2021) p. 27.

In parallel to the commercial atomic hydrogen source, we have developed a hydrogen cracker based on a coaxial tungsten capillary heated directly by current flow through the capillary. We have performed initial tests using this cracker to determine its thermal characteristics and investigate the temperature profile inside the capillary using a thermocouple, which is shown in Fig. 1.9-2. As using a thermocouple in this way is not possible during hydrogen dissociation operation, we have started to develop a camera based pyrometry approach Fig. 1.9-2.

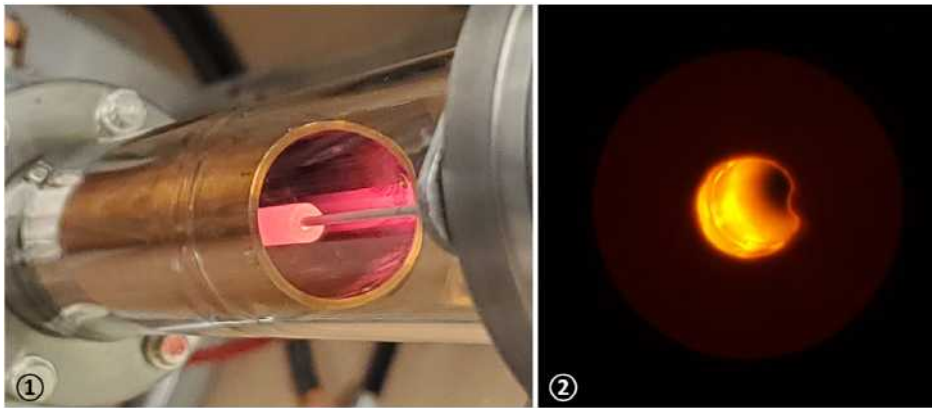


Figure 1.9-2. Shown in (1) is the red hot glowing coaxial cracker, surrounded by a copper heat shield. The tiny cylinder inserted into the front of the coaxial cracker is a Type C thermocouple movable along the length of the capillary. Surrounding both is a vacuum system to prevent oxidation of the tungsten at high temperatures. Shown in (2) is an image taken with the pyrometry setup, looking into the center of the capillary from the front. The larger, dark red ring is the front face of the coaxial cracker with the dimple reaching towards the center of the capillary being an imperfection of the manufacturing process. Inside of the capillary, the higher brightness and brighter color indicate a higher temperature.

The next steps will be commissioning of the coaxial cracker in the test stand used with the commercial atomic hydrogen source, followed by installation of a beam chopper for time of flight measurements. Time of flight measurements will allow us to determine the not necessarily Maxwellian velocity distribution of atomic hydrogen produced by the cracker. This will be followed by the installation of an accomodator, cooled to approximately 40 K. The efficiency in cooling down the atoms to temperatures at which magnetic guiding and cooling of the atoms can be achieved, will be determined using time of flight.

1.10 Simulation of Cavity signals

A. Marsteller and R.G.H. Robertson

The Phase I and II data of Project 8 were analyzed via short-time Fourier transforms that pixelized the RF power in frequency and time. For Phase III we plan to use a resonant cavity to detect CRES and to work with the time-series data rather than frequency-space data. Extracting parameters such as the cyclotron frequency from the time series preserves the phase information throughout the track, information that has not been used before.

A necessary step for testing such an approach is the generation of simulation data with known true parameters in order to determine the reconstruction efficiency and uncertainties on the parameters. For this purpose, we have developed a new approach to the simulation of a CRES electron signal in a resonant cavity.

The equivalent circuit for a resonant cavity is an LCR circuit, a lossy tuned circuit. This is valid (only) when other cavity resonances are far away from the one in use. A tuned circuit has the response of the amplitude A of a 1D underdamped driven harmonic oscillator for a driving force f :

$$\left(\frac{\partial^2}{\partial t^2} + 2b \frac{\partial}{\partial t} + \omega_C^2 \right) A(t) = f(t, z, v_z), \quad (1)$$

which depends on time, location, and velocity of the electron. The driving force f encompasses knowledge of the motion of the electron, as well as information about the coupling of the electron to the cavity.

As an analytical description for f is only possible for the simplest configurations. We need to approximate f by a computable alternative f^* , which is given by a train of δ -like impulses:

$$f^*(t, z(t), v_z(t)) = \sum_n f(nT, z(nT), v_z(nT)) \delta(t - nT), \quad (2)$$

The electron motion is obtained via a Kassiopeia simulation of the electron inside the magnetic trap containing the cavity. Single steps of this simulation are taken as the δ -like impulses for f^* .

For a δ function as driving force in the above equation, the solution is the Green's function. Therefor, the solution to the differential equation is the superposition of the Green's function G of the driven harmonic oscillator for each step of f^* , scaled with the driving force $f(nT, z, v_z)$ at each step. A model for the term $f(nT, z(nT), v_z(nT))$ is given by a term $C(r(nT), z(nT))$ which describes the coupling to the cavity, as well as a term $a(nT, z(nT), v_z(nT))$ that contains the overall amplitude of the signal as well as the sinusoidal nature of the cyclotron motion. In a simplified approach, $C(r, z)$ is given by the TE011 mode, which leads to:

$$C(r, z) = \cos\left(\frac{\pi}{L}z\right) J_1\left(X'_{01} \frac{r}{r_C}\right), \quad (3)$$

$$f(nT, z, v_z) = A_0 \sin\left(\omega_c(nT + \left|\frac{z}{v_p}\right|) + \varphi\right) \cos\left(\frac{\pi}{L}z\right) J_1\left(X'_{01} \frac{r}{r_C}\right), \quad (4)$$

where X'_{01} is the first zero of the derivative of the order-zero Bessel function.

This model has since been incorporated into the Locust simulation software package developed by the Project8 collaboration, including further refinements such as the back-reaction of the electric field inside the cavity on the electron.

Using this model, time series data has been generated and parameters such as the central frequency as well as axial frequency could be extracted using a fit (see Fig. 1.10-1).

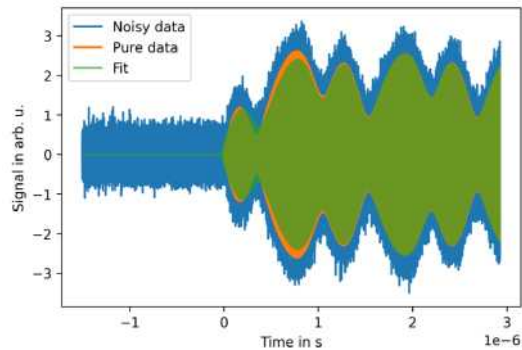


Figure 1.10-1. Simulated data of a CRES electron inside of an idealized cavity modelled as a 1D harmonic oscillator. A fit to the simulated data overlaid with Gaussian white noise was used to extract parameters such as the cyclotron frequency.

Further work using this simulation approach within the Project 8 collaboration has shown the viability of the parameter extraction from the time-series approach for event reconstruction. For one of the crucial points during CRES event reconstruction, a degeneracy between energy and pitch angle of the electron with respect to the magnetic field, this approach appears very promising in disentangling both parameters. A significant issue that remains to be solved is the need for good initial parameter estimates in order for methods such as likelihood minimization to efficiently find the very sharp global minima in a parameter landscape of periodic local minima.

LEGEND

1.11 Commissioning and status of the LEGEND search for $0\nu\beta\beta$ in Ge-76

S. Borden, T. Burritt, J. A. Detwiler, A. Hostiuc, C. J. Nave, D. A. Peterson, R. Roehnelt, N. W. Ruof, G. Song, T. D. Van Wechel, and C. Wiseman

LEGEND is a next-generation neutrinoless double-beta ($0\nu\beta\beta$) decay search in ^{76}Ge . By combining the technological expertise and experience from the MAJORANA DEMONSTRATOR and GERDA experiments, LEGEND is expected to reach a design sensitivity two orders of magnitude greater than its predecessors.

The phased program advances from the intermediate scale LEGEND-200 experiment to the future LEGEND-1000 experiment. LEGEND-200 is currently taking physics data with ~ 140 kg of enriched HPGe detectors deployed at the Laboratori Nazionali del Gran Sasso (LNGS) in Italy. Background analysis is beginning and first background results are expected in summer 2023, with first physics results coming hopefully in 2024.

LEGEND-1000 is a leading candidate for a future US-led tonne-scale $0\nu\beta\beta$ experiment. It leverages the advances of the ^{76}Ge program, through LEGEND-200, to retire risks in demonstrating array scalability and achievement of background goals. It will yield an additional order-of-magnitude sensitivity to the $0\nu\beta\beta$ half-life, covering the neutrino mass parameter space allowed by the inverted ordering of neutrino masses.

Members of the LEGEND group at CENPA were present for installation and commissioning work on LEGEND-200 at LNGS in October and November 2022 and assisted in transitioning to stable physics data-taking in the winter of 2023.

The CENPA LEGEND group also plays a leading role in the development of the analysis framework for the project, which is actively tested on the data collected with our local test stands. Professor Detwiler is a member of the LEGEND Steering Committee, an Analysis Co-Coordinator, and the lead of the Analysis Framework task group. Locally, we are pursuing R&D efforts to understand the surface response of HPGe detectors and the light detection of SiPM detectors. These efforts are described in the subsequent sections.

1.12 Pygama: Analysis Framework for LEGEND

S. Borden, J.A. Detwiler, C. Nave, G. Song, and C. Wiseman

The UW LEGEND group helped lead the implementation of a set of data processing and analysis tools for LEGEND-200, known as *pygama*. This framework contains the primary routines for converting data into analyzable format, running computationally-intensive digital signal processing routines on the detector traces, and calibrating and tuning the reconstructed experimental observables, including energy / number of photons and pulse-shape discrimination parameters. An overview of the data processing pipeline is shown in Fig. 1.12-1. These tools

are now running on data as it comes out of the LEGEND-200 apparatus in an automated workflow.

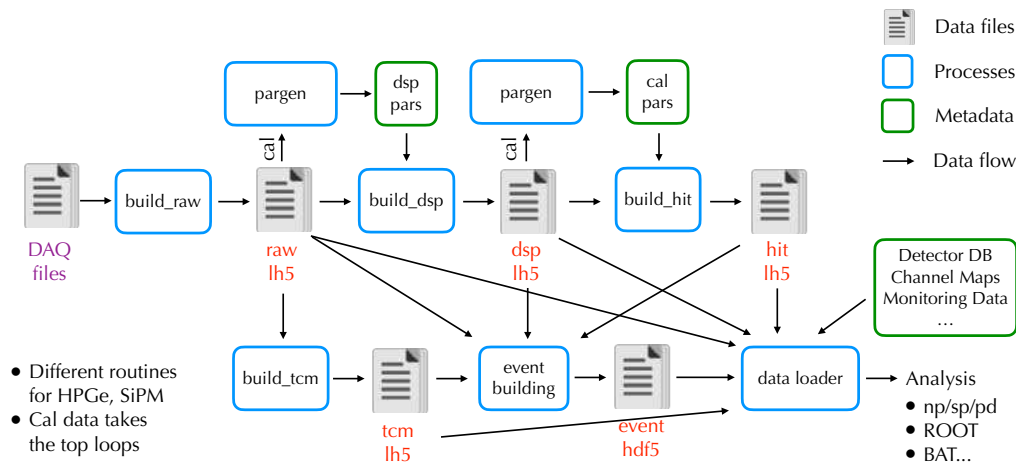


Figure 1.12-1. Illustration of the data processing pipeline for LEGEND data, extending to HPGe detectors, SiPMs, and PMTs. Data from each detector are analyzed automatically to produce pole-zero constants and other parameters necessary to optimize the energy resolution of the detectors. Data from each detector are processed separately until later stages, where timing information is incorporated to produce “events” from the full array for coincidence analysis.

Several important milestones in the development of `pygama` were completed this year. A major refactoring / repackaging of the code improved organization, reusability, and flexibility. This came with the implementation of a robust set of unit tests that greatly improved robustness and validation of new contributions. A full suite of analysis routines for germanium and silicon photomultiplier detector signals were implemented in the framework for LEGEND-200 data processing (an example of their application for calibration data is shown in Fig. 1.12-2). Key components for the generation and manipulation of time coincidence maps were implemented. A number of new digital signal processors were added, and support for new input formats was greatly improved.

A critical contribution worth special mention was the implementation of the “data loader” that provides high-level access to the full data set. Using a “file database” object that stores metadata about what parameters are available in which files on disk, the data loader allows users to specify run lists, subsets of detectors, and collections of parameters to be automatically retrieved from disk. The interface supports selections and cuts, coincidence event building, and multiple output formats. This tool has enabled a vastly expanded analysis effort across the collaboration.

Another key contribution worth special mention was the implementation of a “post-processing” stage for the conversion of DAQ output files into the “raw” HDF5 format used in

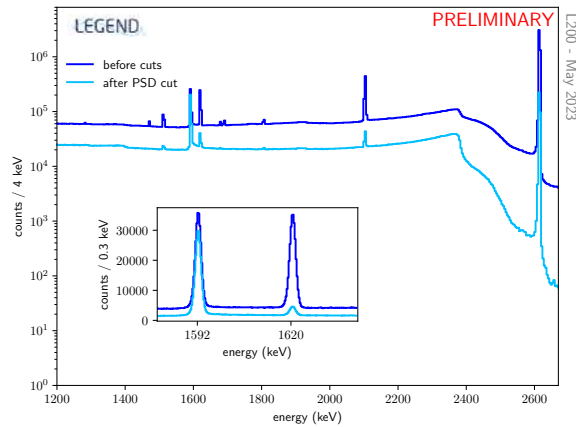


Figure 1.12-2. LEGEND-200 calibration data as processed by `pygama`.

the analysis. This stage includes tools for modifying, transforming, renaming, compressing, dropping, or adding new fields to the raw data during the decoding / HDF5 conversion stage. This stage is being used to implement waveform windowing, presuming, and compression routines that will save a factor of 4 in LEGEND-200 file sizes, while also affording a significant speedup in digital signal processing routines at the same time.

The `pygama` suite is essentially fully functional at this point, although continued development is envisioned. Refactoring of many of the mathematical routines and parameter calibration and optimization code, that should greatly improve performance and flexibility. We continue to iterate on packaging and modularity, and implement community standards for public software. We are also implementing additional tools for building and manipulation event-level information, which is a current focus of LEGEND-200 analysis.

1.13 Characterizing Low-Energy Surface Backgrounds in LEGEND with the Krypton String Test Cryostat (KrSTC)

J. A. Detwiler, N. Fuad, N. Miedema, C. J. Nave, D. A. Peterson, W. Pettus, T. D. Van Wechel, and C. Wiseman

Understanding the energy spectrum produced by high-purity germanium detectors (HPGe) used in the LEGEND experiment is a critical check against our understanding of the components making up the background for the experiment. This is of particular importance near the $Q_{\beta\beta}$ value of 2039 keV in ^{76}Ge , the energy at which we expect neutrinoless double beta decay ($0\nu\beta\beta$) to occur. Due to the extremely slow (if existent) decay rate of $0\nu\beta\beta$, the region near $Q_{\beta\beta}$ must be practically background free to claim a discovery. There are a number of backgrounds that can contribute to the measured LEGEND energy spectrum. One background of interest for the UW LEGEND group is from surface events. Ionizing radiation can interact with the passivated surface of an HPGe and lose some of its energy in that passivation region. CAGE studies this effect with surface alphas which is relevant for $0\nu\beta\beta$ analysis, and the Krypton String Test Cryostat (KrSTC) uses low-energy electrons, gammas,

and x-rays to study this phenomenon at low-energy. These energies are well below $Q_{\beta\beta}$ but this energy region is worth studying due to LEGEND's sensitivity to potential beyond the Standard Model (BSM) physics.

A picture of the KrSTC experimental setup is shown in Fig 1. It consists of a cryostat with a p+ point-contact (PPC) ^{76}Ge detector deployed inside of it. This cryostat is pumped to near vacuum pressures with a turbo pump and cooled with liquid nitrogen. When the detector is in vacuum and cold, it can be biased to $\sim 2700\text{ V}$ where it is then ready to collect data. The charge created by ionization inside the detector is drifted (due to the bias voltage) towards our front-end electronics, amplified by our post-amp electronics (all made by our electrical engineers at CENPA) and read-out as a signal. We study this low-energy degradation effect through the use of a ^{83m}Kr source which has monoenergetic electron, gamma, and x-ray lines. We introduce this gaseous krypton into our system and observe a different energy spectrum from background runs. Any deviations from the expected energy spectrum can give us some handle on this degradation effect.

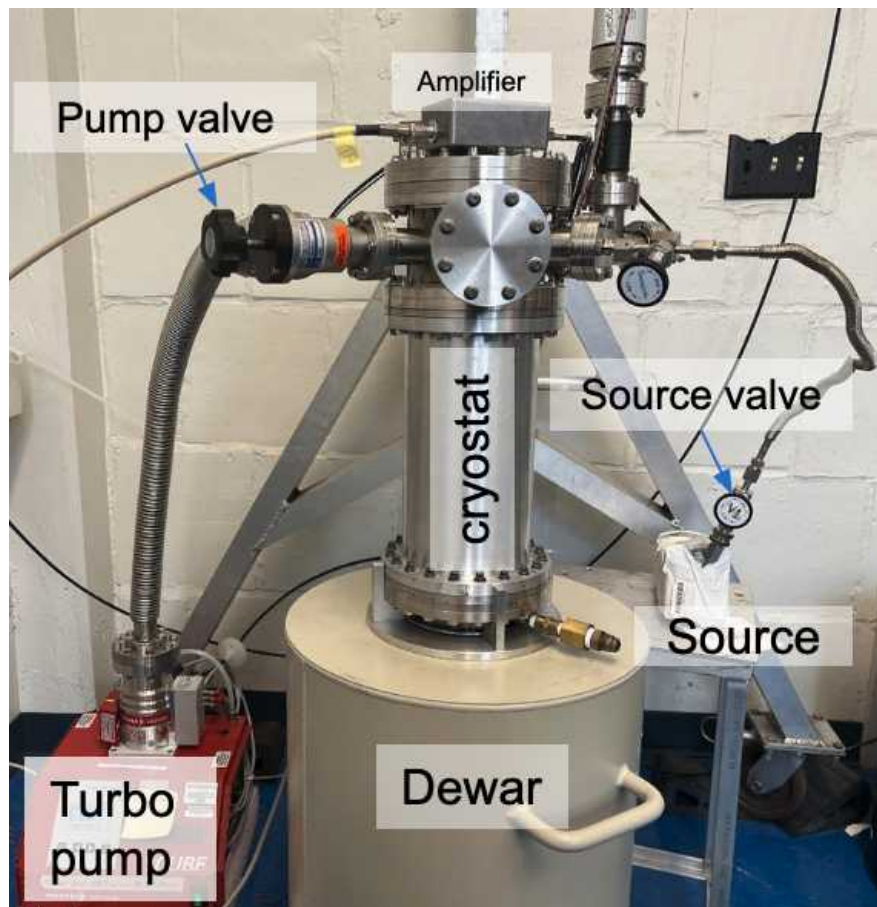


Figure 1.13-1. Image of the experimental setup for the KrSTC experiment. A PPC ^{76}Ge detector is deployed in the cryostat for data-taking.

In February 2023, we found our first strong evidence of a krypton signal, see Fig 2. Notable spectral features are a potential x-ray peak at $\sim 12.6\text{ keV}$ and a gamma peak at \sim

9.4 keV. The deviation between background and krypton data begins at the endpoint of the ^{83m}Kr spectrum, ~ 32 keV. There is also promising analysis that shows we may be sensitive to these Kr events by looking at pulses with quick initial rise times, as these events are occurring very near to the passivated surface of the detector. More analysis is needed and looking at other waveform parameters, such as the time it takes for final charge collection, is warranted. Machine learning projects looking for waveform anomalies is also in the works and should be an exciting thesis project!

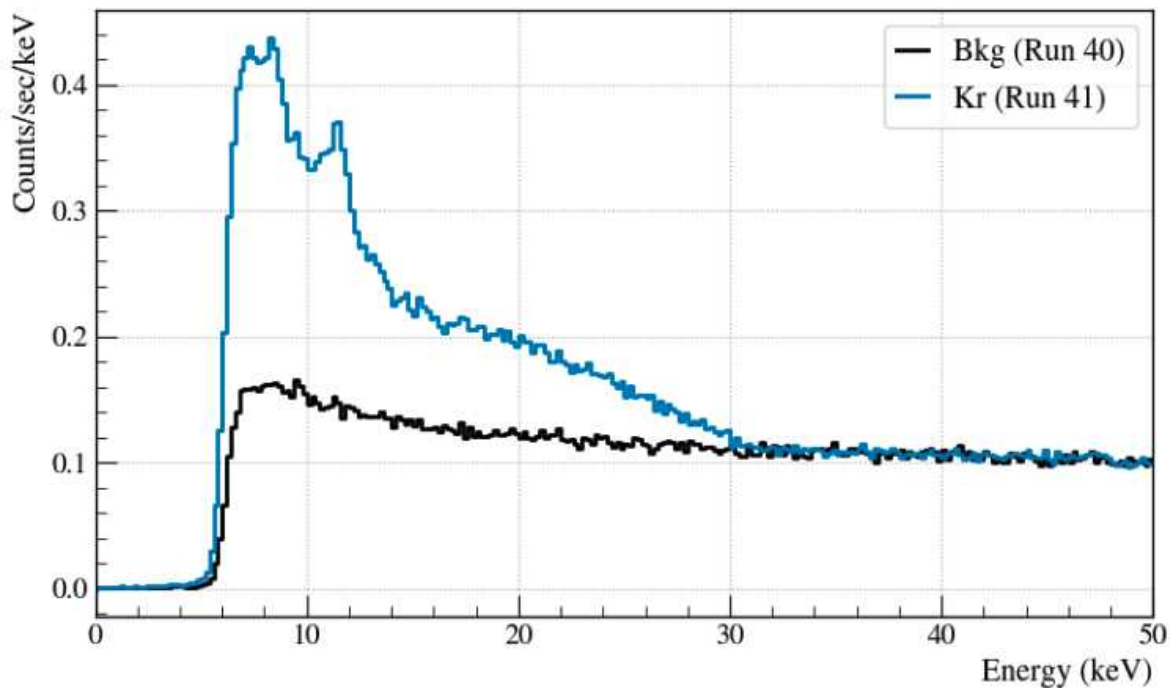


Figure 1.13-2. Calibrated energy spectrum of a background and krypton run. Potential spectral features are an x-ray peak at ~ 12.6 keV and a gamma peak at ~ 9.4 keV. The deviation between background and krypton data begins at the endpoint of the ^{83m}Kr spectrum, ~ 32 keV.

One interesting caveat from that successful krypton run is the fact that we were not able to get up to our standard detector operating voltage. This suggests that there was some surface contamination (from water vapor and other molecules) that prevented the passivated surface from fully standing off the 2700 V bias. Upon further tests, the krypton signal was significantly weaker when running at 2700 V and without those notable spectral features, but those features reappear when running with the detector only able to bias up to 2500 V. These surface effects are very interesting and worth more intense research.

1.14 CAGE

S. Borden, J.A. Detwiler, C. Nave, G. Song, and C. Wiseman

The CAGE Scanner is designed to study High Purity Germanium (HPGe) detector response to potential background sources that penetrate the passivated surface. Radiation that passes

through the passivated surface can become energy degraded, causing normally high energy radiation to be reconstructed into our region of interest. In particular, alpha radiation from the ^{238}U and ^{232}Th decay chains is emitted in the 4-5 MeV range, but can be reconstructed with energies near the 2039 keV $0\nu\beta\beta\text{Q}$ -value.

CAGE uses an Am-241 source to direct a collimated beam of 5 MeV alpha particles onto the passivated surface at specific radii, rotary angles, and incidence angles. This year we completed the hardware upgrades necessary to allow CAGE to accommodate the larger Inverted Coaxial Point Contact (ICPC) detector geometry, updated our electronics, and we began scans to map the response across the passivated surface.

Those hardware upgrades include a redesign of the source collimator, which gives us more confidence in the alignment and position of the beam, and a new holder for the low-mass front-ends (LMFE) that provides a more stable connection between the point contact and the front end electronics. For the collimator, the source is now held in place by a bar that inserts into both sides of the top hat. This eliminates the possibility that the collimator could be inserted at different angles between scans. The lid of the collimator is now held in place by a spring instead of screws, which were difficult to thread tightly into lead and often came loose during thermal cycles. For the front end, we moved away from the original “diving board” design to a crossbar that extends across the detector. This allows the board to resist more of the upward force from the pogo pin, creating a better connection with the point contact, at the expense of obstructing more of the detector surface.



Figure 1.14-1. *Left:* The new collimator design as installed inside the top hat. *Right:* The new crossbar holder for the LMFE fitted onto the ICPC detector.

Our front end electronics were updated to feature a longer second-stage time constant, which gave us a much more linear energy spectrum. Previously, we saw a quadratic shape in our DCR vs. energy plots that had to be manually fitted and removed, rather than the linear distribution centered around $\text{DCR} = 0$ that we expect.

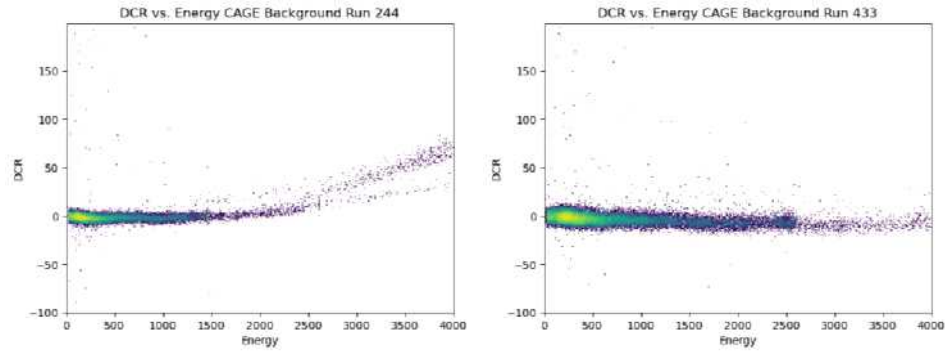


Figure 1.14-2. A comparison of the unwanted quadratic behavior in the DCR vs. Energy plots before (left) and after (right) extending the second-stage time constant of the front end electronics.

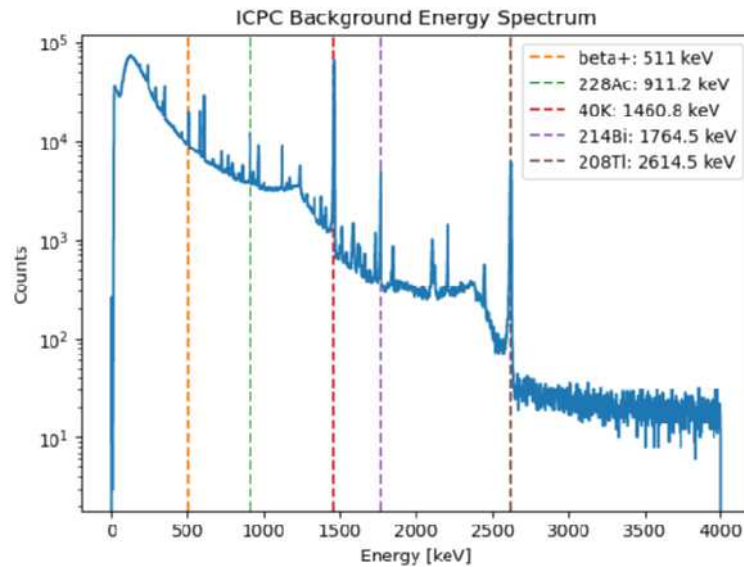


Figure 1.14-3. Background spectrum taken with the ICPC detector. The energies are calibrated with respect to the 40K peak, and the vertical dashed lines mark where we expect to see other prominent peaks.

We have now completed two sets of alpha scans of the ICPC detector, all at normal incidence to the detector surface, while varying the rotary angles and linear radius. We found a 4x longer exposure on ICPC is required to produce a noticeable peak for the 60 keV gamma, compared to our previous scans of the ORTEC PPC Prototype I (OPPI) detector. We also find that this peak grows in strength until a radius of about 7mm, and then decreases again. Similar behavior is found in the alpha rate at rotary angles 145 and 180. Rotary 0 exhibits a notably different behavior.

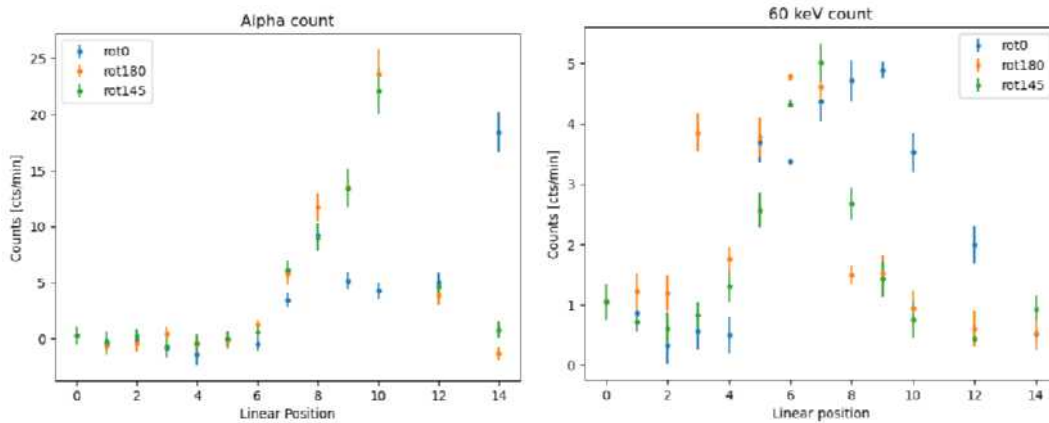


Figure 1.14-4. Rates of alphas and gammas in ICPC linear scans at varying rotary angles.

More studies are required to understand whether the cause of this behavior is irregularities in the passivated surface or systematic effects such as misalignment of the system. We plan to perform more scans with the detector rotated 180 degrees to investigate the discrepancy between the behavior at rotary 0 and the other rotary angles. We also plan to investigate the ICPC ditch, by performing a TUBE style scan across the ditch at a single incidence angle and by scanning the same point at multiple incidence angles, a study which CAGE is uniquely equipped to perform.

1.15 LEGEND L-1000 lock system

J.A. Detwiler, R. Roehnelt, L. Varriano, and C. Wiseman

The UW LEGEND group has taken on the task of designing the lock and shutter system, which will be responsible for inserting and removing fully instrumented strings of germanium detectors into the liquid argon (LAr) cryostat of LEGEND-1000. The system consists of at least one large tube (“mast”) containing the full height of the assembled string and cables, roughly 4 meters. A prototype version of the design shown in Fig. 1 will be built at CENPA before the design is finalized.



Figure 1.15-1. Conceptual view of the lock system. *Left:* Zoom-in on the gate valve system and mounting table as an assembled and purged string is ready to be connected to the cryostat flange and lowered into liquid argon. *Right:* Zoom-out on the lock system, showing the full height of the tall tube which is moved by crane into position above the cryostat. The single-string lock system may be attached to any string flange for insertion or removal of Ge strings. Contamination of UGLAr is minimized by a purge system, and the installation cycle time is minimized to expedite string installation. Multiple lock systems may install strings simultaneously, parallelizing the installation.

The design of the string installation lock is based on experience from GERDA, MAJORANA, and LEGEND-200. In LEGEND-2000, the entire detector array is raised and lowered with a single large-diameter lock. At the scale of LEGEND-1000, this approach is more difficult to justify. For LEGEND-1000, our conceptual design is a “single-string” lock system where each string is fixed to its own flange. A “tall mast” design with its large tube is the primary conceptual design, which incorporates lessons from GERDA and LEGEND-200 avoiding coiling and uncoiling both mechanical supports and low-background cables, at the expense of a large headspace required over the main cryostat, at least as tall as the full length of a deployed string. A clamping system or “lock table” can be attached to a flange, and connected to a tall cylinder which can be cycled with N_2 , AtmAr, and UGLAr gas, to prevent

contamination. Advantages of the single-string lock system include a much simpler mechanical design, partial separation of the lock system from the cryostat design, and importantly provides access to individual strings for repairs or modifications. It will be important to minimize the cycle time of the lock system for individual strings, so that a full deployment cycle for one string takes up no more than a 24 or 48-hour period. If multiple tube systems are procured, multiple strings may be purged at once, connected to common systems such as a gas purge or vacuum flush, before final installation on the cryostat.

The primary components include the tall overhead steel pipe, internal crane system, vacuum pumps and UGAr gas handling systems, a system for moving and aligning the lock with each string flange, the clamp and gate valve system which connects to each string flange, and the controls and interlock systems necessary for monitoring and operation. An internal crane, such as a marine windlass, may be used for lifting the detector array. The crane's acceleration, sway and deployment speed will be determined by the specifications of the string design and the cryostat and array design. Monitoring and validation of the lifting and lowering status will also be implemented. The mechanism to raise and lower a string within the lock must be remotely actuated and able to raise/lower the string, varying speed as necessary during insertion into cryogenics and removal in a gas environment. In-floor or overhead rail systems with gantry cranes may be used to move each lock. We anticipate construction of the first prototype to begin in early 2023.

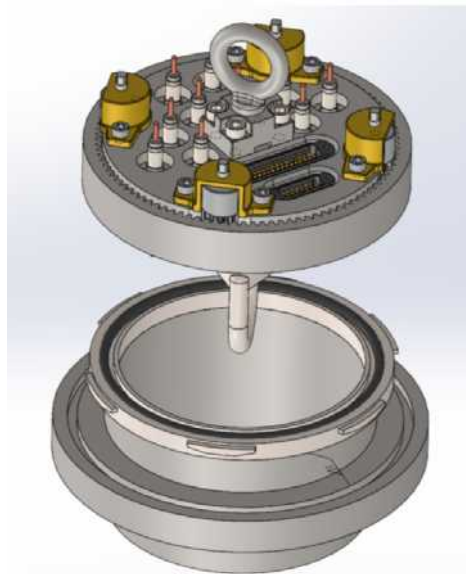


Figure 1.15-2. Conceptual design for the string flange, with 8–10 single-pin HV connections and two 50-pin D-sub connections for the Ge and SiPM signals. Stepper motors actuate the sealing mechanism from within the sealed tube.

1.16 SpIS and 42-Ar

S. Borden, J.A. Detwiler, C. Goodman, and C. Wiseman

Historically, CENPA has operated its tandem accelerator using multiple ion sources. By

2022, only one source was actively in use, the direct extraction ion source (DEIS), limiting the mass range of ions capable of being generated. Recently, there has been an effort to refurbish the sputter ion source (SpIS), an ion source that had not been in operation for 10 years. A functional SpIS would significantly increase the mass range of generated ions, using cesium sputtering of solid targets in order to eject and ionize heavy elements (such as carbon or lithium) that can then be fed through the tandem accelerator. These heavy ions unlock the potential for new science to be done at CENPA.

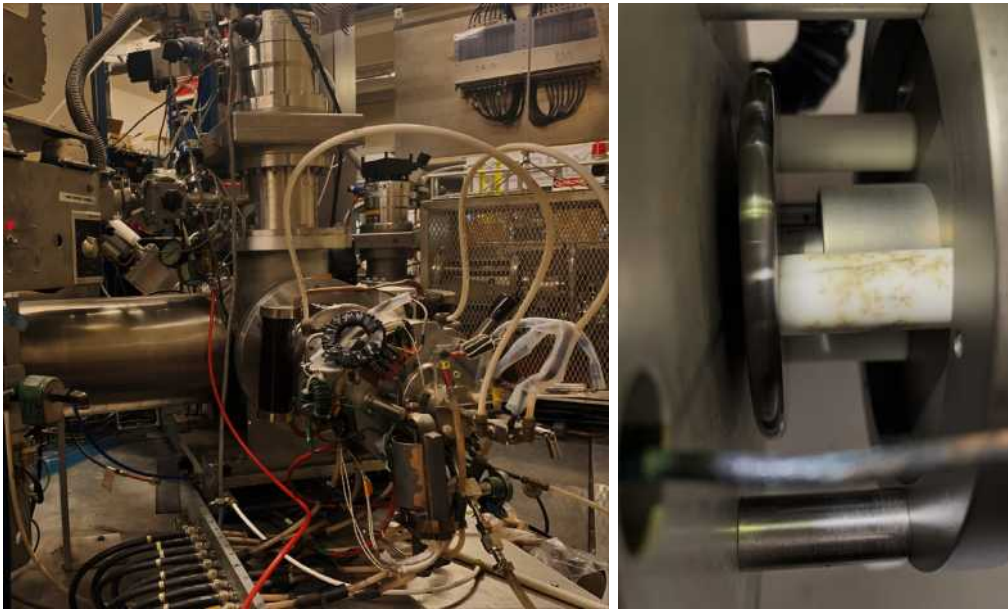


Figure 1.16-1. *Left:* SpIS in-place *Right:* Arc damaged insulator.

In order to recommission the SpIS new documentation had to be made, the source itself had to be disassembled, inspected, cleaned, and reassembled. The disassembly and inspection were done by Brittney Dodson and Cyrus Goodman. During this process, two major maintenance items were noted. Firstly, one of the Macor insulating pegs, responsible for holding a portion of the source at a 10kV bias voltage, was found to be shorted. The old insulators were measured, and replacements were fabricated through the machine shop here at CENPA. Secondly, there is a small cesium oven, external to the main body of the SpIS, that had not been opened or cleaned since the source was last used. A cleaning procedure was written up and the cesium source was rinsed and sonicated. Other than these two maintenance items, the SpIS was found to be in excellent condition. As the source is reassembled, and the electronics tested, it is possible that more will need to be done to get the SpIS into working order.

Once the Sputter Ion Source is functioning, it should be able to generate a lithium-ion beam using a lithium hydroxide cathode. This beam of lithium ions can then be used in conjunction with an ^{40}Ar filled gas cell, to produce ^{42}Ar via the reaction $^{40}\text{Ar}(^7\text{Li}^{3+}, \alpha p)^{42}\text{Ar}$.

1.17 Characterization of silicon photomultipliers at LN temperatures for LEGEND-1000

S. Borden, T. Burrirt, J. A. Detwiler, D. A. Peterson, W. Pettus*, N. W. Ruof, T. D. Van Wechel, and C. Wiseman

LEGEND-1000 will also employ an active liquid argon veto, potentially realized with underground liquid argon. It is therefore more important than ever to have a high light collection efficiency in order to veto the remaining background, and to also have a robust model of each component that contributes to the overall veto efficiency. One such piece comes from the photon detection efficiency (PDE) of the silicon photomultipliers (SiPMs) that L-1000 will be instrumented with for light readout. These SiPMs will be operated at cryogenic temperatures; to date, little research has been done to understand the behavior of the PDE at these cryogenic temperatures.

We have taken our first liquid nitrogen temperature measurement of the PDE for a Ketek SiPM. Analysis of the data indicates quenching of the PDE at lower temperatures, as seen in Fig. 1. We are investigating the physics behind this; the PDE is potentially lower due to lower carrier mobility at LN temperatures, which in turn lowers the avalanche probability. Measurements of the doping profile at room temperature are in progress in order to extend this measurement technique to LN temperatures to verify this hypothesis. There is also evidence that repeated thermal cycling can permanently damage SiPMs.

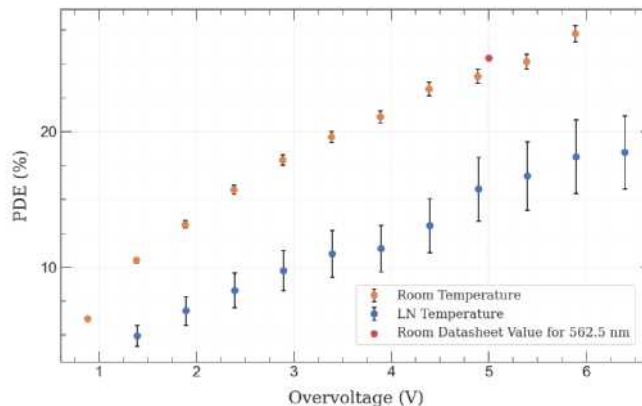


Figure 1.17-1. Precision measurement of the photon detection efficiency of a KETEK SiPM at room and LN temperatures.

Sources of large systematic errors in the experiment are also being identified and fixed. Recently, the impact of SiPM deadtime on the PDE measurement was studied. Results show an up to 10% deviation from the true PDE value for high intensities of impinging light. In order to minimize the dead time, a lower intensity light source must be used; however, the APD previously in use was not sensitive to these lower intensities. The calibrated APD was replaced with a Ketek SiPM with a known PDE at a specified overvoltage. This reference

*Indiana University, Bloomington, IN.

SiPM has helped us eliminate systematic uncertainties, and its more narrowly peaked detector response has also lowered experimental uncertainty.

Selena

1.18 3D track reconstruction in Selena

A.E. Chavarria and X. Ni

We began studying the capabilities of a large Selena detector, shown in figure Fig. 1.18-1. Selena imagers will utilize 5–6 mm-thick layers of amorphous selenium (aSe), which is significantly thicker than the ~ 0.5 mm typically used in flat-panel x-ray imagers. We investigate the 3D spatial resolution of the proposed detector through simulation of β tracks in aSe.

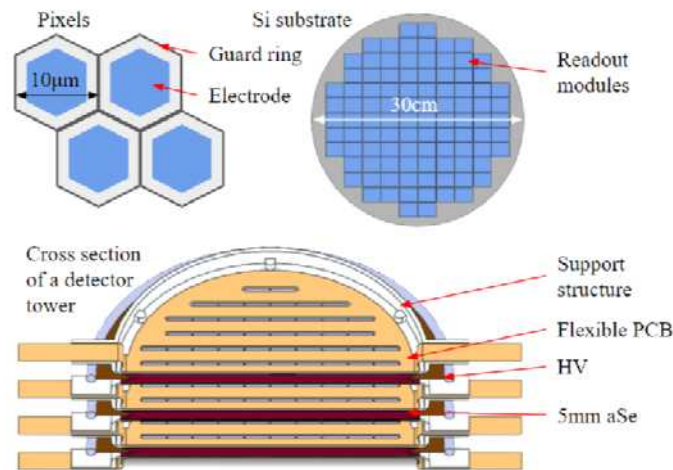


Figure 1.18-1. Conceptual design of a large Selena detector. Each imager consists of a CMOS pixel array covering an entire silicon wafer with 5–6 mm of aSe deposited on its surface. Two back-to-back imagers make a module, which can be stacked to achieve the final target mass.

The simulations are based on particle tracking by Geant4 followed by charge generation, recombination and transport models¹. For 5–6 mm layers of aSe, a 3 MeV β (or $\beta\beta$) track is usually fully contained within the bulk of the module. The ionized charge is drifted toward the pixel array, which consists of 10 μm charge sensing CMOS pixels. A simulated track is shown in Fig. 1.18-2. The spread of the charge on the pixel array (σ_{xy}) is obtained from the diffusion model as:

$$\sigma_{xy} = \sqrt{2 * v_T / E * z_{abs}} \approx \mathcal{O}(1)\mu\text{m}$$

where E is the applied electric field, v_T is the thermal voltage (26 mV at room temperature) and z_{abs} is the absolute z -position of the energy deposit away from the CMOS pixel array.

¹ X. Li, A.E. Chavarria, S. Bogdanovich, C. Galbiati, A. Piers, and B. Polischuk, J. Instrum. **16**, P06018 (2021).

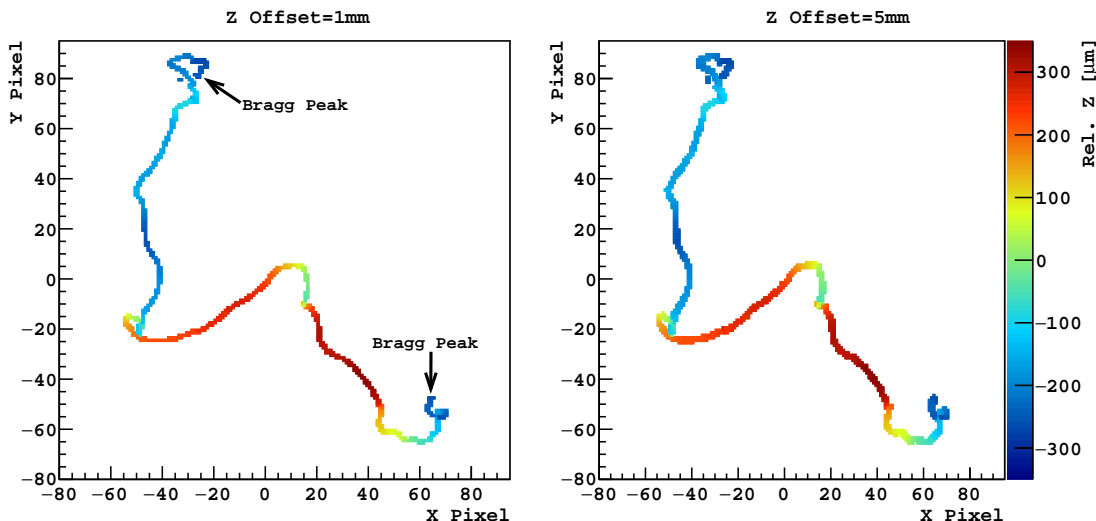


Figure 1.18-2. Simulation of a 3MeV $\beta\beta$ event fully contained in a Selenia imager. The color axis shows the relative z position recovered by TOA. The left and right plots show tracks diffused at different overall z -offsets, which we hope to recover via reconstruction of the charge spread σ_{xy} .

The overall small value of σ_{xy} means that we retain excellent (x, y) spatial resolution and signal-to-noise in our $10 \mu\text{m}$ pixels. On the other hand, this provides less information to extract the absolute z position of the track through diffusion, as is done in the DAMIC experiment. We plan to make up for this by adding a time of arrival (TOA) measurement on our pixels, with a resolution of 20 ns. Using the TOA of the charge on a pixel, we will be able to determine the relative z position of charge (z_{rel}) as:

$$z_{abs} = z_0 + z_{rel}$$

$$z_{rel} = TOA \times \mu_h \times E$$

where μ_h is the mobility of the charge carriers (holes). A resolution of 20 ns in TOA results in $17 \mu\text{m}$ resolution in z_{rel} . The offset z_0 is the point of the track closest to the pixel array, *i.e.*, the point from which the charge is first to arrive to the pixel array. We estimate z_0 from the charge spread σ_{xy} along the track, which together with z_{rel} reconstructed from the TOA provides full z reconstruction.

Our preliminary algorithm on simulated tracks, which aims to correct for contributions from pixelation and the underlying straggling of the β particle to the spatial variance of charge along the track, results in a z_0 resolution of 0.6–1 mm. We hope to improve further by using more advanced image analysis techniques.

1.19 Hybrid aSe/CMOS devices in flip-chip package

A.E. Chavarria, M. Conde, B. Harrop*, X. Li[†], Y. Mei[†], X. Ni, and A. Piers[‡]

We are prototyping a new hybrid device consisting of the Topmetal-II⁻¹ CMOS charge sensor coupled to amorphous Selenium (aSe) in a new flip-chip package. This new design aims to allow for a larger and flatter deposition of aSe over the Topmetal-II⁻. We are able to achieve this by introducing a sapphire interposer with a window cut in the center. The aSe will be deposited over the top of the interposer, while the Topmetal-II⁻ will be flip-chip bonded to the bottom side. We pattern gold traces and pads on the bottom side of the interposer to allow for electrical connections with a newly designed test board. The new design is shown in figure Fig. 1.19-1. In the previous design, the Topmetal-II⁻ was epoxied and wire bonded to a PCB, known as the “post-stamp” package. The wire bonds on the top side of the Topmetal-II⁻ required protection via a nonconductive epoxy and resulted in an uneven deposition of aSe unsuitable for high voltage application.

We faced many delays with the fabrication of these packages. We found that we were limited by both the durability of the sapphire interposer and, mostly, the pads on the Topmetal-II⁻. The former meant that we had to redesign our test board to allow for connection via wire bonding rather than the elastomeric ZEBRA connector. The uneven pressure applied by the connectors resulted in cracks in the sapphire with the window cut. The latter meant that too much pressure on the bonding pad would cause a breakthrough to form between our power lines, shorting our device. We are currently working around this by introducing a thermosonic flip-chip process.

The gold patterning of the sapphire interposer is done at the Washington Nanofabrication Facility (WNF), using a gold evaporation deposition. The window is also cut at UW, using the LPKF laser in NPL.

Flip-chip packaging is a standard industry technique, primarily for use with Chip on Glass (COG) applications such as LED drivers. Typically, gold bumps are placed on the pads of the bare die chip via stud bumps from a ball bonder or an electroplating process. The chip and glass substrate are then placed on a flip-chip bonding machine, which can pick up the bare die and, using beam-splitter optics, align the pads of the bare die to the pads of the substrate. Then, a combination of heat and force is applied to bond the pads together, known as a thermocompression bond. The chip can also be attached using ultrasonic power, known as thermosonic bonding, or via an anisotropic conductive film (ACF).

The initial thermocompression tests were done by B. Harrop at the Nanofabrication Center at Princeton University. Our testing found very low impedance at our power connections on the chip, which meant that the bonding parameters caused a breakthrough of the pads.

*Princeton University, Princeton, NJ.

[†]Lawrence Berkeley National Laboratory, Berkeley, CA.

[‡]Presently at RKF Engineering, Bethesda, MD, 20814-6198.

¹M. An *et al.*, Nucl. Instrum. Methods Phys. Res. A **810**, 144 (2016).

Since the parameters had already been set conservatively, we decided that a thermocompression process was unsuitable for our assembly. Our second prototype involved a layer of ACF spread out across the pads, which required much lower bonding pressure. Unfortunately, we were not able to measure any electrical connection through an ACF bond.

We then shifted the majority of the work from Princeton University to the WNF to speed up the R&D process. The WNF has a flip chip bonder with ultrasonic capabilities, which Princeton does not. On the other hand, the WNF does not have the equipment to meter dispense fluids onto our die and substrate, which is important for application of ACF. Thus, we worked with a thermosonic process.

We utilized the Westbond 4700E ball-wedge wire bonder to place stud bumps onto the pads of the Topmetal-II⁺. We then used the Finetech Fineplacer Pico at the WNF to planarize the bumps and also to flip-chip bond the chip to the interposer.

Unfortunately, we encountered two main problems with the equipment. The first is that the main use of the Westbond bonder is for ball-wedge bonding, so we did not have access to the stud-bump capillary. This resulted in an uneven bump height and shape. In addition, the size of the die and lack of XY translation in the optical setup of the Fineplacer meant that the optics did not provide optical zoom into every pad region. We could only check for alignment of every pad at a far zoom distance and misaligned the pads by $\sim \frac{1}{4} - \frac{1}{2}$ of a pad width across the device.

Despite the limits of the equipment at the WNF, we achieved a mostly successful electrical contact between the device and the substrate. Any further processing will require upgraded tools. These tests have served as a proof of concept for a thermosonic bond between the Topmetal-II⁺ and our sapphire substrate, and we are currently looking to outsource the process to a commercial facility.

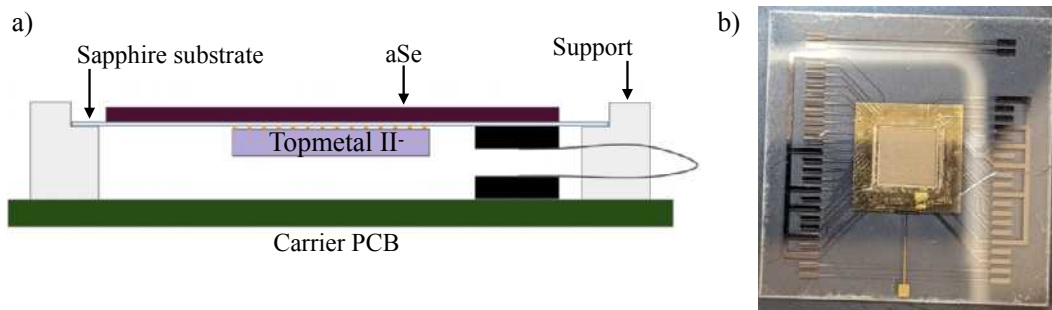


Figure 1.19-1. *Left:* The original proposed package of the Topmetal-II⁺ bonded to the sapphire interposer. Gold bumps interface between the pads on the die and the pads on the substrate. *Right:* Top-view photograph of a completed package.

1.20 Topmetal-Se pixelated CMOS charge sensor

A.E. Chavarria, Y. Mei*, X. Ni, D. Peterson, A. Piers[†], and T. Van Wechel

The TopmetalSe (TMSe) is a pixelated CMOS (complimentary metal-oxide-semiconductor) sensor for the charge readout of amorphous Selenium (aSe), designed for the Selena Neutrino Experiment. The pixels will consist of an exposed topmost metal layer (*topmetal*), which allows for direct coupling to the aSe, and a charge-sensitive amplifier (CSA). We aim for 10–15 μm pixel pitch with $10e^-$ noise. We submitted two prototype designs of the TMSe for tapeout (fabrication) on Skywater/EFabless multi-project wafer (MPW) shuttle runs for the Skywater Open-Source 130nm PDK (Process Design Kit).

The Sky130 Open PDK was released in 2020 as the first ever fully free and open-source PDK and provides access to all the CMOS transistor models and specifications for design of an ASIC (Application Specific Integrated Circuit). EFabless provides the web platform for the PDK and shuttle runs, while the release of the PDK and shuttle runs are sponsored by Google.

The TMSe-V1 was submitted for tapeout in June 2022. The prototype contains two test structures: a 100x100 pixel array and a smaller 3x3 pixel array, with a pixel pitch of 15 μm . The layout of the full device is shown in figure Fig. 1.20-1. Due to many delays from EFabless, we have yet to receive the devices so our understanding of the devices is entirely from simulation. The readout circuitry of each pixel consists of a CSA. From SPICE simulations, we expect $18e^-$ of noise with $< 1\mu\text{W}$ of power consumption per pixel. The pixel *topmetal* layer consists of a $8.2 \times 8.2\mu\text{m}$ collection electrode with a $0.8\mu\text{m}$ surrounding guard ring. From Finite Element Analysis (FEA) simulation in COMSOL, we expect a base collection efficiency of our pixel to be $\sim 63\%$. With a voltage bias on the guard ring, we can expect the collection efficiency to increase to $> 90\%$. The large array is read out in rolling shutter mode, which multiplexes the pixel values onto a single output line. For the testing of the devices, the CENPA Electronics Shop designed a custom test board for the powering and readout of the TMSe-V1. We expect to receive the devices in late June 2023.

*Lawrence Berkeley National Laboratory, Berkeley, CA.

[†]Presently at RKF Engineering, Bethesda, MD, 20814-6198.

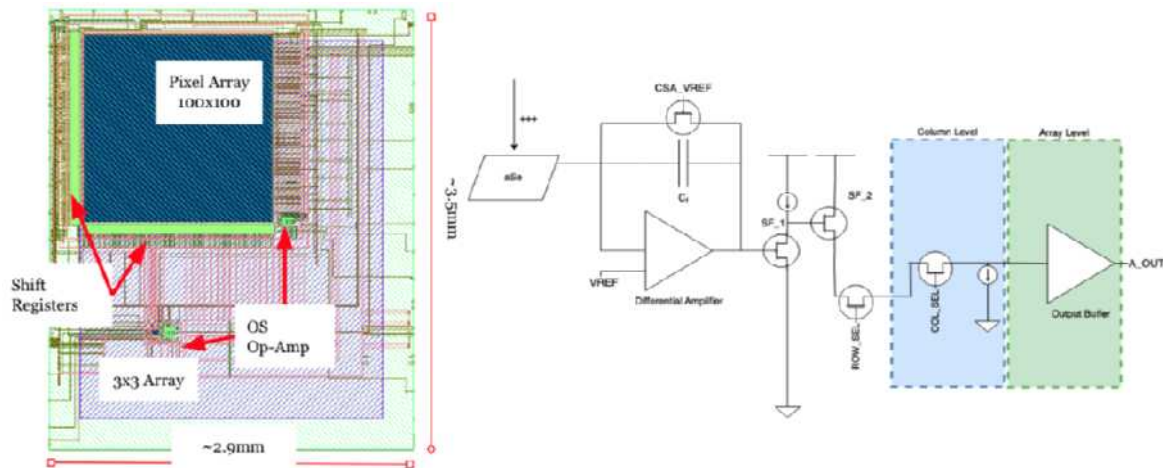


Figure 1.20-1. *Left:* Layout of the full padframe showing different test structures. *Right:* Schematic of pixel

We also submitted a second prototype for tapeout: the TMSe-DPS, which utilizes Digital Pixel Sensor (DPS) readout¹. In this prototype, we implement an 8-bit ramp ADC within each pixel to convert the CSA output into a digital value, to be stored in and read out from an 8-bit DRAM cell. We retain the same pixel geometry and CSA frontend as the TMSe-V1. TMSe-DPS was submitted for tapeout in the Fall of 2022, and (due to delays from EFabless) we now expect these devices in the Fall of 2023.

COHERENT

1.21 NaI(Tl) Crystal Scintillators for the COHERENT Tonne-Scale NaI(Tl) Detector Subsystem

T. Burritt, J. A. Detwiler, M. R. Durand, D. A. Petersen, F. T. Tsai,
T. D. Van Wechel, D. I. Will, and C. Wiseman

The COHERENT project is a collaborative effort to measure coherent elastic neutrino-nucleus scattering ($CE\nu NS$), a Standard-Model process whose precision measurement will allow searches for non-standard interactions of neutrinos with matter and a deeper study of nuclear structure. $CE\nu NS$ is also key process in core-collapse supernova events (Type II SNe), and therefore its study will aid in the understanding of supernova dynamics. $CE\nu NS$ can also be used to detect the neutrinos produced in the core collapse. The $CE\nu NS$ process is also important for understanding the “neutrino floor” background for direct searches for dark matter, arising from $CE\nu NS$ interactions of solar and atmospheric neutrinos.

The COHERENT experiment is based at the Spallation Neutron Source (SNS) at Oak Ridge National Laboratory (ORNL) in Tennessee. The sodium iodide (NaI[Tl]) group at the

¹S. Kleinfelder, S. Lim, X. Liu, and A. Gammal, IEEE J. Solid-State Circuits, **36**, 2049 (2001).

University of Washington has worked with collaborators at Duke University and ORNL to characterize roughly two tons of thallium-doped sodium iodide (NaI[Tl]) crystal scintillators, including roughly 120 7-kg crystals at UW, currently being deployed in NaIvETe, one of the next detector phases of the multiphase approach of the COHERENT collaboration.

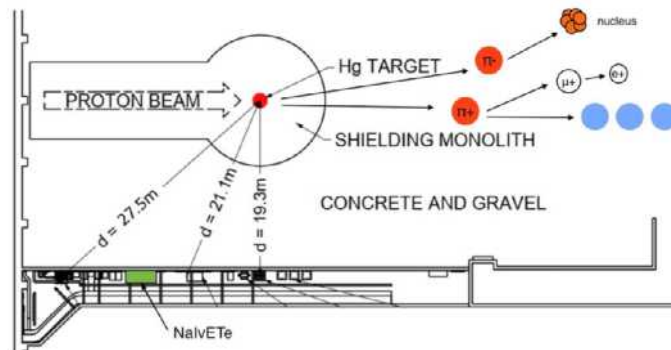


Figure 1.21-1. Diagram of the Spallation Neutron Source at Oak Ridge National Laboratory. The decay products represented by the blue circles are electron neutrinos, muon neutrinos, and anti-muon neutrinos.

NaIvETe, the Sodium-Iodide Neutrino Experiment (Tonne-Scale), is to consist of seven modules of 64 NaI[Tl] crystals deployed in the basement of the SNS at ORNL. Currently, the modules in positions 2 and 3, nicknamed Beta and Gamma respectively, have successfully been deployed and are currently taking beam data. Delta, the next module to be built, is nearly completed and has been loaded with 18 detectors thus far, which are acting as passive shielding for its neighboring module, Gamma.



Figure 1.21-2. A view of the inside of the Gamma module of NaIvETe and the beginning of the frame of the in-progress Delta module. The frame has since been completed, and the module is being loaded.

Along with sending 100 of the crystals characterized at UW to ORNL (several of which are in use in the Beta module), we have also designed, produced, and sent high-voltage distribution panels for use in the current and future models of NaIvETe. The design of these panels was

primarily necessitated by differences in performance across the individual crystals used in the modules. The gain dependence on voltage is not consistent from crystal to crystal, and the distribution panels are therefore designed such that each of the 64 outputs can produce different bias voltages depending on what is necessary for each crystal.



Figure 1.21-3. Part of the board of one of the high-voltage distribution panels sitting on top of its to-be-installed face plate. The blue boxes are variable resistors, allowing each output to be tuned to the ideal voltage for its respective crystal.

One of the distribution panels is currently set aside for a continuation of the crystal characterization campaign. The UW's main contribution to this campaign was completed as of last year, however there are a great many crystals that have been stored on-site at ORNL that still awaited characterization to determine performance specifications and, most importantly, check for insufficient resolution, impurities, or even damage. Using the distribution panel, a low-voltage distribution board from our collaborators at Duke, vertical racks that each fit 12 crystals, and making adjustments to the procedure, we were able to parallelize crystal characterization to do 24 at a time, greatly speeding up the process. Whereas it previously took about 3 hours per individual crystal, up to two full batches of 24 crystals can now be fully characterized in the span of a single work day. After the conclusion of this beam period, on-site efforts will turn to completing the Delta module, which largely only needs to be loaded with its remaining crystals, quality-checked, and gain-matched.



Figure 1.21-4. Loaded racks of 12 crystals each for parallelized crystal characterization.

An additional study that is now completed is an investigation of the background intrinsic to the NaI[Tl] detectors, primarily due to potassium impurities in the crystals. As the detectors were not initially produced with the intention of executing precision measurements, they are contaminated with varying amounts of potassium from the growth process. $CE\nu NS$ is a rare signal that will show up in the low-energy region of our data. The background due to the potassium in the crystals cannot be shielded or removed in any way, so it is important that we understand it well. To investigate this intrinsic background, four detectors were placed into a box of lead bricks to shield from environmental background. Test data has been taken and its analysis is now completed, and the measurement will also be simulated using the `g4simple` software for comparison. The “lead box” has now been dismantled and the four detectors within have been removed.

2 Fundamental symmetries and non-accelerator-based weak interactions

Torsion-balance experiments

2.1 In-Vacuum Rotation Sensors for the LIGO Seismic Isolation

S. Apple, C. Gettings, J. H. Gundlach, M. P. Ross, E. A. Shaw, and J. Turnbull

The LIGO observatories employ a multi-stage seismic isolation to allow for gravitational wave detection without interference from seismic motion. The primary stage of the isolation is the in-vacuum dual-stage seismic isolation platforms. These platforms use a series of on-board seismometers placed in feedback to inertially isolate the platform in all six degrees-of-freedom.

Currently, the rotational degrees of freedom are sensed by the difference between pairs of spatially separated seismometers. The current state-of-the-art seismometers have rising noise at low frequencies. This limits the performance of the isolation below ~ 0.1 Hz. The low-frequency performance of the isolation bleeds into the gravitational wave detection band and is a limited noise source below 30 Hz.

We have developed the Cylindrical Rotation Sensor (CRS), shown in Fig. 2.1-1, to address this issue. It consists of a monolithic cylindrical proof-mass suspended by a pair of $10\ \mu\text{m}$ BeCu flexures. This forms a rotational spring-mass system that isolates the proof-mass from motion of the platform. The angle between the platform and the proof-mass is recorded with a pair of homodyne interferometers. As the proof-mass is inertial, this provides a high-fidelity measure of the platform's motion.

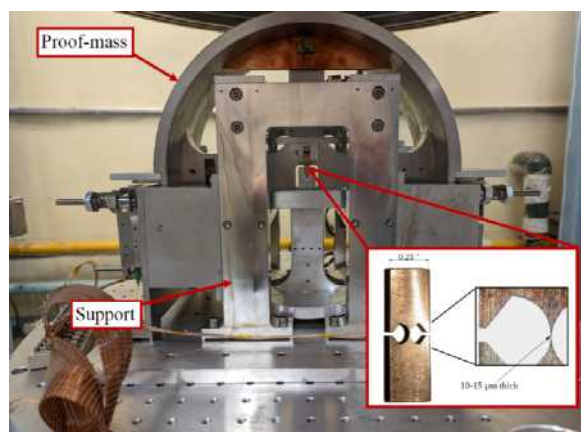


Figure 2.1-1. Picture of the Cylindrical Rotation Sensor prototype along with microscope images of the flexures which suspend the proof-mass.

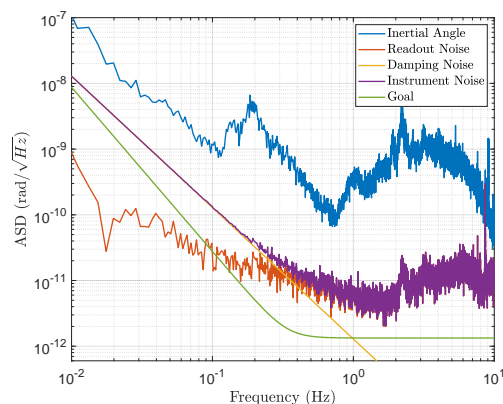


Figure 2.1-2. Amplitude spectral density of the inertial angle, readout noise, external damping noise estimate, total sensor noise and the performance goal.

We've constructed a prototype CRS at CENPA inside a large bell-jar vacuum chamber. This allowed us to test and eliminate a variety of noise sources. Namely, we found that ambient

seismic motion can couple into the interferometer readouts through the fiber optics that provide the laser light to each interferometer. This will not be present in the quiet seismic environment of the LIGO platform. As such, we have attached a broadband three-axis seismometer to the chamber and subtract away this noise within the data stream.

The performance of the prototype is shown in Fig. 2.1-2. The sensor reaches $5 \text{ prad}/\sqrt{\text{Hz}}$ at 1.5 Hz. This is an order of magnitude better than existing state-of-the-art rotation sensors. Below 0.5 Hz, the prototype is two orders of magnitude more sensitive than the sensors currently deployed at LIGO.

With the success of the prototype, we are now moving towards producing sensors to be installed at LIGO. LIGO is currently in its fourth observing run, which will last until the end of 2024. After which, we plan to install a number of CRSs at the observatories. We expect this to allow for the observation of gravitational waves below 30 Hz.

2.2 Update on the Rotating Equivalence Principle Experiment

S. Apple, C. Gettings, J. H. Gundlach, M. P. Ross, E. A. Shaw, and J. Turnbull

The Equivalence Principle (EP) is described in Newtonian physics as the equivalence of the inertial (m_i) and gravitational (m_g) masses of test bodies, where $F = m_i a = GMm_g/r^2$. General Relativity (GR) expands on this description by stating that all objects in free-fall, regardless of their composition, will follow geodesics according to the curvature of space-time. Therefore, tests of the EP not only test GR but allow searches for a new fifth force in nature that doesn't adhere to the EP. Our group has developed a rotating torsion balance test of the EP that's sensitive over length scales from the laboratory ($\sim 1 \text{ m}$) to the galactic center ($\sim 10^{20} \text{ m}$) for a range of possible composition dipoles.

Improvements have been made to the rotating EP test since the last scientific run. These have revolved around replacing the tungsten fibre that suspends the pendulum with one made from fused silica. Fused silica has a much higher intrinsic mechanical Q-factor ($\sim 260,000$ compared to $\sim 5,000$) leading to a much lower thermal noise in the apparatus. Additionally, the ageing DAQ and turntable control hardware and software have been updated; the custom electronics and C# program have been replaced with a dedicated centralised cRIO-9040 CompactRIO FPGA capable controller running on LabVIEW software. This is important as the novel rotating aspect of this EP test, in addition to the new fused silica fibre, is what allows it to achieve sensitivities beyond conventional stationary torsion balance EP tests. Thus better control of this turntable reduces error in the signal frequency and further increases the experiment's sensitivity.

The improvement in sensitivity is highlighted in Fig. 2.2-3 and Fig. 2.2-4. Fig. 2.2-3 is an amplitude spectral density (ASD) plot comparing the error in turntable angle of a previous scientific run which used a tungsten fibre and the old turntable control hardware and software (blue trace) with a more recent test run utilising the aforementioned improvements (orange trace). There is a clear reduction in error of several orders of magnitude across the full frequency range. Fig. 2.2-4 is an ASD plot comparing the torque noise of an inverse square

law (ISL) test with a tungsten fibre (blue trace) and that of the current rotating EP test with a fused silica fibre (orange trace). At low frequencies the noise in the EP test is superior and limited by the thermal noise of the fibre (green trace) which assumes a Q-factor of 260,000.

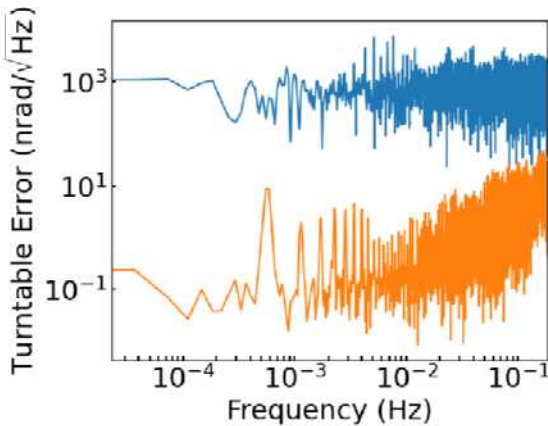


Figure 2.2-3. An ASD plot comparing the error in turntable angle of an EP test which used a tungsten fibre and an old controller (blue trace) with a more recent test run utilising a fused silica fibre and new controller (orange trace).

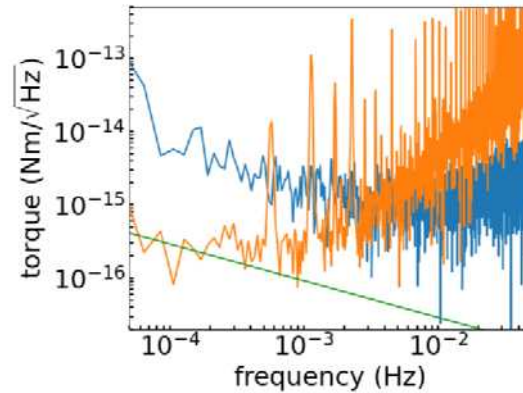


Figure 2.2-4. An ASD plot comparing the torque noise of an ISL test with a tungsten fibre (blue trace) with the EP test with a fused silica fibre (orange trace) and the thermal noise assuming a Q-factor of 260,000 (green trace).

At higher frequencies in Fig. 2.2-4, the rotating EP test's torque noise becomes dominated by turntable harmonics as well as autocollimator noise. The turntable harmonics can be mitigated by improving the turntable controller feedback routine and the autocollimator is being investigated for improvements to reduce its high frequency noise. An additional noise source is the quality of the vacuum. There were issues related to the ion pump high voltage feed-through that led to pressure spikes in the experiment's vacuum chamber. This feed-through has since been replaced and the frequency of the pressure spikes has decreased, but is being investigated further.

With the aforementioned improvements that have been made and the possible improvements to the turntable harmonics, autocollimator noise, and ion pump electronics, a scientific run of the rotating EP experiment using the sun as a source is planned for the immediate future. Furthermore, following the future installation of the in-situ gradiometer detailed in (Sec. 2.3), a scientific run using a local source will be conducted. Both of these runs should improve on the results reported previously.

2.3 Advancements in Gravity Gradiometry

S. Apple, C. Gettings, J. H. Gundlach, M. P. Ross, E. A. Shaw, and J. Turnbull

Tests of the Equivalence Principle are currently limited in precision by systematics, the largest of which being gravity gradients¹. These gravity gradients need to be frequently tracked as

¹T.A.Wagner et. al., *Classical and Quantum Gravity* **29**, 184002 (2012).

the local mass distribution changes over the course of a data run, due to rain and human activity. Current efforts in sensing these gradients have led us to construct a gradiometer that can be directly placed on the science pendulum instrument, allowing for rapid tracking of unwanted gravitational signals at the exact Equivalence Principle test location. We designed and built the gradiometer shown in Fig. 2.3-5.

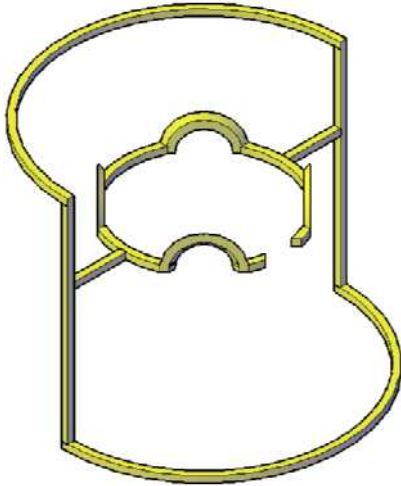


Figure 2.3-5. CAD Rendering of the Gradiometer.

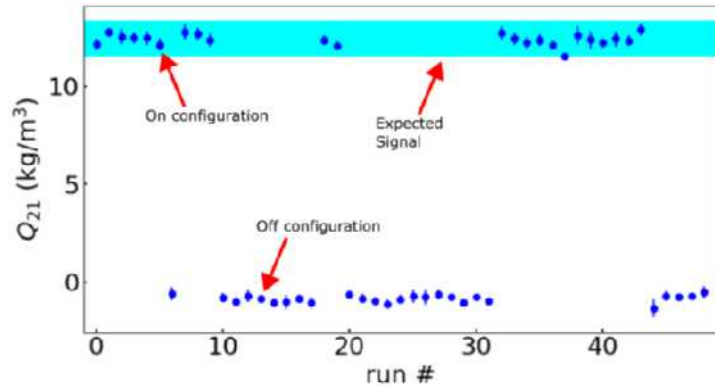


Figure 2.3-6. Gravitational signal for different gradiometer configurations. Here, Q_{21} refers to the gravitational gradient of main interest.

Alongside the gradiometer, we also created a vertical stage that allows us to put the gradiometer on and take the gradiometer off the torsion pendulum in vacuum. With everything in a test chamber, we induced a gravitational signal by using a turntable with two known masses and found our observed signal matched the expected signal from point-gravity simulation, shown in Fig. 2.3-6.

Further use of this gradiometer system require incorporation into the main "science" pendulum, where the vertical stage will need modification to reduce electromagnetic signals from its motor.

3 Accelerator-based physics

3.1 ${}^6\text{He}$ Overview

W. A. Byron, N. Buzinsky, W. Degraw, B. Dodson, M. Fertl*, D. Fredin, A. García, H. Harrington, L. Hayen[†], B. Maxwell, D. McClain[‡], D. Melconian[‡], P. Mueller**, N. S. Oblath[‡], T. Rylander, G. Savard**, E. B. Smith, D. Stancil[†], D. W. Storm, H. E. Swanson, R. J. Taylor[†], J. Tedeschi[‡], M. W. Thomas, B. A. VanDevender[‡], F. Wietfeldt^{††}, A. R. Young[†], and X. Zhu

He6-CRES is progressing toward high precision measurements of the ${}^6\text{He}$ and ${}^{19}\text{Ne}$ beta spectra. Our first publication is now in press¹. The motivation is a high-sensitivity search for chirality-flipping interactions, which would signal physics beyond the Standard Model. Using an effective Lagrangian for the charged weak current with additional scalar and tensor interactions with couplings ϵ_S and ϵ_T ²

$$\begin{aligned} \mathcal{L}_{\text{CC}} = & -\sqrt{2}G_{\text{F}}^0 V_{\text{ud}} \left[\bar{e}^L \gamma_{\mu} \nu_e^L \cdot \bar{u} \gamma^{\mu} (1 - \gamma^5) d \right. \\ & + \epsilon_S \bar{e}^R \nu_e^L \cdot \bar{u} d \\ & \left. + \epsilon_T \bar{e}^R \sigma_{\mu\nu} \nu_e^L \cdot \bar{u} \sigma^{\mu\nu} (1 - \gamma^5) d \right] \end{aligned} \quad (1)$$

the beta spectra, $\frac{dN}{dE}$, are expected to present a distortion with respect to the Standard Model prescription, $\frac{dN_{\text{SM}}}{dE}$, proportional to m/E (the ratio of the mass to total relativistic energy of the beta):

$$\frac{dN}{dE} = \frac{dN_{\text{SM}}}{dE} \left(1 + b \frac{m}{E} \right). \quad (2)$$

The so-called Fierz interference coefficient, b , is directly proportional to the couplings ϵ_S and ϵ_T .

Fig. 3.1-1(left) exemplifies the type of expected distortion, and Fig. 3.1-1(right) gives the sensitivity for $b < 10^{-3}$ measurements in comparison to other determinations³. Significantly, we are aiming for searches that are beyond the level of sensitivity of any previous experiment.

We use the technique called Cyclotron Radiation Emission Spectroscopy (CRES), developed by the Project 8 collaboration, for determining the neutrino mass using the tritium

*Johannes Gutenberg University Mainz.

[†]Department of Physics, North Carolina State University, Raleigh, NC.

[‡]Texas A&M, College Station, TX.

**Argonne National Laboratory, Lemont, IL.

[‡]Pacific Northwest National Laboratory, WA.

^{††}Department of Physics, Tulane University, New Orleans, LA.

¹Byron et al., Phys. Rev. Lett. in press, <https://arxiv.org/abs/2209.02870>.

²Bhattacharya et al., Phys. Rev. D **85**, 054512 (2012).

³M. Gonzalez-Alonso, O. Naviliat-Cuncic, and N. Severijns, Prog. Part. Nucl. Phys. **104**, 165 (2019).

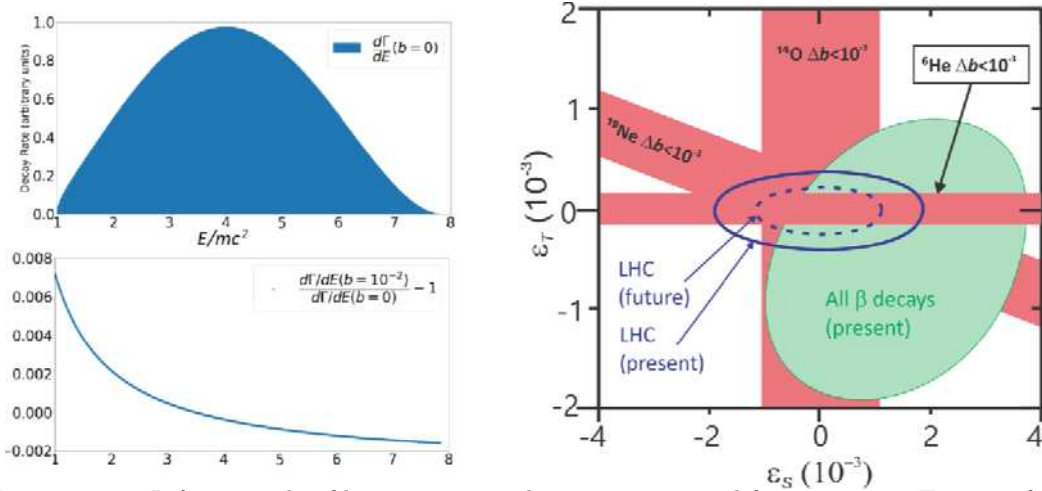


Figure 3.1-1. *Left:* example of beta-spectrum distortion expected from non-zero Fierz coefficient b . *Right:* sensitivities to scalar and tensor couplings from upper limits on b expected from the He6-CRES nuclei in red. In green, we show the result of a combination of all beta decay measurements up to date, including neutron decays. The blue lines indicate limits from the LHC.

endpoint. The basic idea is to arrange for the beta decays to occur within a magnetic field. The betas undergo cyclotron motion with frequency

$$f = \frac{qBc^2}{2\pi E}. \tag{3}$$

For $E \approx 1$ MeV in a ≈ 1 T field, the frequency is ≈ 20 GHz. Letting the radioactive decays to occur within an RF waveguide generates RF excitations with the cyclotron frequency. Typically, we digitize RF waves in slices of $\approx 15 \mu\text{s}$, calculate FFTs, and produce spectrograms, called ‘waterfall’ plots, which allow extraction of E at the point of decay, before any significant loss of energy. The latter feature, combined with low backgrounds, and a first-principles connection between the measured frequency and the energy, are very attractive for a method aimed at probing for new physics.

Our present RF-bandwidth covers 18-19.1 GHz, and the coverage of the beta spectra is achieved by scanning the magnetic field, as shown in Fig. 3.1-2.

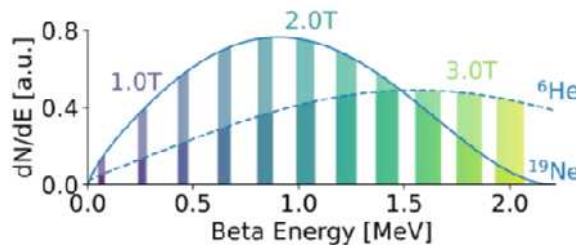


Figure 3.1-2. Sketch of ${}^6\text{He}$ and ${}^{19}\text{Ne}$ beta spectra with bands indicating the regions measured simultaneously by a 18 – 19.1 GHz RF-bandwidth system.

Fig. 3.1-3 shows the main RF components. Careful attention was put into the distribution of heat in the design to allow for optimal temperatures at the Low Noise Amplifiers (LNAs), while keeping the decay cell at warm enough to avoid freezing ^83Kr , which was used as a calibration source.

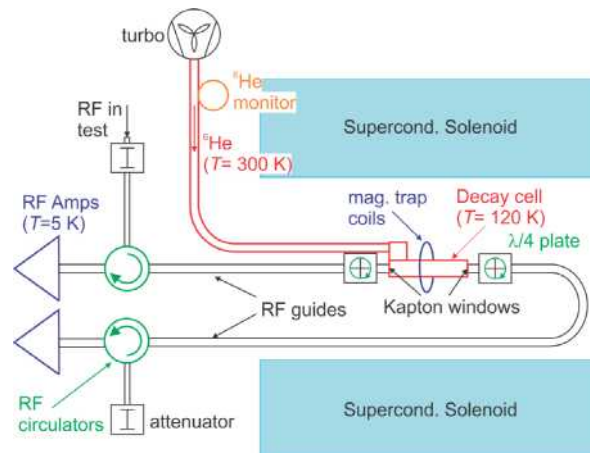


Figure 3.1-3. Sketch of components for He6-CRES. The radioactivity is compressed by a turbo pump into a decay cell, which is part of an RF guide. As shown here, the guide was connected on both ends to RF Low Noise Amplifiers (at ≈ 5 K) to minimize issues related to Doppler effects. Modifications are discussed in (Sec. 3.4). An ambient receiver box, not shown, mixes down the LNA signals to be digitized at several GHz. The ^6He monitor measures beta rates in a manner insensitive to magnetic fields, and allows for normalizing spectra taken at different field values.

He6-CRES is organized into phases with milestones that are presented in Table 3.1-1. We report here on progress since Sept 2021. We have finished Phase I and are starting with Phase II. During the last period, we demonstrated detection of β^\pm in the range between 5 keV and 2.3 MeV. Data were collected at 11 B -field values between 0.75 T and 3.25 T, ratios of counts measured at a given field from ^{19}Ne and ^6He were determined, and yielded a demonstration of how a search for chirality-flipping currents would be done. Details are shown in (Sec. 3.2). In measuring betas at the higher fields, we were surprised to find that their energy loss due to radiation followed closely the Larmor radiation formula for free space: we had assumed that the RF waveguide would act as a suppressor of any mode that was not in the 18-19.1 GHz bandwidth. (Sec. 3.3) shows that once we took into account higher harmonics, we were able to reproduce the measured energy loss. Tracking of events and identification of the initial frequency is important for accurate spectral determinations. Much work was done to understand variations of noise and signal versus frequency, as shown in (Sec. 3.4). The experiment is based on having good sources of ^{19}Ne and ^6He : some updates are given in (Sec. 3.5).

Phase I: <i>proof of principle</i> ; Observe ^{83}Kr lines; Understand RF issues and spectra; Study RF power distribution; Develop ^{19}Ne source. Show detection of cycl. radiation from ^6He ;
Phase II: <i>first measurement ($b < 10^{-2}$)</i> ; ^6He and ^{19}Ne measurements; Develop design of ion-trap systems.
Phase III: <i>ultimate measurement ($b < 10^{-3}$)</i> ; Develop and build ^{14}O source; ^{14}O measurements; Use ion-trap for no limitation from geometric effect.

Table 3.1-1. He6-CRES phases with proposed milestones.

3.2 First CRES Data with ^6He and ^{19}Ne

W. A. Byron, N. Buzinsky, W. Degraw, B. Dodson, M. Fertl*, D. Fredin, A. García, H. Harrington, L. Hayen[†], B. Maxwell, D. McClain[‡], D. Melconian[‡], P. Mueller**, N. S. Oblath[‡], T. Rylander, G. Savard**, E. B. Smith, D. Stancil[†], D. W. Storm, H. E. Swanson, R. J. Taylor[†], J. Tedeschi[‡], M. W. Thomas, B. A. VanDevender[‡], F. Wietfeldt^{††}, A. R. Young[†], and X. Zhu

In 2022-2023, the He6-CRES team has been focused on taking data with our two beta-decay sources: ^6He and ^{19}Ne . This has been the first detection of MeV-scale β^\pm s produced by the decays of ^6He (β^- endpoint ≈ 3508 keV) and ^{19}Ne (β^+ endpoint ≈ 2216 keV) with CRES. In our first data run we collected 92 minutes of ^6He data over two days in August 2022 and then 92 minutes of ^{19}Ne data over two days in October 2022.

For each isotope, we took data at 11 different fields from 0.75T to 3.25T in 0.25T intervals. This procedure allows us to sweep our energy window, set by the main field and the present 1.1 GHz frequency bandwidth, across the two beta spectra of interest. This is shown in Fig. 3.1-2.

Fig. 3.2-2 shows 3 seconds of reconstructed tracks per main field setting from the ^{19}Ne run. While tracks from low-energy betas, such as those from ^{83}Kr that we presented in last year's annual report, are characterized by frequent inelastic scattering with residual gas in the decay cell, the scattering cross-section falls off at higher energies. The result was that for $\sim\text{MeV}$ scale betas we observed long, contiguous tracks as shown in Fig. 3.2-1.

*Johannes Gutenberg University Mainz.

[†]Department of Physics, North Carolina State University, Raleigh, NC.

[‡]Texas A&M, College Station, TX.

**Argonne National Laboratory, Lemont, IL.

[‡]Pacific Northwest National Laboratory, WA.

^{††}Department of Physics, Tulane University, New Orleans, LA.

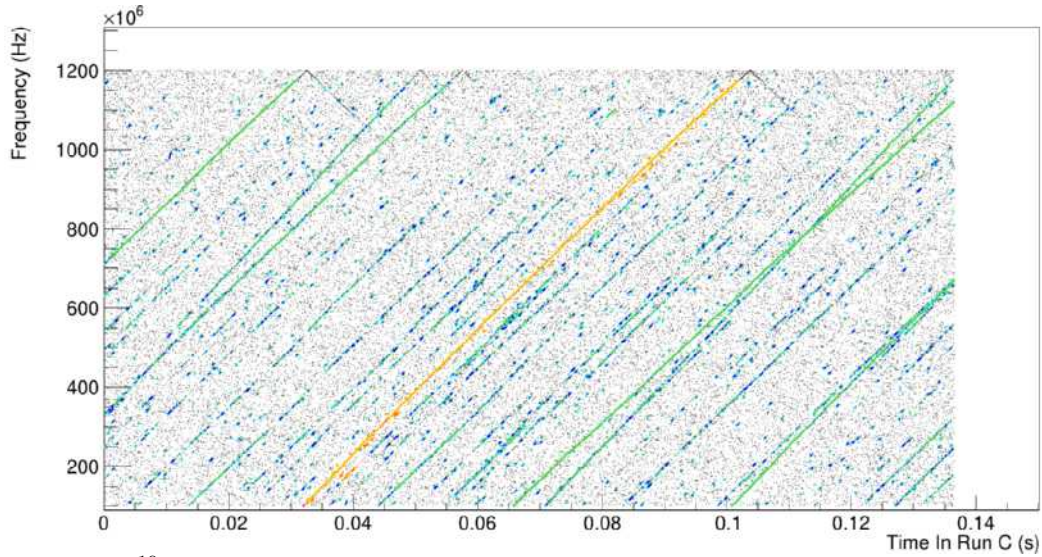


Figure 3.2-1. ^{19}Ne tracks from March 2022 taken at 1.50T with a constant trap. Yellow is an example of a single event as identified by Katydid.

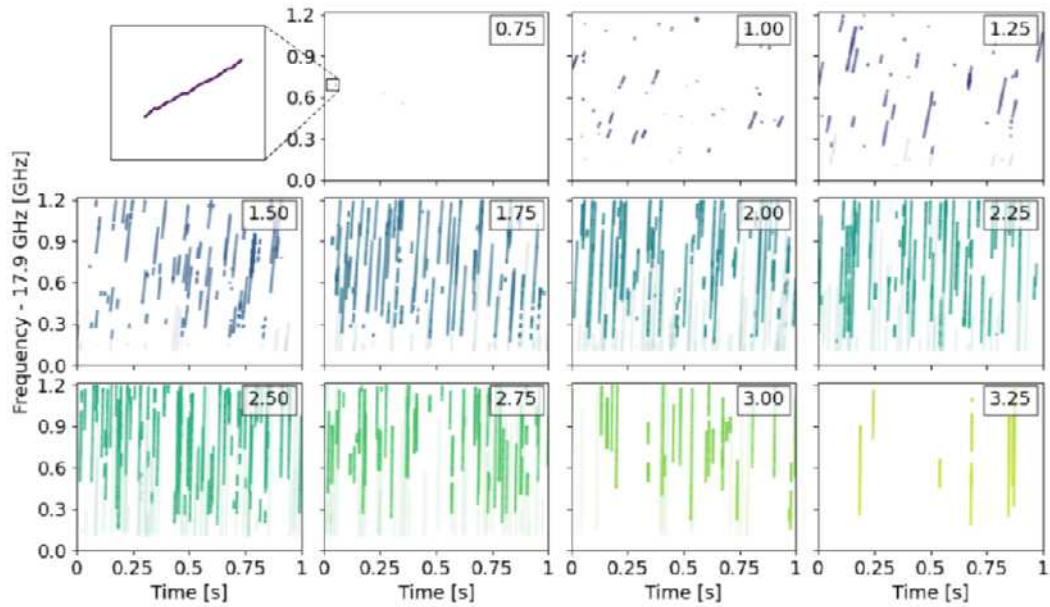


Figure 3.2-2. ^{19}Ne CRES data taken at 11 different fields. Each subplot contains data from 3 seconds of data. Colors are instantaneous reconstructed energy colored by the above spectra.

This first data run allowed us to learn a great deal about extending the CRES technique to higher energies. Important observations included:

- Mean track slopes, a measure of the total energy loss by the beta to cyclotron radiation, were well predicted by the relativistic Larmor formula in free space. We were surprised by this observation, as we had expected the power loss to be suppressed due to only being able to radiate into the lowest propagating mode (TE_{11}) in the waveguide system. This observation led us to develop robust simulations showing that, even for circular axial trajectories, there is radiation at higher harmonics of the cyclotron frequency into many modes. (Fig. 3.2-3)
- Tracks could no longer be well described by a straight line. Instead, they had curves. It was observed that the track slopes increased at certain frequencies, and that some of these resonances could be described by the cut-offs of the guide modes mentioned above. Increasingly sophisticated simulation of this are in development. (Fig. 3.2-4)
- Low scattering meant that betas persisted in the trap for long periods of time, losing energy to radiation. This meant that betas that originated outside our observation bandwidth at a higher energy would lose energy, increasing in frequency until they entered our bandwidth from below. To mitigate the build up of track density, we periodically emptied the trap by slewing the trapping field every 35 ms. In this time, some tracks still entered the bandwidth from below. Fig. 3.2-2 shows an attempt to veto these tracks with a start-frequency cut. Cut tracks are shown with a lower alpha.
- Our experiment had a frequency-dependent SNR. This led to a frequency-dependent track-reconstruction efficiency and to lower power long tracks being fragmented as they passed through low-SNR frequency regions. We determined that this was due to partially reflecting cavities in our RF system. Significant effort has been made on this front, and we have made progress towards solving this with hardware improvements.

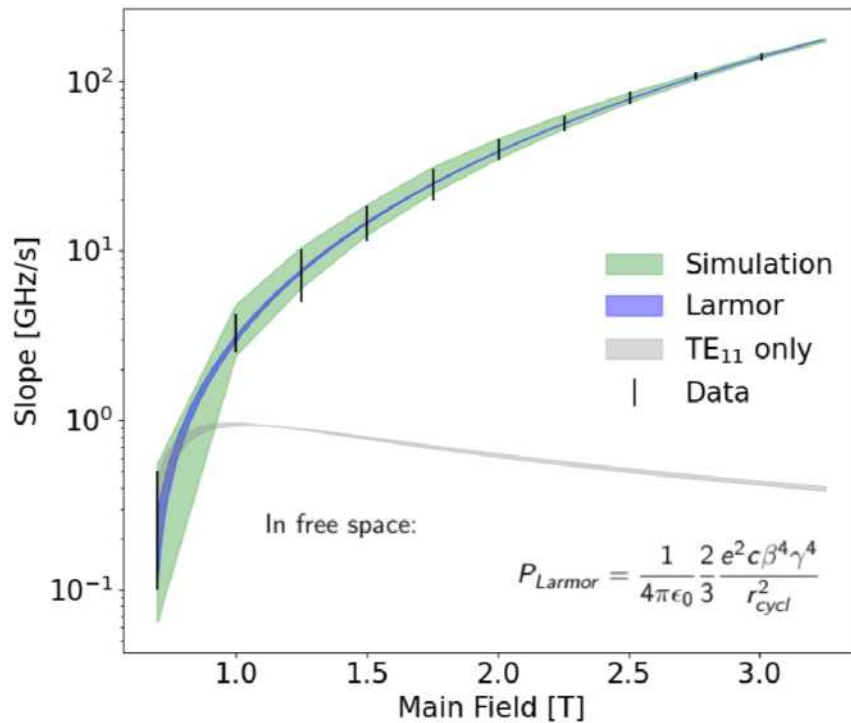


Figure 3.2-3. Observed track slopes (df_c/dt) versus magnetic field for ^{19}Ne and ^6He , showing agreement with numerical waveguide simulations (green) and the Larmor formula (blue), and comparing to coupling to $\text{TE}_{1,1}$ mode only (gray).

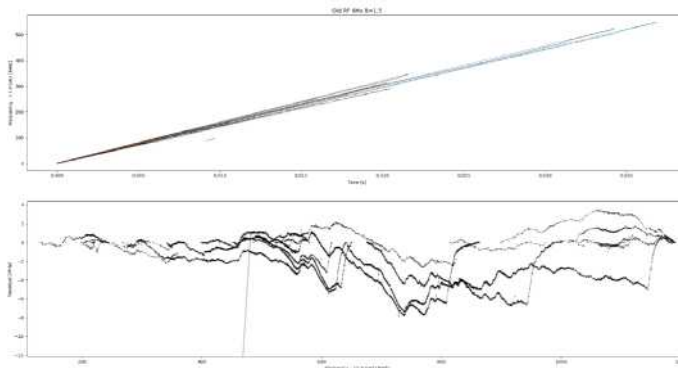


Figure 3.2-4. Tracks taken while slewing the trap at 1.50T and their residuals from straight lines. Some features at the ends of tracks are due to the trap not turning off instantaneously, but other features are not.

With this data, we were able to make a plot of the ratio of observed $^{19}\text{Ne}/^6\text{He}$ counts binned by field. The goal of this was to cancel many energy-dependent efficiencies, such as wall collisions. The frequency-dependent SNR made cuts, such as the start-frequency, cut difficult. Additionally, the gap between the two data runs ended up causing some issues, as the RF noise floor changed between the two runs. This meant that SNR based cuts to remove sidebands or fragmented tracks could not easily be made equal for the two data sets. We thus used the full data set with no significant cuts, and made a model of the SM expected ratio

assuming no scattering and modeling how many events would come up from below including the spectral shape, slope, and period where the trap was on. From studies of the track length across fields, we found that the track length distributions for ${}^6\text{He}$ and ${}^{19}\text{Ne}$ were significantly different below 1.25T, indicating different scattering environments. In particular, the vacuum while running the ${}^{19}\text{Ne}$ was notably worse. (This was later fixed after finding a leak). In order to not need to model scattering, we did not include data below 1.25T in the ratio plot (Fig. 3.2-5). The dashed green lines show what we would expect for $b = \pm 1$.

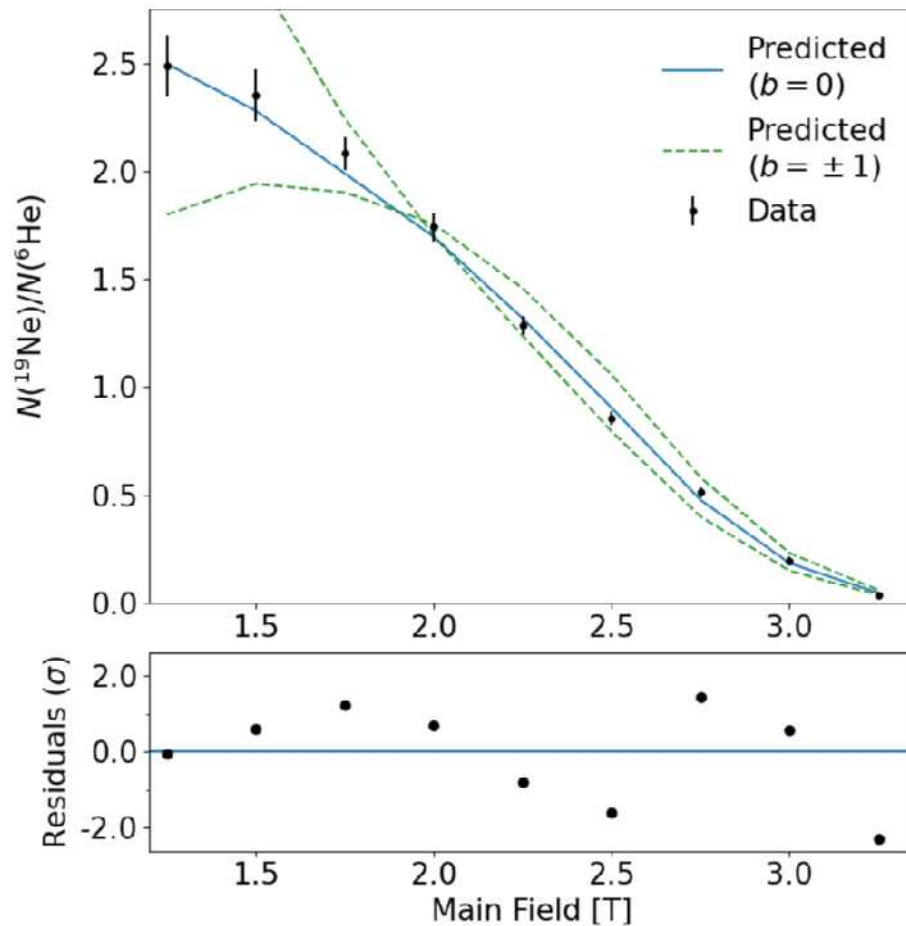


Figure 3.2-5. Spectral ratio plot of ${}^{19}\text{Ne}/{}^6\text{He}$ observed with CRES, including residuals with respect to Monte Carlo (lower inset). Data for all points corresponds to 184 minutes (92 for each isotope.)

3.3 CRES Track Slopes and Radiated Power

W. A. Byron, N. Buzinsky, W. Degraw, B. Dodson, M. Fertl*, D. Fredin, A. García, H. Harrington, L. Hayen†, B. Maxwell, D. McClain‡, D. Melconian‡, P. Mueller**, N. S. Oblath‡, T. Rylander, G. Savard**, E. B. Smith, D. Stancil†, D. W. Storm H. E. Swanson, R.J. Taylor†, J. Tedeschi‡, M. W. Thomas, B. A. VanDevender‡, F. Wietfeldt††, A. R. Young†, and X. Zhu

Besides its primary scientific purpose as a probe of BSM physics, He6-CRES offers a unique experimental window into the radiation of charged particles in a waveguide via the track slope, $\frac{df_c}{dt}$. Track slopes are positively-sloped in time-frequency space as the cyclotron radiation decreases the energy of the underlying charged particle:

$$\frac{df_c}{dt} = -\frac{df_c}{dE} \frac{dE}{dt}. \quad (1)$$

Experimental CRES slopes in a circular waveguide are observed to be broadly consistent with the naive expectation for the free-space result, from the Larmor formula, scaling with the Lorentz factor of the underlying beta as γ^4 (Fig. 3.2-3).

We have been able to derive analytic forms for the power radiated by a (generally) off-axis beta into an arbitrary waveguide mode, in both circular and rectangular waveguides. After implementation into object-oriented C++ with the `c-urchin`² package, direct evaluation of the power radiated by a beta into a waveguide resulted in a $\times 10^6$ reduced computational time cost, compared to a previous iteration using numerical line integrals in Python. This performance boost allows a significantly broader scope for future waveguide Monte Carlo studies.

Analytic and numerical methods has unveiled greater clarity regarding the correspondence to the Larmor power limit for relativistic betas in a waveguide. Fig. 3.3-1 illustrates the power emitted by a beta in a given circular and rectangular waveguide, in comparison to free-space, as a function of frequency. While the TE mode structure of the waveguide results in fluctuations in the power emitted in a given mode, on average, the ratio with respect to free-space is $\mathcal{O}(1)$.

In principle, a detailed understanding of the track slope, and therefore the instantaneous cyclotron frequency $f_c(t)$, could be used to infer the underlying parameters of the radiating beta (e.g. pitch angle, radius), allowing better experimental energy resolution.

²<https://github.com/Helium6CRES/c-urchin>

*Johannes Gutenberg University Mainz.

†Department of Physics, North Carolina State University, Raleigh, NC.

‡Texas A&M, College Station, TX.

**Argonne National Laboratory, Lemont, IL.

‡Pacific Northwest National Laboratory, WA.

††Department of Physics, Tulane University, New Orleans, LA.

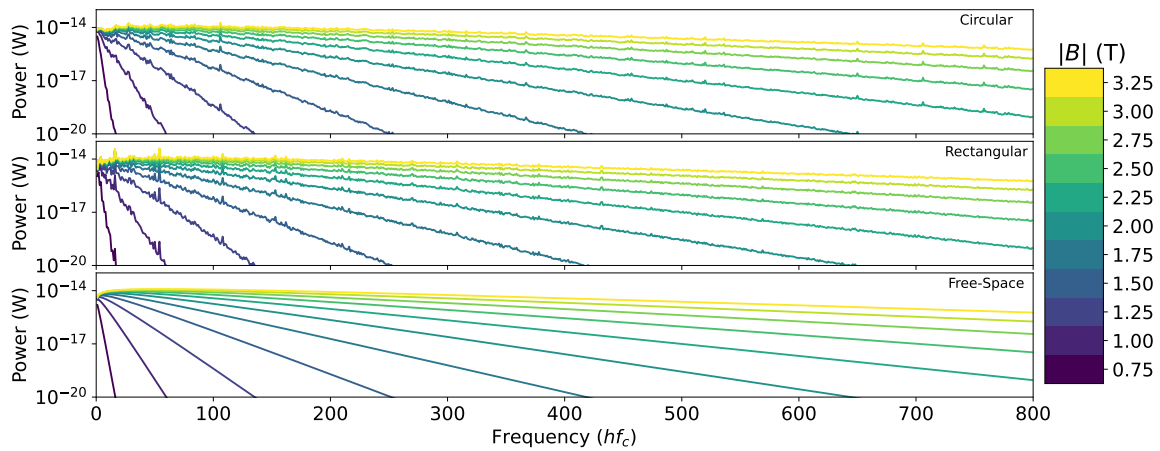


Figure 3.3-1. Frequency spectrum at harmonic frequencies hf_c , as a function of magnetic field, for the circular waveguide (top), rectangular waveguide (center), and free-space (bottom), given $f_c = 18$ GHz.

Currently, agreement between observation and predictions is approximately percent-level, at a given field. Importantly, non-linearities in the instantaneous track slope (shown in Fig. 3.2-4) do not agree with the model assuming naive radiation of a beta into a waveguide. Further development, refining the radiated power calculation model, is required for better agreement between prediction and observation.

For instance, energy conservation implies that cavity resonances in the He6-CRES apparatus, which can positively or negatively construct the emitted cyclotron radiation, must produce a corresponding change to the beta's energy. Numerical evaluation therefore requires a careful characterization of the reflections within the apparatus

3.4 He6-CRES Phase II RF system

W. A. Byron, N. Buzinsky, W. Degraw, B. Dodson, M. Fertl*, D. Fredin, A. García, H. Harrington, L. Hayen†, B. Maxwell, D. McClain‡, D. Melconian‡, P. Mueller**, N. S. Oblath‡, T. Rylander, G. Savard**, E. B. Smith, D. Stancil†, D. W. Storm H. E. Swanson, R. J. Taylor†, J. Tedeschi‡, M. W. Thomas, B. A. VanDevender‡, F. Wietfeldt††, A. R. Young†, and X. Zhu

In the first phase of data from He6-CRES, the RF noise and signal-to-noise ratio (SNR) contained a large frequency dependent oscillation. A frequency dependence in the SNR complicates our analysis since it is dependent on making SNR cuts to find CRES events. A

*Johannes Gutenberg University Mainz.

†Department of Physics, North Carolina State University, Raleigh, NC.

‡Texas A&M, College Station, TX.

**Argonne National Laboratory, Lemont, IL.

‡Pacific Northwest National Laboratory, WA.

††Department of Physics, Tulane University, New Orleans, LA.

sinusoidal SNR adds the additional problem of causing events to move into and out of our SNR detection band, which breaks up events into multiple tracks. This year, we have been working to reduce the frequency dependence of the SNR as much as possible.

We first addressed the sinusoidal RF noise. The He6-CRES experiment has a decay cell with RF components on either side (I-side and U-Side) that guide emitted light to low noise amplifiers. The noise measured out from either path had a prominent oscillation of 98.9(4) and 61(1) MHz for the I-side and U-side, respectively. We determined that this could best be modeled by the existence of a Fabry-Perot interferometer in the RF system. That is, two partially reflective mirrors where light starts outside the mirrors, circulates between the mirrors, and is then measured outside of the mirrors. Fitting this model to the noise determined that one mirror was a point near the circulator and the other was the farther of the two polarizers. The results of the fits are shown in Fig. 3.4-1.

Our understanding is that unpolarized noise is created in the rectangular guides. This noise travels through the first polarizer, becoming circularly polarized. This polarized light then completely reflects off the second polarizer, since it is the wrong polarization. Therefore, we designed a change to the RF system where the I-side and its polarizer are completely replaced with a circular termination. This way any signal traveling towards the I-side would reflect much less (-20dB).

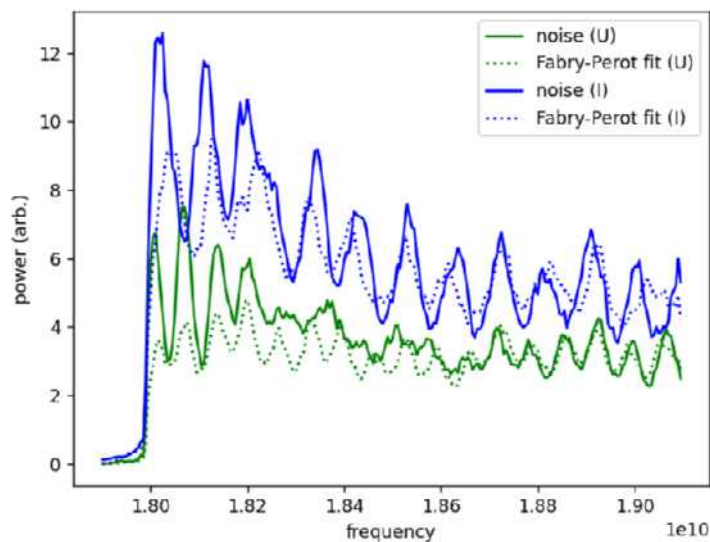


Figure 3.4-1. Noise from I and U Sides shown in solid green and blue lines. Fabry-Perot cavity fit to each noise shown with dotted line.

We designed and installed this new RF system, which we refer to as the Phase II system, this year. The new system includes 5 sections of copper circular waveguide, one stainless steel circular guide and a circular termination as show in Fig. 3.4-2. The portion of circular waveguides is needed because our cold head, which keep the termination at 14K, is located about a meter away from the decay cell. The stainless steel guide is used a thermal break so

that the decay cell remains at 60K. All components were built by the group (and associated machine shops). The termination was accomplished by creating a graphite-epoxy cone using a procedure developed by Project 8. This was measured with a vector network analyser to have a -20dB reflection.

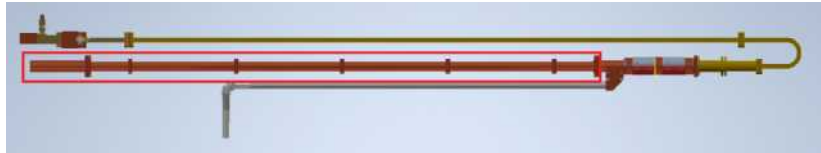


Figure 3.4-2. CAD diagram of RF system. Phase II upgrade components in red box are from left to right: circular terminator, stainless steel transition guide, 4 copper circular waveguides, copper transition guide.

The Phase II system significantly reduced the noise oscillation seen in the original system. Fig. 3.4-3 (left) shows the noise before and after the upgrade. There is still significant structure, but this could be due to the shape of the low noise amplifier gain. The SNR also changed significantly, but still continues to have a large oscillation, see Fig. 3.4-3 (right). The shape of this SNR is almost entirely due to reflections affecting the signal (no single frequency dominates the noise in the same way seen here). A Markov Chain model of the system with an arbitrary number of partially reflecting mirrors has been developed to evaluate the expected signals observed in the low-noise-amplifier. Using this, we have found two possible explanations for the shape of this noise. Either the termination is reflecting enough power to interfere with the signal, or we have another Fabry-Perot cavity between the decay cell and one of the photonic crystals. We plan to test these this summer and remove the offending reflection. Doing this should provide a reasonable flat SNR and help our event detection and analysis.

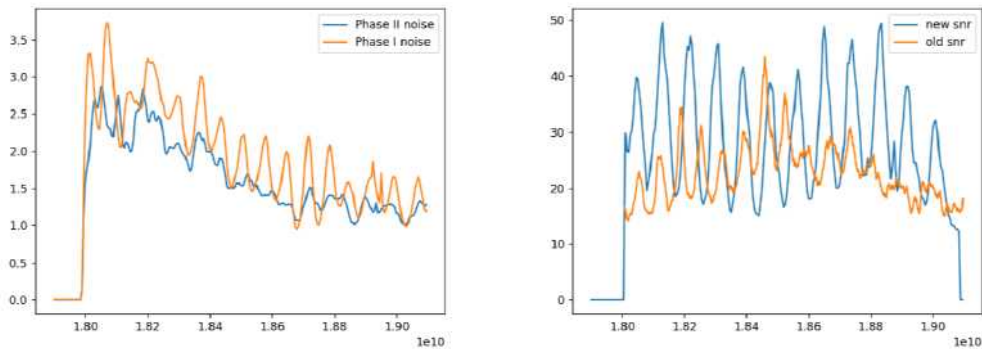


Figure 3.4-3. *Left:* RF noise power (arbitrary units) versus frequency for the U-side signal before and after Phase II RF upgrade. *Right:* Signal-to-noise ratio versus frequency compared for before and after Phase II RF upgrade.

3.5 ^{19}Ne source

W. A. Byron, D. Fredin, A. García, H. Harrington, D. W. Storm, M. W. Thomas, and X. Zhu

As described in the previous Annual Report,¹ we built a gas handling system and target in order to use the $^{19}\text{F}(p, n)^{19}\text{Ne}$ reaction with a beam from the Tandem accelerator at around 12 MeV. The source design is similar to the ^{19}Ne source developed at Berkeley^{2,3} and used later at Princeton,⁴ but without the difficulties related to getting polarized atoms. The gas flows continuously through the target, and the activated gas passes through a cold trap to freeze out the SF_6 , leaving the ^{19}Ne free to be compressed by a turbo pump.

Since the publication of the 2021 Annual Report¹ we used the system a number of times to provide ^{19}Ne for CRES studies.

Previously, we reported¹ that our production rate was lower than expected from calculations using the cross-sections measured by Jenkin,⁵ which suggested that we should produce $7.8 \times 10^8 \text{ s}^{-1} \mu\text{A}^{-1}$ atoms of ^{19}Ne in the target. However, in those measurements, we did not account for the relatively poor efficiency of the monitor detector telescope. GEANT-4 calculations of the efficiency for detecting a decay from our monitor chamber indicate that our production rate is consistent with the expected $10^9 \text{ s}^{-1} \mu\text{A}^{-1}$ in the target, combined with a loss of about a factor of 2 in the transit from the target to the experimental area. To date, we have run with beams over $3 \mu\text{A}$, which provide more than enough activity.

In the fall and winter of 2022-23, we revised the gas handling system by adding a second cold trap. We added a separate return line from the traps and put three-way valves on the gas cylinders, so we can recover gas from a warming trap into one cylinder while supplying gas to the system from another cylinder and freezing it into the other trap. Thus, we can run the system nearly continuously, with only a short pause to cool the second trap and reset the valves. Previously, it took 1/2 to 1 hour to recover the gas and re-cool the single trap. The modification also involved rebuilding the manifold (indicated on Fig. 3.5-1), also using three-way valves so we can select one of the traps for collection of gas from the target and the other one for return to the cylinder.

After the modifications to the gas handling system, there was an excess of N_2 in the CRES vacuum system when flowing SF_6 . Accumulating N_2 was the dominant contaminant in the CRES apparatus and limited the time data could be collected before the system had to be pumped out. RGA analysis showed partial pressures of $2 - 4 \times 10^{-6}$ Torr of N_2 above the cold trap during operation. Careful He leak checking found some leaks in the system following the target. After fixing these leaks, we did several cycles of flowing and freezing most of the

¹CENPA Annual Report, University of Washington (2021) p. 84.

²D. Dobson, *The beta-decay asymmetry and nuclear magnetic moment of Neon-19*, Ph.D. Thesis, U. C. Berkeley (1963).

³D. C. Girvin, *Test of time-reversal invariance in ^{19}Ne beta decay*, Ph.D. Thesis, U. C. Berkeley (1972).

⁴M. B. Schneider, F. P. Calaprice, A. L. Hallin, D. W. MacArthur, and D. F. Schreiber, *Phys. Rev. Lett.* **51**, 1239 (1983).

⁵J. D. Jenkin, L. G. Earwaker, and E. W. Titterton, *Nucl. Phys.* **44**, 453 (1963).

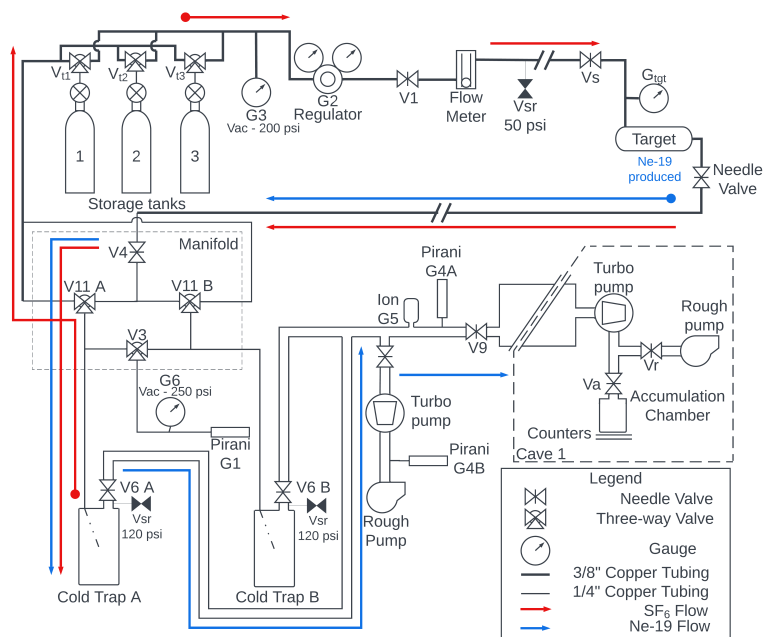


Figure 3.5-1. The gas handling system as described in the text. The target and SF₆ handling system is in Cave 2, near the ⁶He production system. Both systems connect to a 6-inch pipe running through the wall into Cave 1, where the activities are fed into the ⁶He-CRES device. The heavy lines indicate either 3/8" or 1/4" copper refrigeration tubing for gas transport.

gas in each cylinder while pumping on the trap. This process reduced the N₂ impurity by a factor of at least 4, which was enough that the getter pump in Cave 1 could reduce the N₂ in the CRES apparatus to the point where it was no longer a problem. With that improvement, N₂ accumulation no longer limits the time for taking CRES data. The ion gauge above the trap now typically reads around 1×10^{-5} Torr or better, which is presumably the result of residual SF₆ vapor. Extrapolation of published values¹ of the vapor pressure of SF₆ at low temperature suggests we should expect a partial pressure of SF₆ in the low 10⁻⁵ Torr range at 80 K. As the ion gauge is calibrated for air, its reading should be divided by 2.5 to get the actual pressure², if SF₆ is the dominant gas.

Besides producing ¹⁹Ne, the proton beam produces 32-minute ^{34m}Cl via ³⁴S(*p, n*) among other impurities. Most of these are short-lived, but the ^{34m}Cl accumulates in the cold trap. To avoid exposure to this activity while servicing the cold traps, we built an automatic fill system for the liquid nitrogen and have completed a system for positioning the liquid nitrogen container around the trap (for cooling) or below it (for warming) using rigging that can be operated from a distance.

¹<https://encyclopedia.airliquide.com/sulfur-hexafluoride>.

²<https://www.mks.com/n/gas-correction-factors-for-ionization-vacuum-gauges>.

4 Precision Muon Physics

4.1 Overview

The Precision Muon Physics Group’s scientific program is based on experiments that determine fundamental Standard-Model parameters, low-energy effective-field-theory constants, or provide sensitive tests for new physics. We are involved presently in three efforts that are all at different life-cycle stages. We present overviews and individual articles that represent just some of the technical work we have been doing on the MuSun, Muon $g - 2$, and PIONEER experiments. It is but a small sample of the actual work accomplished of course, but should provide a flavor for the variety of UW work in the past year.

4.2 The Muon $g - 2$ Experiment

H. Binney, S. Braun, C. Claessens, D. W. Hertzog, P. Kammel, J. LaBounty,
B. MacCoy, P. Schwendimann, and H. E. Swanson

Physics and motivation

The muon’s anomalous magnetic moment, $a_\mu \equiv (g - 2)/2$ is a special quantity because it can be both measured and predicted to sub-ppm precision, enabling a test for new physics defined by $a_\mu^{\text{New}} \equiv a_\mu^{\text{Exp}} - a_\mu^{\text{SM}}$. As a flavor- and CP-conserving, chirality-flipping, and loop-induced quantity, a_μ is especially sensitive to new physics contributions. In April 2021, our Muon $g - 2$ Collaboration published¹ the result from our Run-1 data taking campaign (> 1600 citations). The result is in excellent agreement with the final BNL E821 measurement² and the new world average,

$$a_\mu(\text{Exp}) = 116\,592\,061(41) \times 10^{-11} \quad (0.35 \text{ ppm})$$

when compared to the 2020 *Muon $g - 2$ Theory Initiative* recommended Standard Model (SM) value³, gives

$$a_\mu(\text{Exp}) - a_\mu(\text{SM}) = (251 \pm 59) \times 10^{-11} \quad (4.2 \sigma).$$

Since that time, we have been working to complete the analysis of the Run-2 and Run-3 data, which has just been unblinded and announced in August, 2023⁴. The Run-2/3 data sets represent 4.7 times that previously published and, with improvements in the hardware

¹Phys.Rev.Lett. 126 (2021) 14, 141801, Phys.Rev.A 103 (2021) 4, 042208, Phys.Rev.D 103 (2021) 7, 072002, and Phys.Rev.Accel.Beams 24 (2021) 4, 044002.

²Phys.Rev.D 73 (2006), 072003.

³Phys.Rept. 887 (2020), 1-166.

⁴Muon $g-2$ Collaboration, arXiv:2308.06230v1, 11 Aug 2023, Submitted to PRL.

systems compared to Run-1, systematic uncertainties have been reduced by a factor of 2.2 to a total of 70 ppb, exceeding our proposal goal. At UW, our group made major contributions to the muon precession analysis (Theses: J. Hempstead and H. Binney; final analysis work by J. Labounty and S. Braun). We provided the analysis of the muon-weighted magnetic field (Thesis: B. MacCoy, with P. Kammel) and we have been involved in several beam dynamics systematics efforts (muon loss: H. Binney and J. Labounty; beam storage and E-field correction studies: C. Claessens, B. MacCoy, and P. Kammel). The Run-2/3 results represent years of work by many groups in our collaboration and all efforts are well documented, then scrutinized through multiple internal review stages. Only when the entire blinded analyses were complete did we vote to reveal the result, an event that took place at our summer off-site collaboration meeting in Liverpool in late July.

The Run2/3 value for the muon anomalous magnetic moment rather exactly re-confirmed our previous measurement; combined, our FNAL 1/2/3 measurement is

$$a_\mu(\text{FNAL}) = 116\,592\,055(24) \times 10^{-11} \quad (0.20 \text{ ppm})$$

and when combined with that from BNL E821, gives the very slightly improved new world average (WA) experimental result of

$$a_\mu(\text{WA}) = 116\,592\,059(22) \times 10^{-11} \quad (0.19 \text{ ppm})$$

. If we dared to compare it to the 2020 *Muon $g-2$ Theory Initiative* SM value, we would find the new world average to lie 5.1σ higher, a tantalizing prospect. However, critical inputs to the lowest-order hadronic vacuum polarization (HVP) contribution have muddled the landscape of obtaining a firm prediction. In 2021, the BMW Collaboration published a precise lattice QCD calculation¹ of the HVP contribution that is competitive with the data-driven dispersion approach that has been a standard in the field. Follow-up work by several independent lattice groups have yet to confirm or refute this effort, but progress has been significant in certain aspects of testing representative calculations and experts are confident that in due time the lattice QCD approach will settle and likely provide a very precise prediction. As suggested above, the HVP term is obtained from measurements of absolute cross-sections for e^+e^- annihilation to hadronic final states. At least six independent experimental results are typically averaged prior to evaluating the HVP term; differences in comparative cross-sections between collaborations are carefully incorporated into an expanded uncertainty. The 2020 SM value is based on this approach, and the 345 ppb uncertainty is almost entirely driven by these data sets. In early 2023, the CMD-3 Collaboration at Novosibirsk, released a surprising new result² for the $\pi\pi$ channel that is central to the HVP calculation. Their result differs by 4-5 standard deviation from all others (including their previous measurement) and, like the BMW lattice calculation, falls much higher than the 2020 value, leading to – if true – a much smaller deviation between the experiment and theory. Accordingly, at the time of this Annual Report, we cannot say much about “discovery” or “confirmation” of the SM, but work is in progress in the theory sector and, from our Collaboration’s side, we have much more data from Runs 4, 5, and 6, all now being vigorously processed.

¹Nature 593 (2021) 785.

²CMD-3 Collaboration, e-Print: 2302.08834 [hep-ex].

The results are shown graphically in Fig. 4.2-1. The BNL, Run-1, and Run-2/3 results are shown along with the new world average (WA). The experimental campaign has clearly been very consistent.

In other important news, Fig. 4.2-1 illustrates the final accumulated data size we collected through Run-6, along with the projected final uncertainty. Run-6 ended in early July 2023. Throughout these many years, our UW team supported the many hardware systems we designed and built, including the entrance detectors (T0, IBMS), the calorimeter system, the NMR hardware and electronics, and recently, a novel in-vacuum imaging detector discussed in a companion article.

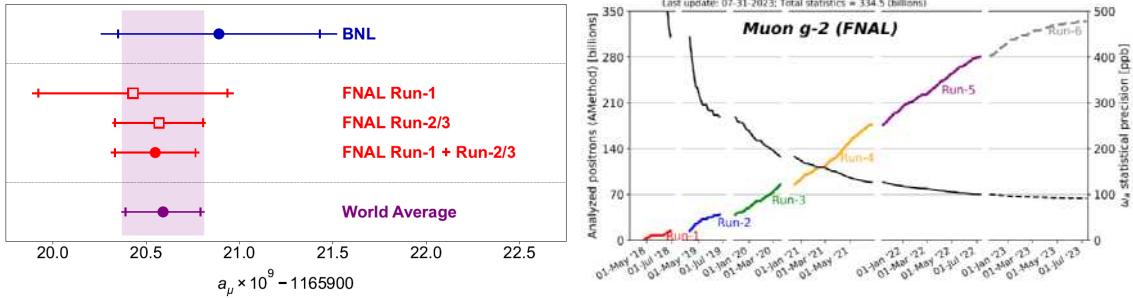


Figure 4.2-1. Left: The BNL, Run-1, and Run-2/3 results together with the new world average (WA). (Figure: Muon g-2 PRL 2023). Right: The figure illustrates the accumulated data obtained for Runs 1-6 and the projected statistical uncertainty on the precession frequency at each stage.

Experimental concept and status

When a muon with charge q is circulating in the horizontal plane of a magnetic storage ring, its cyclotron frequency is $\vec{\omega}_c = -q\vec{B}/m\gamma$. The muon spin precesses at frequency $\vec{\omega}_s = -(gq\vec{B}/2m) - [(1 - \gamma)q\vec{B}/\gamma m]$. Assuming a negligible muon electric dipole moment, the anomalous precession frequency can be expressed simply

$$\vec{\omega}_a \equiv \vec{\omega}_s - \vec{\omega}_c = -\left(\frac{g-2}{2}\right) \frac{q\vec{B}}{m} = -a_\mu \frac{q\vec{B}}{m}. \quad (1)$$

Parity violation associates the decay positron energies in the laboratory frame with the average spin direction of the muon at the time of the decay, such that the highest-energy positrons are preferentially emitted when the muon spin is aligned with its momentum, and lower-energy positrons are emitted when the spin is reversed. The UW system of electromagnetic calorimeters is used to measure the decay positron times and energies, and from these data determine the anomalous spin precession frequency ω_a .

The magnetic field B is measured in terms of the proton's Larmor precession frequency ω_p . The pNMR system developed at UW is critical to this effort. It is further necessary

to know the muon distribution in the storage ring for the muon population that contributes to the ω_a data. This distribution is folded with similarly determined azimuthally averaged magnetic field moments to give the effective magnetic field seen by the muons, $\tilde{\omega}_p$ below. One obtains a_μ through the relation

$$a_\mu^{\text{Exp}} = R \frac{g_e m_\mu \mu_p}{2 m_e \mu_e}, \quad \text{where } R \equiv \omega_a / \tilde{\omega}_p \quad (2)$$

is measured by our collaboration. The electron g_e factor, the muon-to-electron mass ratio, and the proton-to-electron magnetic moment ratio are known to sufficient precision.

Briefly, the experimental data taking proceeds as follows. Compact bunches of 3.1 GeV/ c polarized muons are delivered into our 1.45 T superconducting storage ring at a fill rate of ~ 11 Hz. Their intensity, timing, and spatial profiles are measured with UW built T0 and IBMS counter systems. Once inside the ring, muons are deflected on their first turn onto stable orbits within a defined storage volume by a magnetic outward, pulsed kick. A system of electrostatic quadrupole plates that are charged prior to injection vertically contains the particles. The positrons from muon decay curl inward, where their hit times and energies are recorded in one of the 24 UW-built electromagnetic calorimeter stations. Two calorimeter stations include in-vacuum tracking chambers just upstream of the detectors in order to provide an indirect tomography of the stored muon distribution from tracing the positron trajectories into the storage volume. The magnetic field is monitored continuously by 378 fixed NMR probes built at UW and placed above and below the vacuum chamber. The azimuthally dependent multipolarity of the field is mapped in detail in the storage volume every ~ 3 days using a 17-probe NMR trolley. Representative figures for a subset of the UW-built hardware are shown in Fig. 4.2-2.

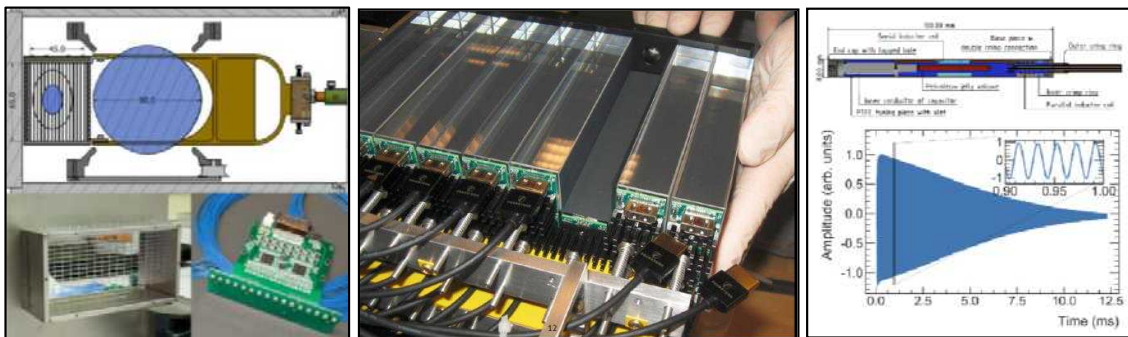


Figure 4.2-2. Representative UW-built hardware images. *Left-top*: IBMS-3 design; *bottom*: IBMS-1 detector and electronics. Three IBMS detectors measure the incoming beam intensity, trajectory, and spatial profile. Inner error bars are statistical; outer are total. *Middle*: Photo of an opened calorimeter showing crystals and SiPM readout. 24 such stations measure the decay positron times and energies. *Right-top*: An NMR probe used in the fixed and trolley systems; *bottom*: a typical free induction decay signal. 378 probes form the fixed-probe system and 17 are embedded in the in-vacuum trolley.

4.3 Measurements of the Incoming Phase Distribution in Run-6

J. LaBounty

The muons in the $g - 2$ storage ring begin their lives as 8 GeV protons in the recycler ring of the former Tevatron. These long proton bunches are re-shaped using RF cavities into 8 muon bunches, each with its own unique shape and temporal distribution. These are then extracted to the AP0 target hall at a rate of ≈ 11 Hz. Once in the hall, the protons impact an Iconel production target, producing a cloud of secondary particles. Particles with a forward momentum of ≈ 3.1 GeV are selected and transported along the M2 beamline towards the $g - 2$ storage ring. The muons which are injected into the $g - 2$ storage ring are produced primarily from π^+ decays in the M2/M3 beamlines (see Figure Fig. 4.3-1). Selection in these beamlines of only forward going muons yields a high intensity muon beam with $\approx 95\%$ polarization entering the delivery ring (DR). After 4 turns around the DR, the muon and proton bunches no longer overlap and the protons are removed from the beamline using an electromagnetic abort kicker. The muons are then extracted along the M4/M5 beamline to the $g - 2$ storage ring. This detour along the DR, while necessary to remove the ‘proton flash’ which limited the previous generation $g - 2$ experiment, introduces an initial phase-momentum correlation due to differences in the path length of high and low momentum muons through the beamline.

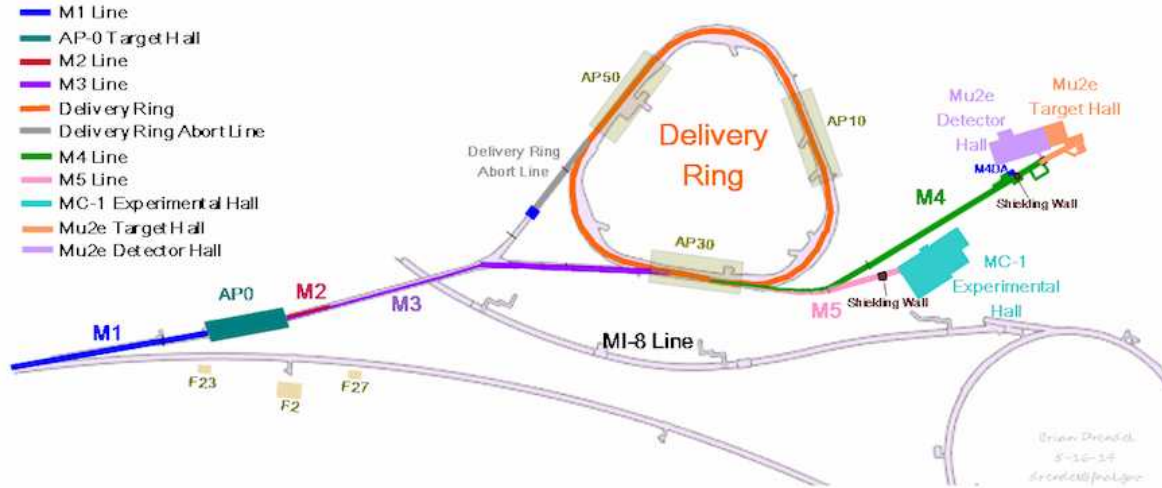


Figure 4.3-1. Diagram of the upstream beamlines.

Such an initial phase-momentum correlation can be detrimental to the extraction of the anomalous precession frequency — ω_a — if the stored momentum distribution changes vs. time:

$$\frac{d\langle p \rangle}{dt} \frac{d\langle \phi_a \rangle}{d\langle p \rangle} = \frac{d\langle \phi_a \rangle}{dt} = \Delta\omega_a. \quad (1)$$

We know that the stored momentum distribution in the ring changes due to two effects:

- Momentum dependent muon losses: Lower momentum muons have a higher probability of hitting the aperture defining collimators and being ejected from the storage region before they can decay.
- Differential decay: Higher momentum muons ($\gamma > \gamma_{\text{magic}} \approx 29.3$) have a slightly longer lifetime than low momentum muons, and so will make up a higher proportion of the stored population at later times.

Both of these effects are small ($< 20\text{ppb}$), but in order to properly quantify them, we must also quantify the initial $\phi - p$ relationship. End-to-end simulations of the beamline predict a phase-momentum relationship of

$$\frac{d\langle\phi_a\rangle}{d\langle p\rangle} = -9.54 \frac{\text{mrad}}{\% \delta p/p}.$$

This relation is shown in Figure Fig. 4.3-2 (red curve).

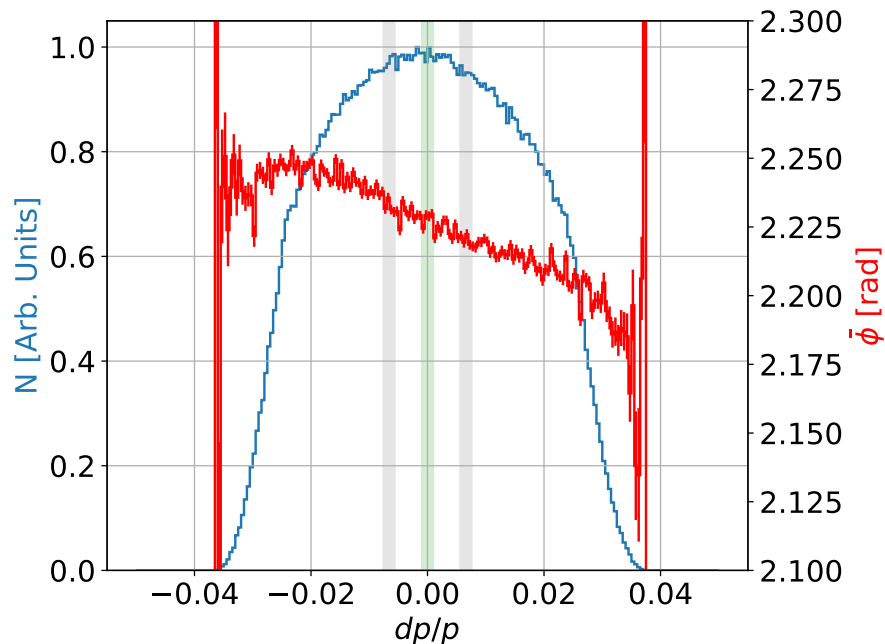


Figure 4.3-2. Simulated intensity (blue) and phase (red) distributions vs. momentum at the end of the M5 beamline, just before injection to the $g - 2$ storage ring. The green band represents the region of this distribution which is selected in nominal operation, while the grey bands are the high and low momentum regions selected for this study.

The $g - 2$ storage ring has a momentum acceptance of $\delta p/p = \pm 0.1\%$, but the overall momentum distribution of the incoming beam is $\delta p/p \approx 5\%$ (see Figure Fig. 4.3-2). This wide incoming momentum distribution means that we can map out the incoming phase-momentum distribution in data simply by selecting a different slice of the incoming beam. We do this by changing the magnetic field of the storage ring, and therefore also p_0 , by $\pm 0.66\%$. We

then perform an ω_a analysis on these high, low, and nominal momentum datasets and fit the resulting ϕ values vs. the momentum change.

From this analysis, we extract the result:

$$\frac{d\langle\phi_a\rangle}{d\langle p\rangle} = -13.51 \pm 1.42 \frac{\text{mrad}}{\% \delta p/p}. \quad (2)$$

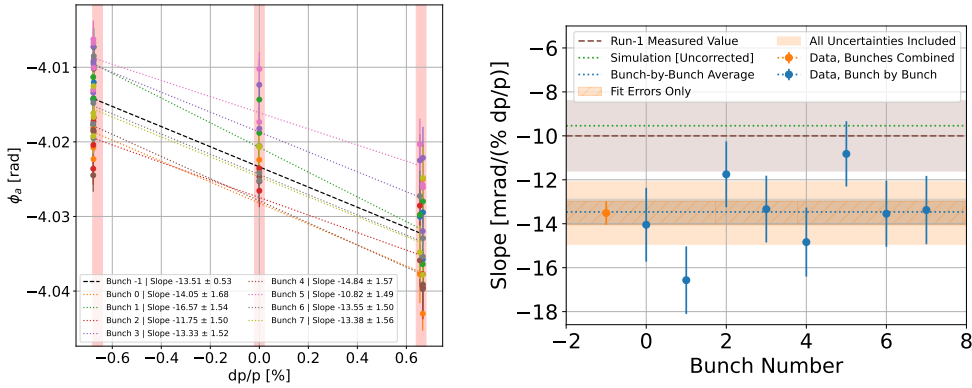


Figure 4.3-3. *Left:* Bunch by bunch fits to the incoming phase-momentum relationship. Since each bunch has a unique temporal profile, the bunches are shifted vertically relative to one another. The extracted slopes, however, are consistent. *Right:* Results of the extracted slopes bunch by bunch compared with simulation. The simulation and the Run-1 result disagree with the updated measurement.

The Run-6 measurement is 35 – 40% larger compared to the Run-1 measurement and the beamline simulation. After repetition of the measurement, which confirmed the result, a thorough look at the simulation was undertaken, to determine whether there had been changes to the experimental setup since Run-1 which were not included in the latest model. Through this search, we were able to determine that a momentum cooling wedge in the M4/M5 beamline had been inserted in Run-2 but had not been included in the latest beamline simulation model. This wedge is inserted in an area of the beamline with high radial dispersion, and degrades high momentum muons to lower momentum. It is inserted in such a way that it is designed to minimally impact (if at all) muons with $p < p_{\text{magic}}$. Toy Monte Carlo simulations of including the wedge, combined with back to back measurements of the $g - 2$ phase with the wedge inserted vs. retracted, indicate that the wedge is responsible for the increase in slope (see Figure Fig. 4.3-4).

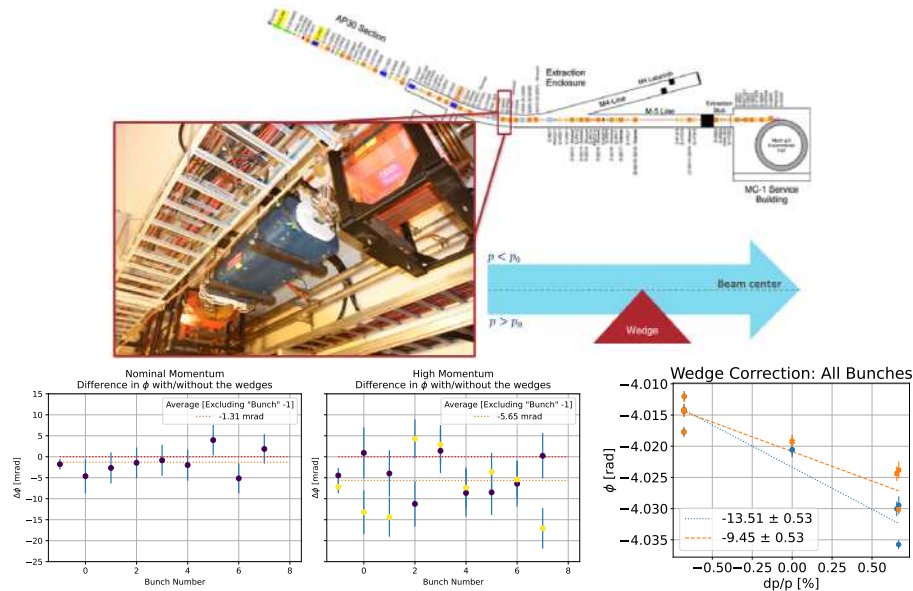


Figure 4.3-4. *Top:* Diagram showing the M4/M5 cooling wedge location in the beamline. *Bottom Left/Middle:* Measured effect of inserting the wedge on the $g - 2$ phase. *Bottom right:* Measured slope, with (orange) and without (blue) a correction for wedge effects at high and nominal momenta.

4.4 Beam dynamics studies with the MiniSciFi detector

S. Braun, T. Burritt, C. Claessens, P. Kammel, B. MacCoy, N. Miedema, D. Peterson, R. Roehnelt, and T. Van Wechel

Introduction

After reaching the statistics goal of 21 BNLs in Run-6, the focus of the collaboration shifted toward systematic studies. Especially the electric field correction to ω_a , calculated from the reconstructed muon momenta, remains a hot topic since it is the largest source of systematic uncertainty on ω_a . The time-varying strength of the kicker magnet, which shifts the muon beam to its nominal orbit, leads to an injection time dependence of the stored beam momentum which distorts the momentum reconstruction. Significant effort was required in Runs 1-3 to estimate the uncertainty due to this time-momentum (t - p) correlation, which was extracted via fits from calorimeter data in the absence of a direct measurement of the effect.

To enable a data driven measurement of the t - p correlation, and for other validations of detector and simulation properties in the experiment, the CENPA muon group developed the Minimally Intrusive Scintillating Fiber detector (MiniSciFi). With the goal to directly measure the stored beam with minimal disturbance, we designed a detector with 3 scintillating fibers using the 250um SCSF-NOL11 fibers from Kuraray. Geant4 simulations of the storage

ring and the detector showed that the presence of 3 fibers separated by 26 mm causes an inward drift of less than $0.5 \text{ mm}/\mu\text{s}$ and a lifetime reduction of the muon beam of less than 1.5%.

Detector details

We made 2 frame designs, one for holding vertical and one for horizontal fibers (Fig. 4.4-1). The fibers are glued into small holes in the frames with optical cement. The purpose of the vertical-fiber version of the detector is to measure the beam intensity at the fiber's horizontal positions. By stepping the detector through the beam, a detailed horizontal beam profile can be reconstructed. With the horizontal fibers, on the other hand, we can measure the momentum distribution of all muons in the beam. While the horizontal fibers cannot be scanned vertically through the beam (the positioning arm only moves the detector horizontally), the betatron oscillation makes all muons pass the vertical center. By doing a frequency analysis of the intensity vs. time on the central horizontal fiber, the distribution of beam cyclotron frequencies and hence the equilibrium radii and momenta can be extracted.

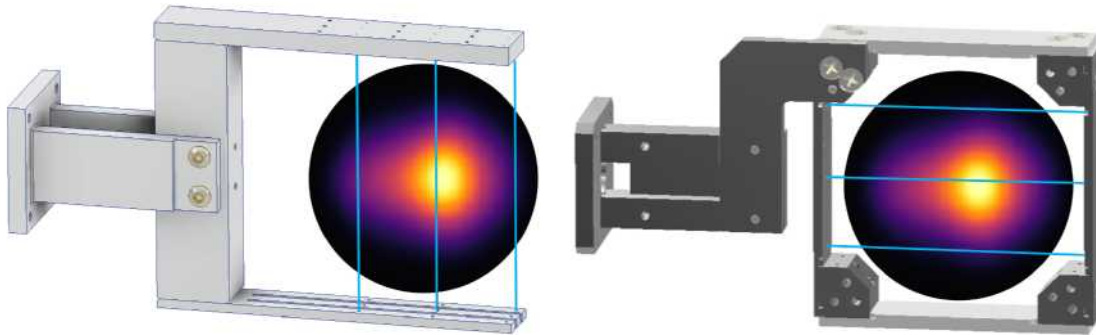


Figure 4.4-1. Vertical (left) and horizontal (right) MiniSciFi detector designs, overlaid with the transverse stored muon beam profile reconstructed by separate indirect tracking detectors.

To read out the fiber signals, we initially used an amplifier board from the CENPA-built injection beam monitoring system (IBMS), but later replaced it with a custom DC-coupled board that had a shorter impulse response ($\approx 15 \text{ ns}$). DC coupling is required because of the slow intensity decrease of the muon beam that is otherwise convolved with the AC response. As a result, with the old amplifier board the beam signal amplitude is not proportional to the beam intensity, which is problematic for constructing the beam profile vs. storage time (Fig. 4.4-2).

For mounting and positioning the MiniSciFi one of the 4 fiber harp detectors that were previously installed in the g-2 experiment was decommissioned and shipped to CENPA. We disassembled the fiber harp frame to be able to use the detector arm for the MiniSciFi. We also modified the motion control mechanism to enable precise position scans. Ryan Roehnelt designed a new motion mechanism for the detector arm, in which a lead screw is turned

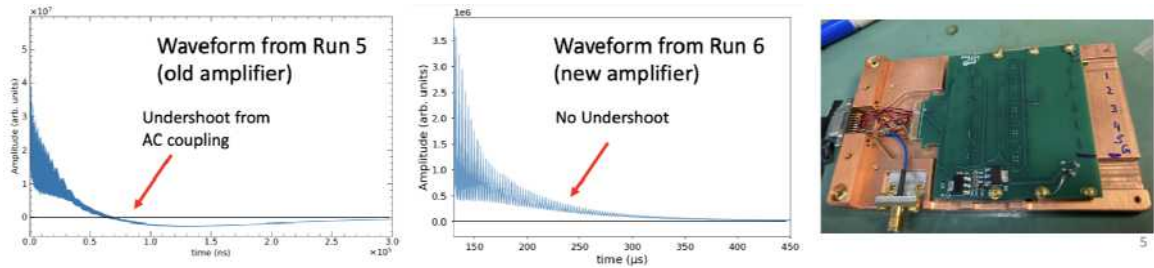


Figure 4.4-2. Averaged signal recorded with the central fiber of the horizontal MiniSciFi in run 5 (left) and the vertical MiniSciFi in run 6 (center). The signal is averaged over many beam injections. The AC coupled amplifier in run 5 lead to an undershoot in the recorded waveforms. The new amplifier board (right) in run 6 resolved this issue which simplifies the profile and time-momentum analysis.

by a nonmagnetic piezo motor to guide the motion. A test measurement of the position repeatability of the system showed that the differences between set and measured positions can be kept below $\pm 50 \mu\text{m}$ (Fig. 4.4-3).

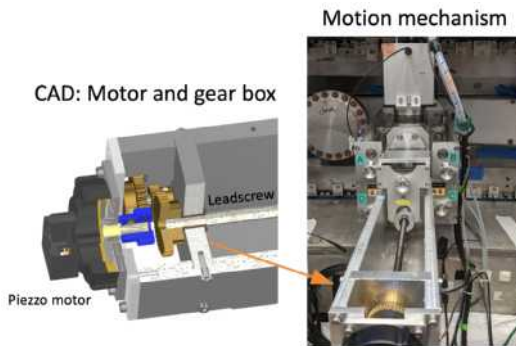


Figure 4.4-3. The MiniSciFi motion mechanism consists of a lead screw that is turned by a piezo motor. Translation gears reduce the torque required to turn the screw.

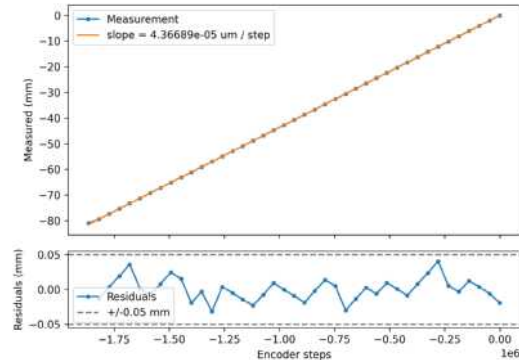


Figure 4.4-4. The MiniSciFi motion mechanism consists of a lead screw that is turned by a piezo motor. Translation gears reduce the torque required to turn the screw.

Measurement campaign

The horizontal MiniSciFi was installed in the storage ring during Run-5. The first systematics data were taken in July 2022, with the goal of measuring the t - p correlation in narrow time slices. Because the kicker pulse is not much longer than the injected muon bunch, we used an upstream proton abort kicker to shorten the muon bunches at the expense of the number of muons in each bunch. By scanning the kicker delay in steps over a range of ± 100 ns,

we could measure the momentum distribution as a function of injection time relative to the kicker. The measured correlation can be used to analytically correct the reconstructed momentum distribution and reduce the corresponding uncertainty.

During the summer shutdown, the MiniSciFi was uninstalled from the ring again and shipped back to CENPA for upgrades and repair. The plastic coupling nut of the lead screw was damaged as a result of the high torques in the motion system resulting from the pull of the vacuum. We replaced it with a brass nut and also replaced the titanium lead screw with a stainless steel version. To reduce the torque, we added a pressured-air piston to the setup that would pull on the lead screw to counteract the vacuum force. In parallel, CENPA engineers designed and build the fast, DC coupled amplifier board and grounding box.

During Run-6 in January 2023, we brought the MiniSciFi back to Fermilab and installed the vertical-fiber version in the ring. A series of horizontal beam profiles was recorded under nominal and special beam conditions, to better understand the response of the beam to various inflector, kicker, and quadrupole settings. In April, we swapped the vertical-fiber for the horizontal-fiber MiniSciFi to repeat and extend the t - p studies from Run-5, this time with the new fast amplifier electronics. In April, the vertical-fiber MiniSciFi was reinstalled at a different location in the ring.

The last MiniSciFi data was taken shortly before the end of Run-6 in July 2023, concluding a long and successful systematic study program, and analysis of the data is underway. Fig. 4.4-5 shows a preliminary horizontal beam profile measured with the vertical MiniSciFi, and Fig. 4.4-6 shows a t - p distribution measured with the horizontal MiniSciFi which still requires an additional step to unfold the injected bunch shape and recover the correlation. These analyses will support calculations of the ω_a beam dynamics corrections in Runs 4-6 and further improve the calibration of the indirect muon beam tracking detectors.

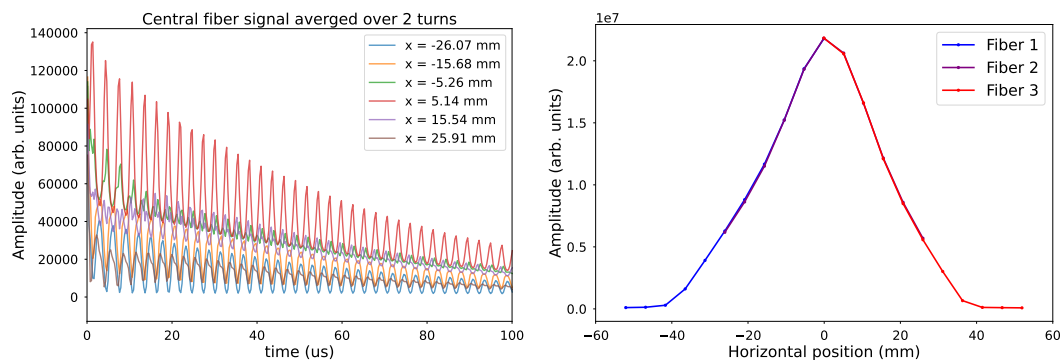


Figure 4.4-5. *Left*: Beam signal recorded with the central fiber at different locations. By integrating the signal from all fibers at each scan position a full horizontal profile can be reconstructed. *Right*: Horizontal beam profile measured with the vertical MiniSciFi in Run-6. The ranges scanned by each fiber overlaps with the range scanned by the neighboring fiber. This way the relative fiber efficiencies are calibrated.

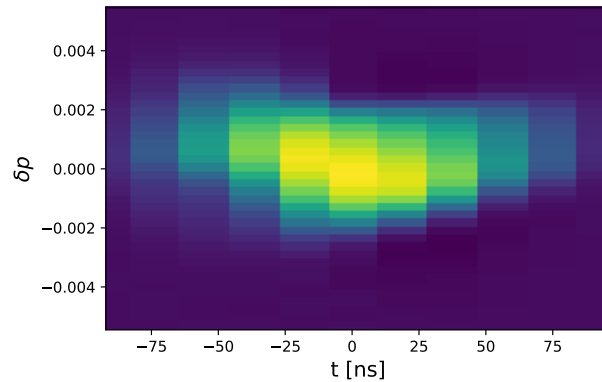


Figure 4.4-6. Momentum distribution vs. injection time measured with the horizontal MiniSciFi in Run-6, with momentum in terms of the relative offset δp from nominal. The t - p correlation can be recovered from this measured distribution.

4.5 Anomalous spin precession frequency comparisons

S. Braun and J. LaBounty

Introduction

As explained above in 4.2 the anomalous spin precession ω_a is extracted in the decay positrons extracted from the calorimeters. Due to parity violation ω_a is encoded in the number of decay positions above a certain energy threshold. ω_a is extracted from a fit to a time-binned histogram, which contain clusters that are reconstructed from crystal hits based on the time and energy of the reconstructed decay positrons.

Comparison of the different ω_a analyses

In total there are seven independent analysis groups that determine ω_a : Boston, Cornell, Europa, IRMA, Kentucky, Shanghai and Washington. Two different methods are used reconstructing individual positrons: Recon East and Recon West, and one method to reconstruct the integrated energy spectrum (Q-method). The Recon West analyses differ by their implemented clustering algorithm in combining crystal hits based on crystal energy thresholds and positron cluster timing. There are also different approaches constructing the time histograms of position hits above an energy threshold: In the T-method hits are equally weighted whereas for the A-method weights are based on their energy-dependent muon-decay asymmetry ($w(E) = A(E)$). In addition, the Ratio method involves dividing above-threshold, reconstructed positrons into four statistically equal datasets and is applied to both T- and A-method.

There are also differences in how different groups deal with pile-up, which occurs when multiple positrons are misidentified as one single positron. The probability for pile-up is higher

at the beginning of the fill when the muon intensity is higher, and therefore a rate-dependent effect. Also, pile-up events have a different phase and time dependence than real positions which can bias ω_a , if it is not corrected. The wiggle histogram is corrected by subtracting an empirically constructed pile-up spectrum. There are three different methods used to construct the spectrum which are all based on a shadow-window idea using a trigger and shadow positron combined into a pile-up event, but differ by combining clusters, crystal hits or raw traces from the calorimeter.

Every analysis group uses a different fit-function to fit the time-binned histogram to extract ω_a . All groups account for the features of the weak decay by a 5-parameter fit function such as $N(t) = N_0 e^{-t/\tau} [1 + A \cos(\omega_a(R)t - \phi)]$, where N_0 is the number of positrons at $t = 0$, τ is the time dilated muon lifetime, A the asymmetry, $\omega_a(R)$ the blinded frequency as the physics quantity and ϕ the spin phase at injection. There are remaining effects beyond the basic precession frequency oscillations causing modulations of the positron rate measured by the calorimeters, coming from beam dynamics effects that couple to the acceptance. The largest contribution comes from horizontal beam oscillations about the central orbit in the storage region, known as coherent betatron oscillation (CBO). This oscillation decoheres as a function time in fill, which can be parameterized by a decoherence envelope with an unknown exact functional form, such that different parametrizations were tried per analysis group to estimate a systematic uncertainty due to that. This is accounted for in the fit function with the most general form: $N_{CBO}(t) = 1 + e^{-t/\tau_{CBO}} A_{CBO} E_{CBO}(t) \cos(\omega_{CBO}(t)t - \phi_{CBO})$, where $E_{CBO}(t)$ stands for the envelope and $\omega_{CBO}(t)$ is the time dependent CBO frequency.

Vertical betatron and vertical width (VW) oscillations are taken into account with additional terms in the fit. Those couple through the detector acceptance to the horizontal CBO oscillations and create a VW-CBO beat frequency term. Additional parameters are added to the fit to account for that. The last remaining component for the fit function is to account for muons that are lost from the storage ring before they decay. This requires an empirically determined loss spectrum, which can be identified through their characteristic energy deposit as minimum ionizing particles in the calorimeter and their flight time from transversing multiple calorimeters.

The different contributions are parameterized differently in the 7 analysis groups, therefore the total number of free parameters in the fit varies with analysis choices and histogramming methods, with a minimum of 14 for Europa to a maximum of 38 parameters for Kentucky. All 7 analysis are relatively blinded with respect to each other therefore the blinded ω_a per group can't be compared with respect to each other group, this can only be done post relative unblinding. One of the consistency checks between analysis groups post unblinding was to swap the time-binned histograms as the input to the fit to identify the impact of different analysis choices between groups.

Boston-Washington histogram swap

Each analysis group uses independent code to make the time-binned histogram as well as to fit them. By swapping histograms between groups, we can cross-check a group's fitting code for bugs and also test for the effect of different fitting function choices to fit the data. We wanted to see if we get the same result fitting the same histogram or are there remaining

differences which are due to different analyses choices which we can remove by equalizing our analyses. For this exercise Recon East and Recon West analyzers swapped histograms and for us, we exchanged them with the group from Boston.

Both analyses use the same method to reconstruct pile-up, and the clustering algorithm. Differences are that in the Boston time-binned histograms all vertical frequency terms are randomized out, whereas we include those contributions and have fit additional parameters to account for those. Therefore, we both had to adjust our fitting code accordingly such that we remove these terms when fitting Boston's histograms, and they included extra terms when fitting our data. We found an up to 14ppb shift on R for Run2 and 3 datasets when swapping histograms and fitting them each with our nominal fit function adjusted for the vertical term difference.

In order to track down where this difference is coming from, we identified the following fitting differences:

- drifting CBO frequency term: using different lifetimes and amplitudes for $\omega_{CBO}(t) = \omega_{CBO} + ae^{-t/\tau_a}/t$ and fixing both terms (us, from tracker data) or letting the amplitude float (Boston)
- fixed muon loss normalization value in Run3: we fix it to zero, whereas Boston fixes it to a non-zero value which is scaled from Run 2
- CBO envelope choice: Boston used for their nominal fit $E_{CBO}(t) = e^{-t/\tau_{CBO}} + c$ for all 3 datasets, whereas we use the exponential only model for Run 2 and 3a, and the exponential+const for Run 3b
- Implementation difference of envelope: Boston only modifies the central CBO envelope whereas we modify also the higher order terms such as 2CBO and also modify the envelope for the phase and asymmetry modulation such that they are modified from the time-dependent CBO oscillation.

After equalizing our fit functions based on the above differences, the shift of R is within 1ppb. We found that the largest shift comes from the different drifting CBO frequency treatment (-12ppb). The CBO envelope choice adds a difference of -5ppb and the fixed muon loss normalization parameter is small (+3ppb).

Through these studies we found how important the inclusion of the drifting CBO frequency term for the analysis of the anomalous spin precession frequency ω_a is, non-inclusion of this term leads to a 30ppb shift in R. Also our fitting differences came from reasonable different analysis choices, which are covered by the systematic uncertainties assigned to ω_a .

4.6 Rare Pion Decays: PIONEER

O. Beesley, S. Braun, Q. Buat, D. W. Hertzog, P. Kammel, J. LaBounty, R. Roehnelt, P. Schwendimann, and H. E. Swanson

Lepton flavor universality (LFU) implies that the weak force is the same for e, μ and τ leptons. Our MuLan experiment ¹ measured the muon lifetime to a precision of 1 ppm, which determined the Fermi Constant G_F to 0.5 ppm, through the understanding that G_μ is identical to G_F because of LFU. It is fair to ask, how solid is this assumption? In 1999, Marciano raised the issue ² and more recently Crivellin and Hoferichter ³ explored how LFU violation might be the root cause of the $> 3\sigma$ tension in the Cabibbo-Kobayashi-Maskawa (CKM) quark-mixing matrix first-row unitarity relation. Some large LFU violation signals in B decay channels continue to exist, perhaps with a different underlying cause. Finally, the difference between the measured and calculated values for the muon anomalous magnetic moment is yet another hint at new physics that might be related to lepton flavor. Our group has been working with others on a next-generation rare pion decay experiment – PIONEER – that can contribute significantly to both LFU violation tests and CKM unitarity. PIONEER is now approved at PSI with high priority, and the collaboration has been vigorously developing simulations and hardware prototypes.

Phase I of PIONEER will be a measurement of the charged-pion branching ratio to electrons vs. muons, $R_{e/\mu}$, which is extremely sensitive to new physics at high mass scales. The proposed detector system – appropriately upgraded for rate – can also be used to measure pion beta decay, $\pi^+ \rightarrow \pi^0 + e^+ \nu_e(\gamma)$, and other rare decays. Order of magnitude improvements in sensitivity to these reactions will probe LFU at an unprecedented level, determine V_{ud} in a theoretically pristine manner, and test CKM unitarity at the quantum loop level.

Regardless of specific new-physics models, these experiments are well motivated. The $R_{e/\mu}$ ratio,

$$R_{e/\mu} = \frac{\Gamma(\pi^+ \rightarrow e^+ \nu(\gamma))}{\Gamma(\pi^+ \rightarrow \mu^+ \nu(\gamma))} \quad (1)$$

was calculated to extraordinary precision within the Standard Model by Cirigliano and Rosell ³, obtaining $R_{e/\mu}(\text{SM}) = (1.2352 \pm 0.0001) \times 10^{-4}$. The PDG experimental average $R_{e/\mu}(\text{Exp}) = (1.2327 \pm 0.0023) \times 10^{-4}$ is in fair agreement with the SM but more than 20 times less precise. The $R_{e/\mu}$ ratio can be interpreted as a test of e - μ universality; the current ratio leads to the relation $g_e/g_\mu = 0.9990 \pm 0.0009$. The large gap in precision between experiments and theory represents a discovery opportunity.

³Phys. Rev.Lett. 99, 231801.

¹Phys. Rev.Lett. 106, 041803, Phys. Rev.D 87, 052003, and previous Annual Reports.

²Phys. Rev.D 60, 093006.

³Phys. Rev. Lett. 127, 071801.

Basics for a new measurement of $R_{e/\mu}$

At rest, the pion lifetime is 26 ns and the muon lifetime is 2197 ns. The monoenergetic positron from $\pi \rightarrow e\nu$ has an energy of 69.3 MeV. Positrons from ordinary muon decay form the Michel spectrum from 0 to an endpoint of 52.3 MeV. The monoenergetic e^+ is well above the Michel endpoint and can be easily identified using a high-resolution, hermetic calorimeter. However, counting all $\pi \rightarrow e$ events with a precision at a few parts in 10^4 requires determining the low-energy tail of the shower that hides under the Michel spectrum from the $\pi \rightarrow \mu \rightarrow e$ chain, which has several orders of magnitude higher rate. It also demands that one understands non $\pi \rightarrow e$ events that reside above the Michel cutoff, such as ultra-rare muon decay-in-flight events and, less rare, Michel pileup events.

These challenges were critical to previous generation experiments and were responsible for their leading systematic uncertainties. We are designing an experiment that incorporates the “lessons learned” from PIENU and PEN efforts. Among the most important is development of a high resolution calorimeter with significant depth. Simulations show the importance of these parameters to determining the so-called tail fraction of the pienu peak that lies nominally hidden by the overwhelming Michel decay positrons. At present, we are exploring a high-resolution liquid xenon calorimeter, following the work of the MEG Collaboration, and we are also examining the use of LYSO crystals; this latter work is being done here at UW.

A better calorimeter alone is not enough. It is important to be able to create triggers that can isolate $\pi \rightarrow e$ from $\pi \rightarrow \mu \rightarrow e$ chains within the stopping target, including pion and muon decays in flight, as well as identify pileup from long-lived muons remaining in the target from earlier pion stops. To achieve these goals, we will use an active target (ATAR) that can provide 4D tracking (at the level of 150 μm in space and 100 ps in time) and energy measurements from the 30 keV (MIP) signals for electrons to the 4000 keV Bragg peaks of stopping pions and muons. Our collaboration is focusing on the new LGAD (low-gain avalanche diode) sensors as a centerpiece of the experiment. At UW, we are working closely with teams from UCSC and BNL on testing LGAD components here at CENPA, on aspects of the electronics chain, and importantly on simulations.

The experiment will require a 65-75 MeV/ c continuous wave pion beam with different characteristics for the two physics channels: 0.3 MHz with $\delta p/p \sim 1\%$ for $\pi \rightarrow e\nu$, and ≥ 10 MHz with $\delta p/p \sim 3\%$ for $\pi \rightarrow e\pi^0\nu$. These beams exist at PSI. We will need to deploy detector systems to image and trigger the arrival of pions into the ATAR. Because of the high data rate, state-of-the-art triggering, fast digitizing electronics, and high bandwidth data acquisition will be required. In 2022, we carried out a lengthy beam evaluation in the πE5 line, measuring flux and spot size over a variety of tunes and momenta.

The PIONEER Collaboration is drawn from groups having considerable experience in experimental precision physics, together with leading theorists who are carefully articulating the goals to maximize scientific impact. Member groups led previous generation rare pion decay experiments (PIENU, PEN and PiBeta), rare kaon decay experiments (BNL-E787/E949 and CERN NA62), stopped muon experiments (MEG, MuLan, MuCap and MuSun), and

Fermilab Muon $g - 2$. PIONEER has expertise in all the technical areas listed above.

In October 2022 we co-hosted a Rare Pion Decay Workshop¹ of theorists and experimentalists at UC Santa Cruz. This Workshop was generously supported by a grant we obtained from the Gordon and Betty Moore Foundation through the APS. The next major meeting will be held in Seattle in October 2023.

On the technical side, our group is leading the overall Simulation effort (Schwendimann, Buat, Labounty), development of the alternative LYSO crystal array (Beesley, Hertzog, Schwendimann, Swanson), and contributing significantly to the beam development design (Kammel) and the LGAD testing and concept our (Kammel, Braun, Buat). At present, we are using our Van de Graaff's Rutherford Backscattering (RBS) technique, which can provide heavy, slow protons into the ATAR planes to mimic the energy deposition expected from stopped pions or muons. In all the effort, CENPA lead engineer Roehnel is playing an important role in designing small test stand components and in advising on the overall PIONEER design.

As an example of recent lab work, grad student Beesley has been evaluating the light output, resolution, and longitudinal uniformity of new LYSO crystals. These are all critical parameters for the consideration of a full calorimeter for PIONEER. Fig. 4.6-1(left) shows a typical spectrum from a Na-22 511 keV line, and Fig. 4.6-1(right) shows the resolution observed using the gamma lines from a variety of sources, including Na-24, made using the CENPA Van de Graaff (See article by O. Beesley for details). Together with colleagues from the Shanghai Jiao Tong University, we are preparing an array of 10 LYSO crystals, surrounded by 4 large NaI crystals, to be used at PSI in a test-beam run in November 2023. The PSI π M1 beamline can provide a high-resolution electron beam in the range from 100 to 500 MeV, which will be idea to evaluate the performance of a small array. Our other PIONEER colleagues are preparing the electronics (Cornell) and DAQ (Kentucky) and beamline counters (PSI, Zurich, Stony Brook).

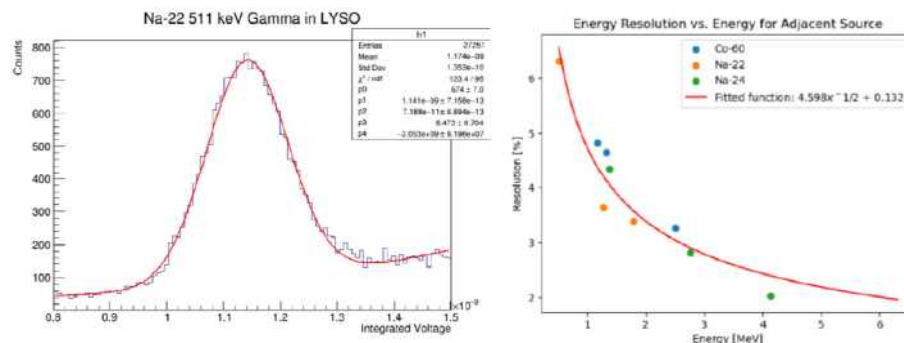


Figure 4.6-1. *Left*: Typical spectrum of a single LYSO crystal exposed to a Co-60 source. The 1.1 and 1.3 MeV lines are clearly resolved with good resolution. *Right*: The resolution vs energy assembled from a variety of laboratory sources as indicated. The energy can be characterized by the expression $\sigma/E = xx\%/\sqrt{(E)} + yy$, with E in GeV.

¹<https://indico.cern.ch/event/1175216>

4.7 Development of the PIONEER Simulation Framework

Q. Buat, J. LaBounty, and P. Schwendimann

As the PIONEER experiment intends to measure the branching ratio $R_{e/\mu}$ given in eq. (Sec. 4.6)(1) to a 10^{-4} precision, an extraordinary understanding of all processes and detector details is mandatory. To drive this endeavor, the development of a sophisticated simulation framework is led by the UW group and supported by more than a dozen collaborators around the globe. As currently many details are yet to be explored, the framework is designed in a very versatile and flexible way, consisting of four independent parts.

The first part encompasses the geometry description of the detector. It is written in python, making use of the python bindings provided by PyROOT. In a default configuration, the main geometry builder gets called with a JSON configuration file, providing parameters to predefined components in the detector assembly. It provides a GDML file readable by the GEANT4-based second part of the simulation. It is flexible enough such that any user can import the modules in a custom python script or add a custom python scripts to the builder to describe any desired geometry, such as a Liquid Xenon Prototype detector or a $g - 2$ calorimeter.

The second part deals with tracking particles through any previously defined geometries and computing particle hits and energy deposits in the specified sensitive detector areas. It is based on the GEANT4 package. At the current stage, it provides three different primary particle generation methods. By default, it provides a configurable pion beam aimed at the center of the detector, with optional muon and positron contamination. Alternatively, monochromatic signal-like positrons can be emitted from the target region with a defined angular direction. As a last option, the Geant4 native General Particle Source is available. It fully benefits from parallel processing on multiple CPU cores and writes the output to ROOT TTrees using custom classes with bindings provided for python users.

As understanding rare events is crucial to the success of the experiment - Measuring a 10^{-4} quantity to a 10^{-4} relative precision - event biasing is implemented. Amongst others, it is possible to enable/disable certain decay channels. This can for example be used to produce a high statistics $\pi \rightarrow e\nu$ sample without generating an unnecessary $10^4 \pi \rightarrow \mu\nu$ events per event of interest. Also, the muon decay was reimplemented to select muons that decay prior to a given time without disturbing the exponential lifetime of the muon in that time range. This is crucial to obtain a reasonable muon decay in flight (DIF) sample as this process is expected to occur for $\mathcal{O}(10^{-6})$ of all pion decays, thus an important contribution. More details on muon DIF are presented in (Sec. 4.9).

The third part is designed to deal with event mixing and the detector response. While this part is currently under heavy development, its importance is already quite clear. The muon lifetime is $2.197 \mu\text{s}$ and the pion beam rate is 0.3 MHz , suggesting an average separation of $\approx 3 \mu\text{s}$ and thus a high probability that a muon from a previous pion decay is still lingering around as a new pion enters the detector. Those are generally referred to as Old Muons. As a simple calculation shows with a very ambitious assumption that the calorimeter can fully

separate hits with a time difference of 10 ns, the probability for a pile up are still on the order of $\mathcal{O}(10^{-3})$, thus about ten times more likely than a $\pi \rightarrow e\nu$ event if not properly mitigated. While the designed output of this part is a ROOT TTree that contains data structures that emulate a digitized signal from the actual detector, a bypass is under construction that directly provides pseudo-reconstructed hits based on Monte Carlo truth values to start with the reconstruction development.

The last part that currently only exists as a concept on the drawing board is the full collection of reconstruction algorithms. It is supposed to take digitized data either from the detector itself or the detector response simulation and do the full reconstruction and fill histograms required by the analysis. At the current stage, various partial algorithms exist as ideas in the heads of individual developers or their personal laptops for testing. In addition, a Docker container is maintained that contains all crucial dependencies for the full framework, such that collaborators are not forced to deal with the details of software dependencies for their development endeavors.

While many parts of the simulation are still under development, it already provides data that reasonably models the expected behavior and allows starting designing reconstruction algorithms and test the respective performance under different detector assumptions. A qualitative example of an energy spectrum is shown in Fig. 4.7-???. With a total of 1.6×10^7 simulated events, the Michel spectrum from the $\pi \rightarrow \mu\nu, \mu \rightarrow e\nu\nu$ decay chain is clearly visible after some basic acceptance selection (blue) and the statistics of tagged pile up events (green) suffices for most purposes. However, dedicated runs with event biasing is required to get reasonable insights on the $\pi \rightarrow e\nu$ tail (red) and the rare muon DIF (purple).

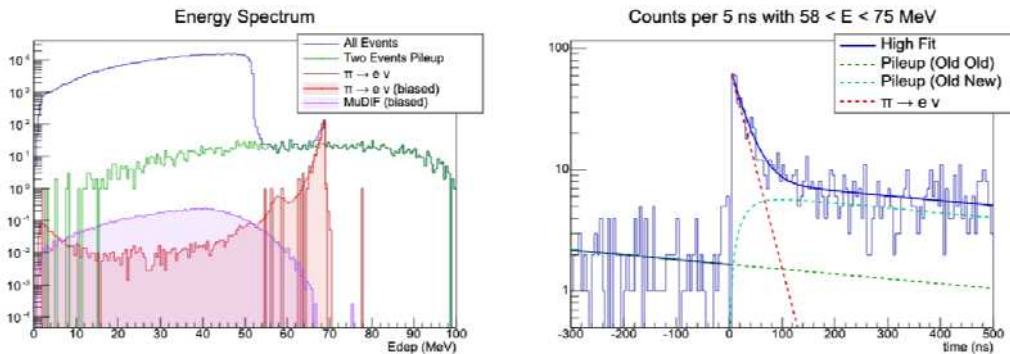


Figure 4.7-1. Proof of principle distributions in energy (left) and time (right) for different event types.

The time spectrum in Fig. 4.7-1 shows events with a pseudo-reconstructed energy between 58 MeV and 75 MeV, i.e. the range where $\pi \rightarrow e\nu$ events are expected. Events prior to the pion arrival ($t = 0$) originate from pile up of two old muons, denoted by Old-Old Pileup. Old-New Pileup on the other hand is a pileup of an old muon with a positron emitted from the triggering pion decay and the subsequent muon decay. Last, in the time region immediately after the pion arrival, a clear exponential decay due to $\pi \rightarrow e\nu$ events can be observed. Note that the dashed lines represent the components of the solid High Fit curve displayed. With the current low statistics in this plot and heavy development ongoing, this plot should be

taken as proof of principle only.

4.8 Characterization of LYSO:Ce as a PIONEER Calorimeter Option

O. Beesley, D. W. Hertzog, P. Schwendimann, and H. E. Swanson

To achieve the 2% energy resolution and 25 radiation length specifications for a PIONEER calorimeter, two calorimeter materials are considered: liquid xenon (LXe) and lutetium–yttrium oxyorthosilicate (LYSO) crystals. A LXe calorimeter would have excellent energy resolution approaching the 1.8% level, a fast response time of 45 ns, and uniform composition. The MEG charged-lepton flavor violation experiment at PSI has demonstrated the effectiveness of LXe as a calorimeter material in our energy range, but the challenges – both in cost and complexity of a larger LXe system necessitates the consideration of an alternative option. A PIONEER calorimeter made of tapered LYSO crystals provides more stopping power than LXe per unit cost, provides intrinsic segmentation for pileup reduction, and does not require the complex cryogenic systems needed to maintain a LXe calorimeter. Despite these advantages, a calorimeter of the scale needed to perform the PIONEER experiment has not been previously demonstrated. LYSO has worse energy resolution than LXe, but the best achievable energy resolution of LYSO at the energy scale relevant for PIONEER is unknown; previous tests of LYSO arrays have found energy resolutions at approximately the 4% level at 70 MeV. A LYSO calorimeter will require a significant quality control effort to calibrate each crystal and a demonstrated sufficient uniformity of crystal-crystal response in order to match the performance of single crystal bench tests.

Towards the exploration of a LYSO calorimeter for the PIONEER experiment, we will test the resolution of a 3 x 3 array of 2.5 x 2.5 x 18 cm of LYSO crystals surrounded by additional crystals used to catch leakage from the array at the energy scale of the PIONEER experiment. This beam test will be done with the PiM1 beam at PSI with a momentum resolution of 0.1% in November 2023. Prior to the beam test, ongoing work has been carried out to optimize the performance of LYSO crystals for the test. To characterize the energy resolution of an array, it is first necessary to understand the resolutions of its constituent crystals. The intrinsic resolution of a single LYSO crystal is determined by measuring the energy resolution of the crystal across a broad energy range and fitting the resulting energy resolution distribution as a sum of Poisson processes and a constant term. A 2.5 x 2.5 x 18 cm LYSO crystal produced by SICCAS was studied using the setup shown in Figure Fig. 4.8-1.

Three different radioactive sources were used in the determination of the LYSO crystal's resolution: a Na-22 source, a Co-60 source, and a Na-24 source. Each source emits two time coincident gamma rays and therefore provides three data points corresponding to each of the two gammas and their coincidence. The nine data points are then fit to determine the constant term in the energy resolution within a single crystal as shown in Fig. 4.8-2.

Extrapolation of the fits out to the PIONEER energy range finds contributions of less than 0.7% to energy resolution; it follows that inter-crystal miscalibration will become a dominant source of energy resolution for an array of LYSO crystals.

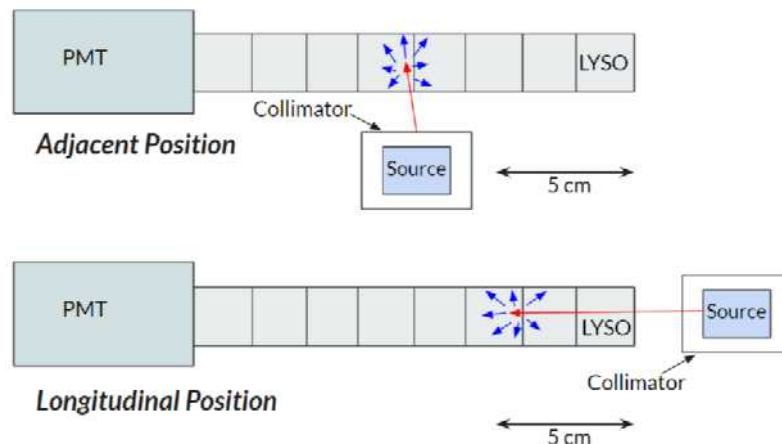


Figure 4.8-1. Diagrams of two source positions considered for determination of the dependence of energy resolution on energy for a single, unwrapped LYSO crystal. In the diagram labeled “Adjacent Position”, a source is placed next to the crystal so that gamma rays emitted by the radioactive source are directed by a lead collimator to the center of one of the 2.5 x 18 cm rectangular faces of the crystal. In the diagram labeled “Longitudinal Position”, a source is placed next to the crystal and opposite the PMT so that gamma rays emitted by the radioactive source are directed by a lead collimator to the center of one of the 2.5 x 2.5 cm square faces of the crystal. Light produced by the scintillating crystals will reflect along the sides of the crystals due to total internal reflection until it either attenuates or it reaches a PMT attached to the end of the crystal.

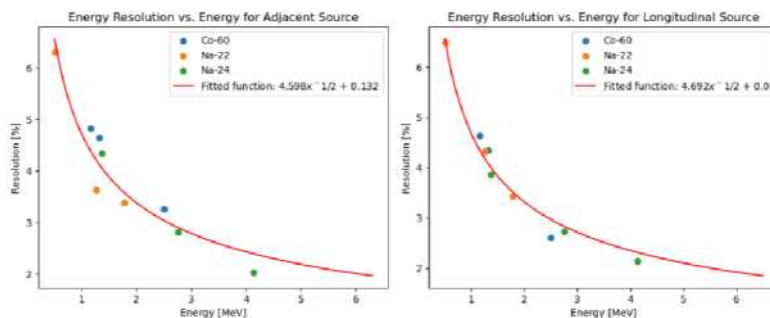


Figure 4.8-2. Plots of energy resolution dependence on energy for longitudinal and adjacent positioning of a radioactive source. Data points are fit separately for each source position and both fits find small contributions from the constant term of the fit to the energy resolution of the crystal; the constant term is $0.132\% \pm 0.477\%$ in the adjacent position and $0.000\% \pm 0.280\%$ in the longitudinal position.

4.9 Example of a PIONEER simulation study: decay-in-flight muon background

Q. Buat and P. Schwendimann

The PIONEER experiment aims in the first phase of the project at precisely measuring the ratio $R_{e/\mu} = \frac{BR(\pi \rightarrow e\nu(\gamma))}{BR(\pi \rightarrow \mu\nu(\gamma))}$. A measurement performed with a precision of 0.01 % would challenge the theoretical prediction from the Standard Model of Particle Physics, and any deviation from that prediction would be an unequivocal sign for new physics beyond the Standard Model.

To achieve this ambitious goal of $\frac{\Delta R_{e\mu}}{R_{e\mu}} < 10^{-4}$, the detector needs to be able to identify $\pi^+ \rightarrow e^+\nu(\gamma)$ events with a very good efficiency to build a very large dataset of $\approx 2e8$ $\pi^+ \rightarrow e^+\nu(\gamma)$ events over the planned years of data-taking. At the same time, the $\pi^+ \rightarrow \mu^+\nu(\gamma)$ events that occur at a much higher rate ($\approx 10^4$ higher than $\pi^+ \rightarrow e^+\nu(\gamma)$) need to be highly suppressed from the signal region (rejection rate of $\approx 10^6$).

The experiment is designed such that the charged pion (and the anti-muon in the case of the $\pi^+ \rightarrow \mu^+\nu(\gamma)$ decay) stop in the active target while the positron travels all the way to the calorimeter, which is designed to contain its shower. In most cases, the presence of an anti-muon in the decay chain will result in a very distinctive signature in the detector:

- The positron produced in the decay of an anti-muon will deposit less than 58 MeV in the detector while for most $\pi^+ \rightarrow e^+\nu(\gamma)$ events the deposited energy will be around 69 MeV;
- The MIP-level hits in the active target from the positron will be significantly delayed if they originate from an anti-muon decay due to the long lifetime of the muon ($2.2 \mu s$).

However, in the events where the anti-muon decays before coming to a stop (referred to in the rest of this report as Decay-In-Flight or DIF), the anti-muon residual momentum at the time of the decay is transferred to the positron. This can induce a larger energy deposited. Furthermore, the time separation of the anti-muon hits in the target and the MIP hits from the positron will typically be too small to be resolved by the detector as illustrated on Fig. 4.9-1 (left). Using the latest version of the PIONEER simulation, we compared the size of this class of background events with the signal events on Fig. 4.9-1 (right) and observed that the DIF background was very large.

The $R_{e/\mu}$ measurement strategy planned for PIONEER follows closely the analysis conducted by the PIENU experiment. Events will be split in two energy bins (high and low) as displayed on Fig. 4.9-1(right). In each bin the signal and background components will be extracted with a template fit of the timing distribution.

In order to satisfy $\frac{\Delta R_{e\mu}}{R_{e\mu}} < 10^{-4}$, some critical performance criteria must be achieved:

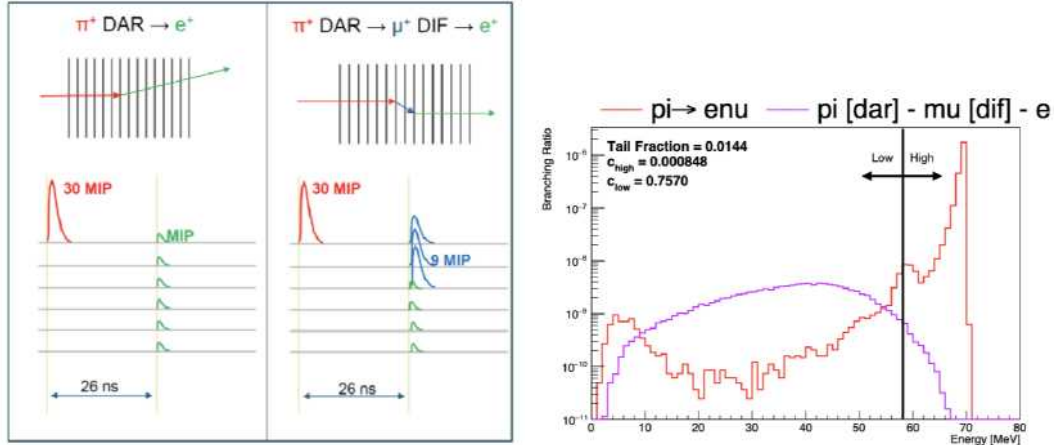


Figure 4.9-1. Sketch and energy distribution comparing $\pi^+ \rightarrow e^+\nu(\gamma)$ events and $\pi^+ \rightarrow \mu^+\nu(\gamma)$ events where the anti-muon decays in flight. *Left:* Sketch illustrating the signature of $\pi^+ \rightarrow e^+\nu(\gamma)$ event (left) and a $\pi^+ \rightarrow \mu^+\nu(\gamma)$ event where the anti-muon decays in flight. *Right:* Deposited energy for $\pi^+ \rightarrow e^+\nu(\gamma)$ events (in red) and $\pi^+ \rightarrow \mu^+\nu(\gamma)$ events where the π^+ comes to a rest before decay but the μ^+ decays in flight.

1. The signal *Tail Fraction*¹ must be around 1-2 %;
2. the background contamination (c_{high}) in the high bin needs to be below 10^{-4} ;
3. in the absence of any auxiliary measurement to determine it precisely, the background contamination (c_{low}) in the low bin should be around 1 %.

As reported on Fig. 4.9-1 (right), the *Tail Fraction*, at 1.4 %, is within the design requirement. However for the DIF background, $c_{high} = 8 \cdot 10^{-4}$ and $c_{low} = 75 \%$ are significantly higher than desired. In order to reduce the contamination in the low and high bins, we can leverage the information measured in the highly segmented ATAR detector.

Using timing information, the last hit of the charged pion can be easily identified. As illustrated on Fig. 4.9-2(left) there is a very strong correlation between deposited energy and path travelled. Since the energy deposited in the strip where the charge pion stopped can be measured within a time window of a few nanoseconds, we can exploit this correlation to infer where the charged pion stopped, and subsequently we can measure the dE/dx distribution of the track formed by the charged pion decay as illustrated on Fig. 4.9-2 (right).

This approach yields very promising results, as illustrated on Fig. 4.9-3. Applying a criterion on this dE/dx calculation along the beamline reduces c_{high} from $8 \cdot 10^{-4}$ to $0.4 \cdot 10^{-4}$ and c_{low} from 75 % to 12 % as illustrated on Fig. 4.9-3(right).

While this represents a significant reduction of the DIF background, the contamination in the low bin is still fairly high. Several ideas are being pursued to understand how to further reduce the DIF background:

¹The *Tail Fraction* is defined as the ratio of the signal contribution to the low energy bin over the total number of signal events

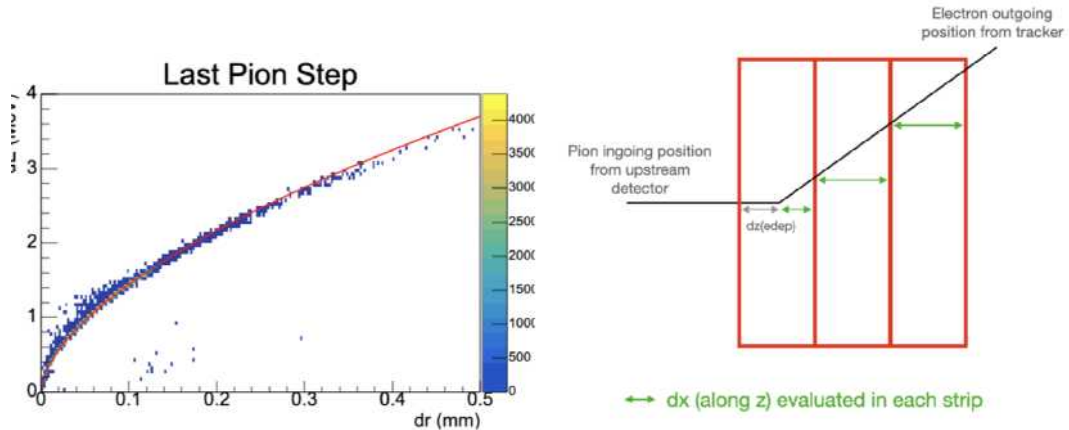


Figure 4.9-2. dE/dx calculation along the beamline. *Left:* Energy vs path travelled of the last pion step in the geant-4 simulation of the target. *Right:* Sketch of the dE/dx calculation along the beamline.

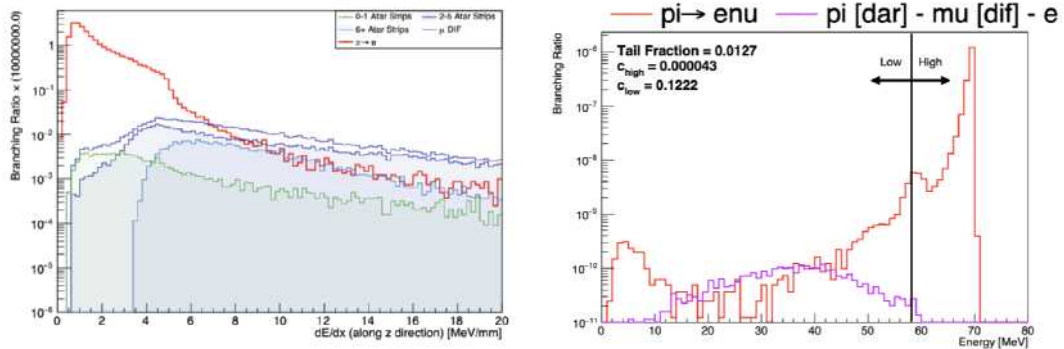


Figure 4.9-3. Performance of the dE/dx criteria. *Left:* dE/dx distribution for $\pi^+ \rightarrow e^+\nu(\gamma)$ events (red) and DIF events. The DIF events are split based on how many strips in the target the muon travels through before decaying. *Right:* Deposited energy for $\pi^+ \rightarrow e^+\nu(\gamma)$ events (in red) and $\pi^+ \rightarrow \mu^+\nu(\gamma)$ events where the π^+ comes to a rest before decay but the μ^+ decays in flight. Distributions are shown after a cut on the dE/dx calculation along the beamline.

- using angular information of the outgoing track through the target and the tracker, the path of the pion decay products can be better estimated, which should yield sizeable improvements to the dE/dx criteria;
- using deposit of the previous to last hit of the charged pion in the target can help to better determine where the pion stops;
- using deep learning techniques, a discriminant could be trained using the position, energy and time information of each recorded hit;
- using the recorded pulse shape in the strips hit by the pion decay products, the angle at which the deposit happens could be determined.

All these directions are currently being explored and in the meantime, the analysis is being repeated with newer version of the simulation to make sure it can inform as accurately as possible the prototyping of the experiment.

MuSun

4.10 Muon capture and the MuSun experiment

D. W. Hertzog, [P. Kammel](#), E. T. Muldoon, and D. J. Prindle

Muon capture is a powerful tool to study the properties and structure of the nucleon and few nucleon systems as predicted by effective field theories (EFT) founded on Quantum Chromodynamics. Our program focuses on capture from the simplest muonic atoms, namely on the proton (MuCap experiment) as well as on deuterium (MuSun experiment). Substantially improved precision is enabled by a novel active-target method based on the development of high-pressure time-projection chambers (TPC) filled with hydrogen/deuterium gas, which our collaboration pioneered.

The goal of the MuSun experiment is a first precise measurement of a weak process in the 2-nucleon (2N) system. These reactions include muon capture on the deuteron, $\mu + d \rightarrow n + n + \nu$, together with two astrophysics reactions of fundamental importance, solar pp fusion and νd reactions, where the latter provided the evidence for solar neutrino oscillations. The extremely small rates of these processes do not allow their cross-sections to be measured precisely; they must be calculated by theory, with information derived from the more complex three-nucleon system. These interactions all involve the same axial-vector coupling at a four-nucleon vertex, characterized by a single common low-energy constant (LEC) d^R in the EFT description. This LEC is also an essential ingredient in the construction of chiral three-nucleon forces and in other weak and strong dynamics. MuSun plans to determine the rate Λ_D of muon capture on the deuteron to 1.5%, where Λ_D denotes the capture rate from the μd doublet hyperfine state. Current experiments are at the 6-10% level, and the most precise one disagrees with the latest theory calculations^{1,2} $\Lambda_D = 399.1 \pm 8.8 \text{ s}^{-1}$ and $393.8 \pm 4.4 \text{ s}^{-1}$

¹B. Acharya et al., Phys. Rev. C **107**(6), 065502 (2023).

²A. Gnech et al., arXiv:2305.07568 [nucl-th] (2023)

by more than 3 standard deviations.

The MuSun experiment uses the so-called “lifetime method” consisting of a precision measurement of the muon disappearance rate $\lambda_{d\mu}$ in deuterium. As $\lambda_{d\mu} \approx \lambda_{\mu^+} + \Lambda_d$ and the free muon decay rate λ_{μ^+} is known¹ to 1 ppm, a 13 ppm measurement of $\lambda_{d\mu}$ is required. Muons are stopped in a cryogenic time projection chamber filled with ultrapure deuterium gas. Decay electrons are detected in two cylindrical wire chambers and a segmented scintillator barrel. The experiment must simultaneously meet several stringent requirements. i) The target conditions (T=31 K and density 6.5% of liquid-hydrogen density) are optimized for an unambiguous extraction of Λ_D , and the suppression of muonic atomic physics complications that arise when muons stop in deuterium, such as muon-catalyzed fusion. ii) Muons are tracked in three dimensions in the active target TPC, which eliminates most muon stops in wall material. iii) Muon transfer to impurity elements is suppressed by keeping and monitoring the gas contamination at the 10^{-9} level. After several technical developments and upgrades, MuSun collected its full statistics of 1.4×10^{10} events in two main production runs R2014 and R2015 at PSI, followed, in 2016, by a shorter systematic run.

In order to achieve the required precision in Λ_D both statistical and systematic uncertainties should not exceed $\pm 4 \text{ s}^{-1}$. Such a precision requires careful attention to systematics from physical as well as instrumental effects. In particular, early-to-late effects within the fit range of 1-24 μs must be tightly controlled. Additional analysis challenges were introduced by the poorer beam quality of the new beamline, where the experiment had to relocate after the development phase. The final analysis at the required level is performed by the UW group, with the several milestones achieved this year.

Effect		Shift (s^{-1})		Uncertainty (s^{-1})	
		R2014	R2015	R2014	R2015
Beam	Pileup	1.5		1.5	
	MORE	≈ 0		0.25	
	Slope	-9.8	-5.7	2.1	1.5
TPC	Fusion	-0.2	-1.6	1.2	0.9
	Electron	8.2	3.1	3.9	2.9
Purity	Wall Stops	≈ 0		≈ 0	
	Isotopic	0.8		0.2	
	Chemical	5.2	4.1	0.6	0.5
Electrons	Afterpulses	-0.54		0.64	
Total		5.16	1.66	4.9	3.8

Table 4.10-1. Summary of the major systematic effects in the MuSun experiment. Some R2014 estimates are preliminary and subject to change.

In the PhD. Thesis of Ethan Muldoon (June 2023) systematic effects were comprehensively evaluated with uncertainties close to the proposal goal. Table 4.10-1 gives an overview of the current status, which the largest corrections discussed below. An optimized muon stop definition is essential, as pile-up with decay electrons and muon-catalyzed fusion recoils can

¹V. Tishchenko et al., Phys. Rev. D **87**(5), 052003 (2013).

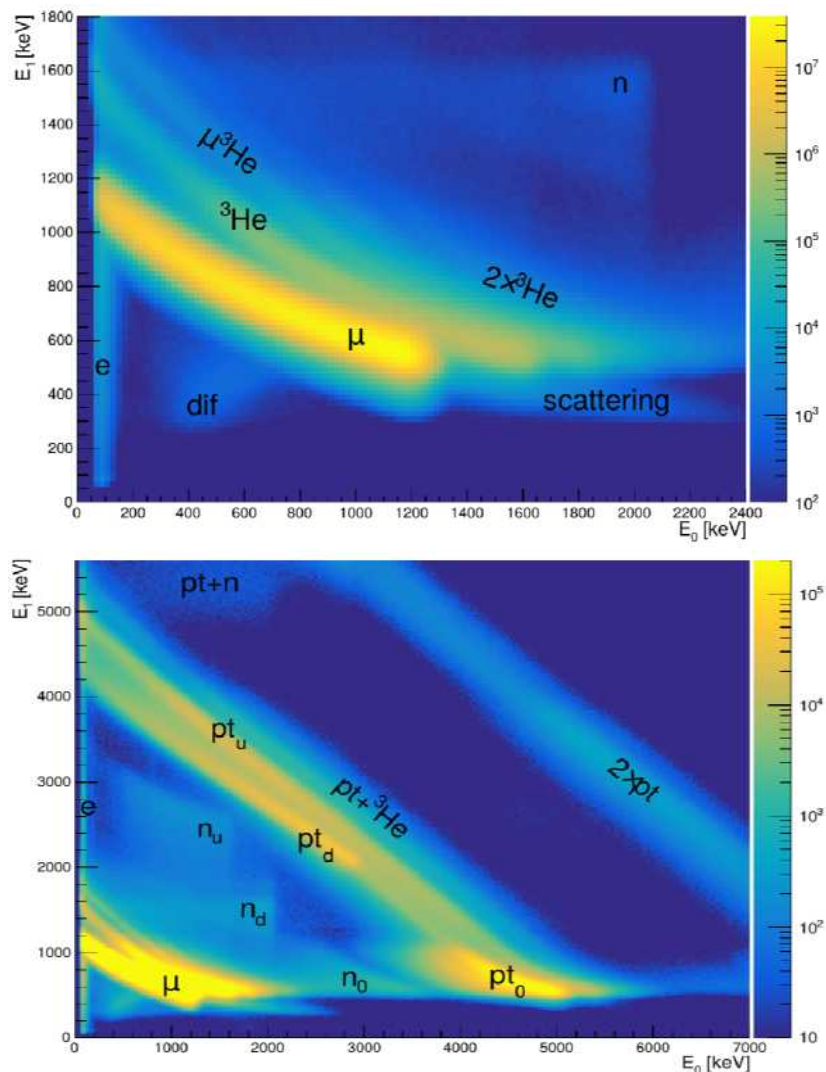


Figure 4.10-1. E_1 vs. E_0 histograms. Top: The low energy region is dominated by the main muon stop band (μ) reflecting the Bragg energy loss relation in the two last pad rows, and various less intense bands of decay electron energy deposit (denoted by e) and pileup from ${}^3\text{He} + n$ fusion. Bottom: At higher energies p+t fusion pile-up becomes the dominant feature where the pt energy is contained in the stop row (pt_0) or the proton travels up (pt_u) or downstream (pt_d). Figures will be updated.

potentially lead to misreconstruction of the muon stopping point. In case the misreconstructed events cross TPC fiducial boundaries, these lost events induce a distortion of the originally nearly exponential decay spectrum. Two-dimensional histograms of the intensity distribution in the penultimate pad E_1 vs. the stop pad E_0 are powerful tools to identify event classes and their properties. The events indicated in Fig. 4.10-1 consists of muon stops and their secondary particles namely decay electrons as well as p+t and ${}^3\text{He}+n$ from muon-catalyzed dd fusion. The energy deposit from electrons is small, whereas p+t fusion can deposit 4 MeV or even 8 MeV for overlapping double fusions (right side of Fig. 4.10-1). Electrons piling-up with the stopping muons are identified in specific regions of the E_0 - E_1 plane, e.g. region e in

Fig. 4.10-1, and, after studying their properties and impact on the lifetime, their overall effect can be estimated. Muon-catalyzed fusion products, which for long have been considered the most dangerous background, are now well controlled. An advanced track finder minimizes the tracking errors and remaining losses can be accurately quantified based on the early part of the muon-electron time spectrum, which is not included in the final lifetime fit.

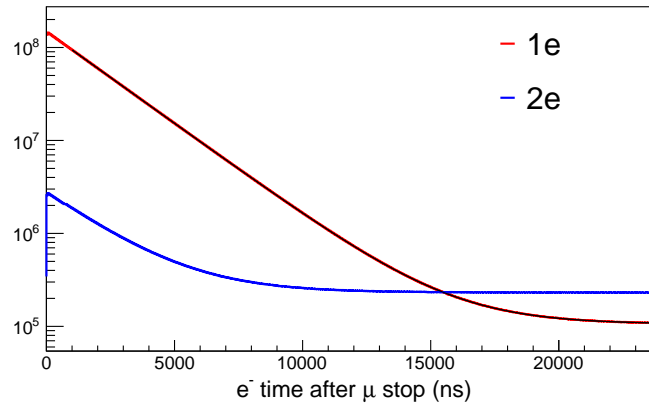


Figure 4.10-2. Muon decay spectra from scintillators observed in R2014 requiring one (1e) or two (2e) electrons in the region of interest. The data is fitted to a single exponential and an accidental component with a small linear term in the range 1-24 μ s. Data and fit curves are basically indistinguishable.

The muon decay spectra, see Fig. 4.10-2, are built by histogramming the electron scintillator barrel hits against the entrance scintillator time for muons that were tracked to stops inside the fiducial volume of the TPC. The time spectra shown in the figure are sorted depending on whether only one (1e), or two (2e) electrons were detected in the region of interest 0-24 μ s after muons stop, which suppress and enhance accidentals, respectively. With this method, a slight slope of the accidental background is observed, which is probably related to the fast kicker, and accounted for in a simultaneous fit of both spectra. Trace N_2 contaminants in the ultrapure and isotopically clean D_2 gas are monitored at the ppb level by gas chromatography and direct detection of recoil nuclei from $\mu + N \rightarrow C^* + \nu$ in the TPC, which was achieved in a challenging analysis by Prindle. Finally, a long-standing analysis problem was resolved, which seemed to indicate a significant and ununderstood dependence of the measured lifetime on the muon stop position in the TPC. This problem only occurred when a dE/dx cut in the first TPC pad-row was employed to tighten the muon stopping distribution in the beam direction, and was explained by a subtle cross talk between TPC pads by capacitive coupling via the Frisch grid.

The UW group plans to finish the analysis over the summer, focusing on consistency checks and tightening the electron pile-up correction uncertainty. An unblinding meeting is planned at UW in the fall after collaboration review of the analysis reports. We anticipate to publish a first physics results in PRL, followed by a long paper documenting the novel experimental approach used in MuSun.

5 Dark matter searches

ADMX (Axion Dark Matter eXperiment)¹

5.1 Searching for QCD axions between 800 MHz and 1.4 GHz

C. L. Bartram*, T. Braine, N. Du[†], M. Guzzetti, C. Goodman, C. Hanretty, G. Leum[‡], L. J. Rosenberg, G. Rybka, J. Sinnis, and D. Zhang

The Axion Dark Matter eXperiment (ADMX) is an axion haloscope² housed at the University of Washington’s Center for Experimental Nuclear Physics and Astrophysics. It consists of a 136-liter cylindrical, copper-plated, resonant microwave cavity with two copper tuning rods that is immersed in a ~ 7.6 Tesla superconducting solenoid. The magnetic field stimulates the decay of axions into microwave photons producing a signal which, when on resonance with the cavity frequency, becomes amplified making something once thought to be undetectable, detectable.

Axions were first proposed as a solution to a long-standing mystery related to the quantum chromodynamics (QCD) Lagrangian, known as the strong CP problem, by Peccei & Quinn in 1977³. Not long after the axion was introduced, physicists realized that its properties such as electric neutrality, feeble interactions with standard model particles, and abundant production in the early universe make it a compelling dark matter candidate as well.

There are two benchmark models that describe the QCD axion: the Kim-Shifman-Vainshtein-Zakharov (KSVZ)^{4,5} model and the Dine-Fischler-Srednicki-Zhitnitsky (DFSZ)^{6,7} model. Many find the more weakly coupled of the two, DFSZ, to be more compelling due to its compatibility with Grand Unified Theories. However, reaching this level of sensitivity turns out to be nontrivial. ADMX was the first group to reach DFSZ⁸, and to date remains one of only two groups⁹ that have reached it at all.

So far, ADMX has excluded both KSVZ and DFSZ axions between 645-800 MHz (2.66-3.3 μeV) over the course of two data taking runs^{10,11}. Additionally, ADMX excluded KSVZ

*Presently at SLAC, Menlo Park, CA.

[†]Presently at Lawrence Livermore National Laboratory, Livermore, CA.

[‡]Presently at Microsoft Quantum, Redmond, WA.

¹ADMX is supported by the DOE Office of High-Energy Physics and makes use of CENPA resources by recharge to the cost center.

²P. Sikivie, Phys. Rev. Lett. **51**, 1415 (1983).

³R.D. Peccei and H. Quinn, Phys. Rev. Lett. **38**, 1440 (1977).

⁴J.E. Kim, Phys. Rev. Lett. **43**, 103 (1979).

⁵M.A. Shifman, A.I. Vainstein, and V.I. Zakharov, Nucl. Phys. **B166**, 493 (1980).

⁶M. Dine, W. Fischler, and M. Srednicki, Phys. Lett. **B104**, 199 (1981).

⁷A.R. Zhitnitsky, Sov. J. Nucl. Phys. **31**, 260 (1980).

⁸N. Du et al. (ADMX Collaboration), Phys. Rev. Lett. **120**, 151301 (2018).

⁹Andrew K. Yi et al. (ADMX Collaboration), Phys. Rev. Lett. **130**, 071002 (2023).

¹⁰N. Du et al., Phys. Rev. Lett. **120** 151301 (2018).

¹¹T. Braine et al., Phys. Rev. Lett. **124** 101303 (2020).

and DFSZ axions between 800-1015 MHz (3.3-4.2 μeV) and 943-991 MHz (3.9-4.1 μeV) respectively during its third data taking run¹. During this run, we encountered experimental challenges such as damage to our helium liquefier, and a persistent cold vacuum leak that halted data taking for quite some time, leading to only a portion of this frequency range reaching DFSZ. Over the last year the ADMX group has worked diligently to get the experiment into a healthy state so that we could fill in some of the parameter space that did not reach DFSZ sensitivity the first time around before moving onto the next planned frequency range for ADMX (nominally 1-1.4 GHz). The preliminary results from this data taking run are plotted in Fig. 5.1-1.

In addition to this final push to get data in the frequency range up to 1 GHz, the first few months of 2023 were spent preparing for our next data taking run. As aforementioned, this run is designed to search for DFSZ axions in the 1-1.4 GHz range, as can be seen in the sensitivity projection in Fig. 5.1-1. This new frequency range requires some upgrades to the system such as swapping out the cavity for one with a single copper tuning rod, allowing us to scan higher frequencies using the same magnet bore. We are also in the process of upgrading and/or replacing various experimental components, such as our Josephson Parametric Amplifier and some of our existing cryogenic DC and RF cables. Additionally, we have been working on improving the experimental site plumbing for our 1K pots. This upgrade will allow for individual pumping on and operation of our two 1K Pots, as well as providing additional protections during their operation. Improved heat sinking and insulation against thermal radiation will also help to improve our low temperature operations in this upcoming data taking run.

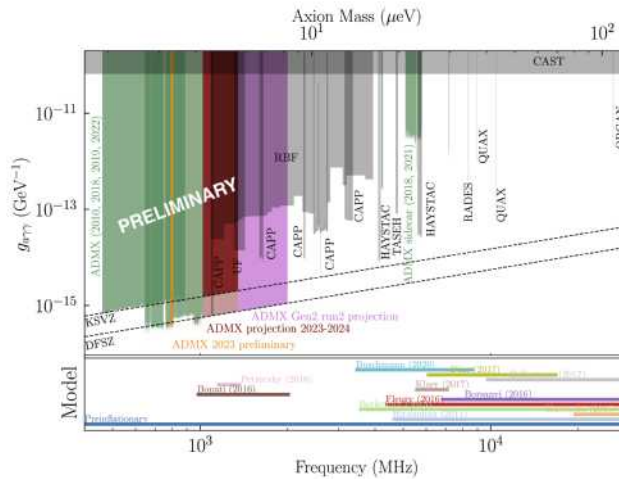


Figure 5.1-1. Axion-photon coupling constant sensitivity plot. The vertical axis is the axion-photon coupling constant, $g_{a\gamma\gamma}$, with smaller values indicating higher sensitivity. The two horizontal axes are axion mass and frequency respectively. Exclusion limits previously set by ADMX are shown in green, while those set by other experiments are shown in gray. Additionally, preliminary exclusion limits for ADMX’s most recent data taking run are shown in orange, and the projected sensitivity for our upcoming data taking run are shown in dark red.

¹C. Bartram et al. (ADMX Collaboration), Phys. Rev. Lett. **127**, 261803 (2021).

5.2 Preparing for a high frequency axion search with ADMX Orpheus

R. Cervantes*, G. Rybka, and J. Sinnis

Orpheus is a pathfinder axion haloscope project, which uses a novel cavity design to search for axions in mass ranges generally above the values that traditional tunable haloscopes are sensitive to. Orpheus searches for axions with the 18th order TEM mode of a Fabry-Perot interferometer. The frequency of this mode is tuned from about 15.8-16.8 GHz, which corresponds to axion masses of roughly 65-70 μeV . Generally, the use of the higher order modes of a resonator in an axion search is not feasible, because the axion signal power scales with the effective volume V_{eff} , which follows this proportionality relation:

$$V_{eff} \propto \int \vec{E} \cdot \vec{B} d^3x \quad (1)$$

where \vec{E} is the electric field of the mode used to search for the axion and \vec{B} is an externally applied magnetic field. The direction of \vec{B} is fixed, so using a higher order mode for \vec{E} introduces oscillations into the integral which cancel out. To avoid this cancellation of the effective volume, dielectric plates are placed along the length of the resonator with even spacing, such that select oscillations of \vec{E} have diminished amplitudes. This reduces the cancellation due to the oscillations in the integral.

In late 2021, Raphael Cervantes (currently at the SQMS center at Fermilab) conducted a dark photon search with the Orpheus haloscope¹². The dark photon search is identical to a search for axions except that it does not require an applied magnetic field. James Sinnis, a graduate student in the ADMX group at CENPA, is continuing the Orpheus project by constructing a superconducting magnet. The magnet was wound and potted in 2022, and the full experiment is now in the process of final assembly. We expect this process to be finished by the end of this summer. If the magnet is demonstrated to work then we will conduct an axion search with Orpheus in the Winter of 2023.

DAMIC

5.3 DAMIC-M CCD Array

K. Aragon, A. E. Chavarria, M. Conde, M. Huehn, H. Lin, K.J. McGuire, A. Piers*,
R. Roehnelt, and M. Traina

The DAMIC-M experiment will search for the interaction of dark matter particles in the galactic halo with silicon atoms in the fully-depleted active region of scientific charge-coupled

*Presently at FNAL, Batavia, IL.

*Presently at RKF Engineering, Bethesda, MD, 20814-6198.

¹R. Cervantes et al., Phys. Rev. Lett. **129**, 201301 (2022).

²R. Cervantes et al., Phys. Rev. D **106**, 102002 (2022).

devices (CCDs). The DAMIC-M detector will deploy an array of ~ 200 skipper CCDs with sub-electron resolution (~ 700 g of sensitive mass). The detector will be constructed in an ultra low-background environment (~ 0.1 dru¹), in the Modane Underground Laboratory (LSM) under the French Alps. The design of the CCD array and the evaluation of its performance are the responsibility of the DAMIC-M group at CENPA².

Over the past year, the design of the four-CCD module was finalized. Two modules that were fabricated on UW campus (Washington Nanofabrication Facility (WNF) and DAMIC-M PAB lab) were deployed in the DAMIC-M test setup at LSM (Fig. 5.3-2, left). These modules have been tested extensively, demonstrating the performance required for the DAMIC-M detector. In parallel, we are prototyping the design of the CCD array, with evaluations of thermal and mechanical performance being conducted at NPL.

Leakage current across the CCDs can limit DAMIC-M sensitivity to hidden sector dark matter candidates³. To minimize leakage current and maintain optimal charge transfer efficiency, DAMIC-M CCDs must be operated at temperatures between 120 K and 140 K. An increase of 7 K in CCD temperature is expected to produce an order of magnitude increase in leakage current. For this reason, it is critical that device temperature stays uniform across the detector array, and therefore across the 13 modules making up one of its four arms. Our group designed and tested a thermal evaluation setup consisting of 13 mock modules stacked horizontally (a quarter of the array) and installed in a copper assembly surrounded by an infrared (IR) shield (Fig. 5.3-2, right). The thermal chain across the array consists of a repeating sequence of chemically cleaned copper, Kapton and silicon. Thin (~ 1 cm) copper bars are sandwiched between the Kapton flexprint glued on one module and the back of the silicon of another module. Each mock module is equipped with two thin-film platinum resistance temperature sensors (RTDs) with 0.1 K accuracy. Thermal tests are conducted in the DAMIC-M cryogenic test chamber at NPL, which features an LN2-based cooling system with full remote control capabilities. The required performance of ~ 1 K temperature gradient across the array was recently achieved (Fig. 5.3-1), after few iterations on the array design. The lessons learned in the process inform the design and protocol for the deployment of the DAMIC-M array.

¹1 dru = 1 keV⁻¹ kg⁻¹ day⁻¹

²CENPA Annual Report, University of Washington (2021) p. 133.

³DAMIC-M Collaboration, Phys. Rev. Lett. **130**, 171003 (2023).

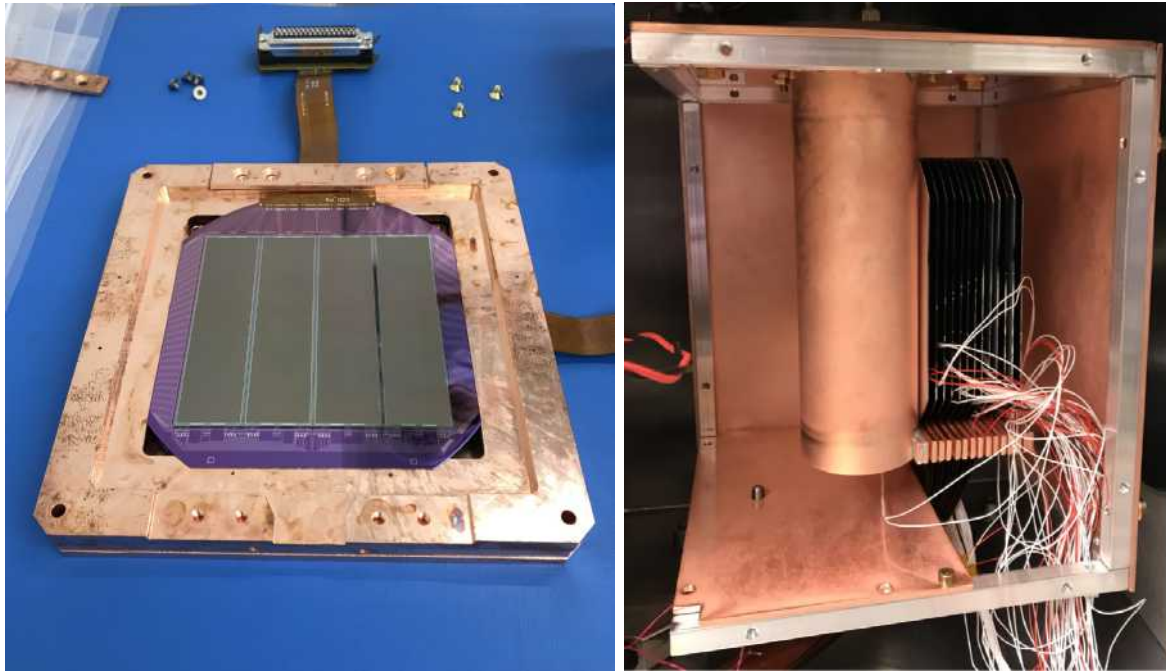


Figure 5.3-1. *Left:* DAMIC-M module prototype installed in its oxygen-free high-conductivity copper box, before installation in the DAMIC-M Low Background Chamber. The four $6k \times 1.5k$ skipper CCDs are glued and wirebonded to the silicon pitch adapter, which features aluminum traces to carry control and readout signals. *Right:* DAMIC-M mock quarter array installed in the (partially assembled) copper IR shield. The 16 copper bars forming the thermal chain across the array and temperature-control wires are visible.

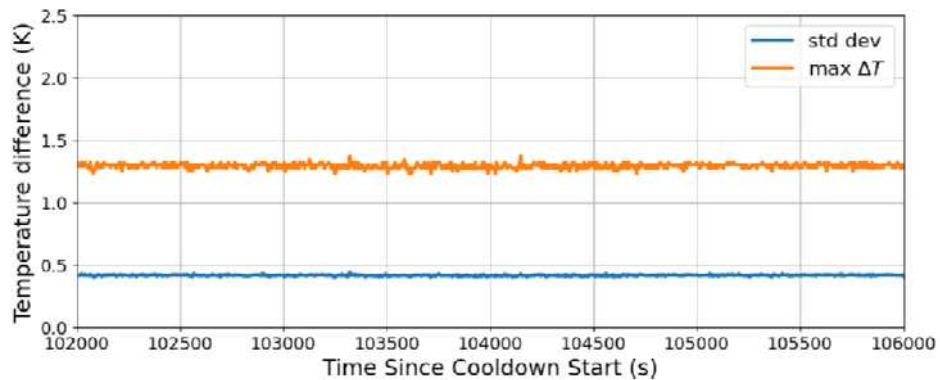


Figure 5.3-2. Thermal performance of the DAMIC-M mock quarter array at NPL. The standard deviation and maximum difference in temperature across the modules as a function of time at $T = 100.0\text{ K}$ are shown in blue and orange, respectively.

5.4 DAMIC at SNOLAB upgrade with skipper CCDs

A.E. Chavarria, M. Conde, M. Huehn, K.J. McGuire, D. Peterson, A. Piers*, and M. Traina

DAMIC (Dark Matter in CCDs) at SNOLAB is a low threshold dark matter experiment installed beneath 2 km of granite in the Vale Creighton Mine near Sudbury, Canada¹. The DAMIC group at CENPA upgraded the DAMIC at SNOLAB apparatus in October 2021, decommissioning the former seven CCDs with conventional readout to install two 24-megapixel CCDs with skipper readout and sub-electron resolution. Only minor modifications were made to the rest of the apparatus, which features the same copper, lead and polyethylene shielding as the previous installation. The skipper upgrade of DAMIC at SNOLAB was commissioned for operations with a sub-electron noise of $0.2 e^-$, leakage current of $\sim 10^{-3} e^-/\text{pix}/\text{day}$, and background rate of $\sim 10 \text{ dru}^2$, compatible to the rate measured with the previous apparatus. The factor of 10 reduction in readout noise enables lower energy threshold (previously 50 eV_{ee}) and better spatial reconstruction of ionization events.

Following the optimization of detector operation parameters, we conducted a science run using both skipper devices to investigate the statistically significant excess of low-energy bulk events ($E < 0.5 \text{ keV}_{ee}$) previously observed above expected backgrounds³. Details of the experiment and results are on the arXiv⁴. We acquired a total target exposure of $4.8 \text{ kg}\cdot\text{day}$ throughout 2022. The cluster search was performed using a likelihood clustering algorithm⁵, where the likelihood ratio $\Delta LL = -\mathcal{L}_g/\mathcal{L}_n$ is computed for the hypotheses that the charge in a pixel window of preset size comes from an ionization event and noise (\mathcal{L}_g), and from noise only (\mathcal{L}_n). For each cluster found with a soft cut on ΔLL , a stricter, charge-dependent cut was applied on ΔLL to discriminate noise accidentals from ionization events. To address the dominant systematic uncertainty of the previous analysis—the detector response to CCD surface events—we performed the spectral analysis after selecting events in the bulk of the CCD from the lateral spread of the pixel clusters (σ_{xy}) (Fig. 5.4-1). The lateral spread is related to the depth (z) of ionization events by the charge diffusion model, which was calibrated on muon surface data and validated experimentally for surface events at the University of Washington (Sec. 5.6).

To confirm that the previously constructed background model³ retained its validity, we analyzed the measured ionization spectrum between 0.5 keV_{ee} and 20 keV_{ee} . The overall (bulk) background rate in the $1\text{--}6 \text{ keV}_{ee}$ energy range of 9.7 ± 0.8 (4.4 ± 0.6) dru was found to be comparable to the previous installation. A detailed spectral analysis revealed the anticipated cosmogenic tritium spectrum within the CCDs bulk ($Q_\beta = 18.592 \text{ keV}$), accompanied by a constant contribution from Compton scattering of external γ rays. These contributions are expected to dominate at lower energies too. We thus assumed a flat background model

*Presently at RKF Engineering, Bethesda, MD, 20814-6198.

¹CENPA Annual Report, University of Washington (2021) p. 126.

² $1 \text{ dru} = 1 \text{ keV}^{-1} \text{ kg}^{-1} \text{ day}^{-1}$

³DAMIC Collaboration, Phys. Rev. D **105**, 062003 (2022).

⁴DAMIC Collaboration, arXiv:2306.01717 (2023).

⁵DAMIC Collaboration, Phys. Rev. D **94**, 082006 (2016).

below 0.5 keV_{ee} . The reconstructed bulk ionization spectrum (Fig. 5.4-2, left) confirms with high significance (5.4σ) the presence of an excess population of low-energy events above our background model. The excess population is statistically compatible with the previous result from DAMIC at SNOLAB, with a rate of ~ 7 events per kg-day and exponential decay constant of $\sim 80 \text{ eV}_{ee}$ (Fig. 5.4-2, right). The observed excess ionization events likely arise from an unidentified source of radiation in the DAMIC detector or from the environment, which is common to the two experiments.

The DAMIC-M detector, a 0.7 kg skipper-CCD array with a radioactive background rate of $\mathcal{O}(0.1)$ dru, will start operations at the Modane Underground Laboratory (LSM) in late 2024. If the bulk excess is detected in DAMIC-M, a high-resolution spectral measurement, time evolution studies of the excess, and investigations of its dependence on detector configuration and operating parameters will be possible to better understand its origin.

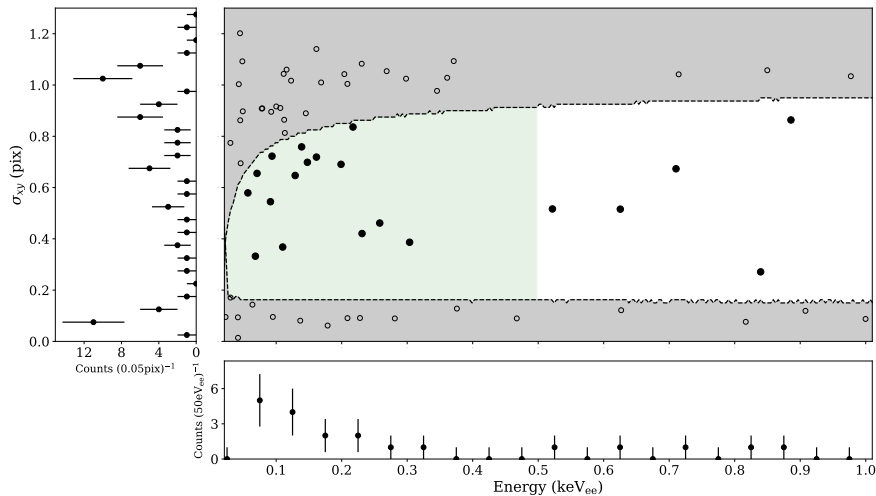


Figure 5.4-1. Distribution of clusters in energy vs. σ_{xy} space for $E \in [0.023, 1] \text{ keV}_{ee}$. Clusters with large (small) σ_{xy} correspond to events occurring in the back (front) of the CCDs. Grey regions are excluded by the 95% surface event rejection, which results in the final sample of bulk events (filled circles). The green-shaded region represents the energy ROI ($E < 0.5 \text{ keV}_{ee}$) for bulk events. The left (bottom) panel shows the σ_{xy} (energy) projection of all (bulk) events.

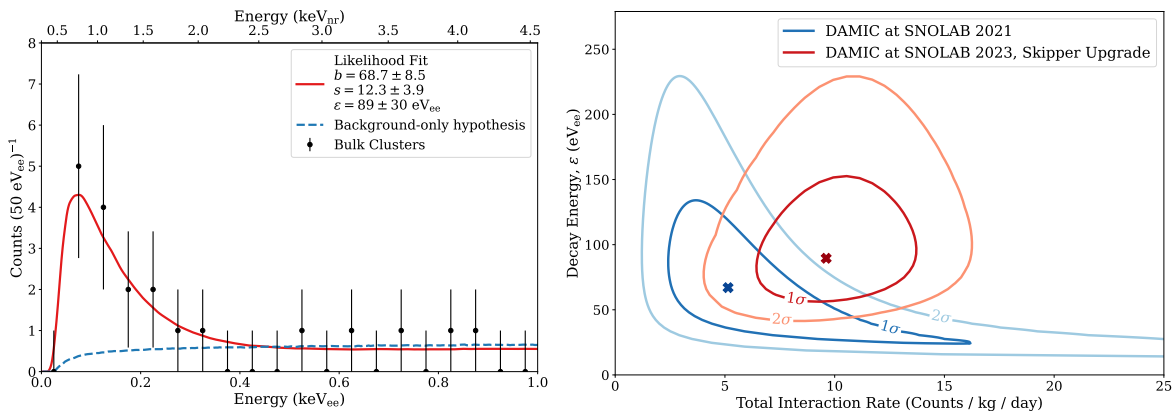


Figure 5.4-2. *Left:* Result of the fit to bulk events with the exponential excess + background (red) and the background-only (blue dashed) hypotheses. The fit prefers a low-energy exponential component. *Right:* Comparison of the allowed parameter space of the bulk excess measured in this work and the previous 11 kg-day analysis³.

5.5 Search for sub-GeV dark matter particles with DAMIC-M

A.E. Chavarria, M. Conde, M. Huehn, K.J. McGuire, A. Piers*, and M. Traina

The DAMIC-M Collaboration deployed in October 2021 two 24 megapixel skipper CCDs (18 grams of silicon) in the Low Background Chamber (LBC) at the Modane Underground Laboratory (LSM) in France. The LBC is a test stand designed to evaluate the performance of skipper devices in a low-background environment deep underground. An analysis was performed on four data sets with a total exposure of 85 gram-days, which was selected after masking image regions of abnormally high dark counts (e.g., from lattice defects) and high-energy ionization events. A fit was performed to the distribution of pixels with charges between 0 and 7 electrons (e^-). The data are well described with a background model consisting of Gaussian pixel white noise with $\sigma_{\text{pix}} = 0.2 e^-$ and shot noise with mean occupancy per pixel between 10^{-3} and $10^{-2} e^-$, depending on data set. By including a signal from dark matter-electron scattering in the fit function, exclusion limits were derived on the dark matter-electron scattering cross-section $\bar{\sigma}_e$ assuming a single dark matter species in the galactic halo. The final results are shown in Fig. 5.5-1, which are the world's best exclusion limits on the existence of dark matter particles with MeV-scale masses. All details of the experiment are published¹.

*Presently at RKF Engineering, Bethesda, MD, 20814-6198.

¹DAMIC-M Collaboration, Phys. Rev. Lett. **130**, 171003 (2023).

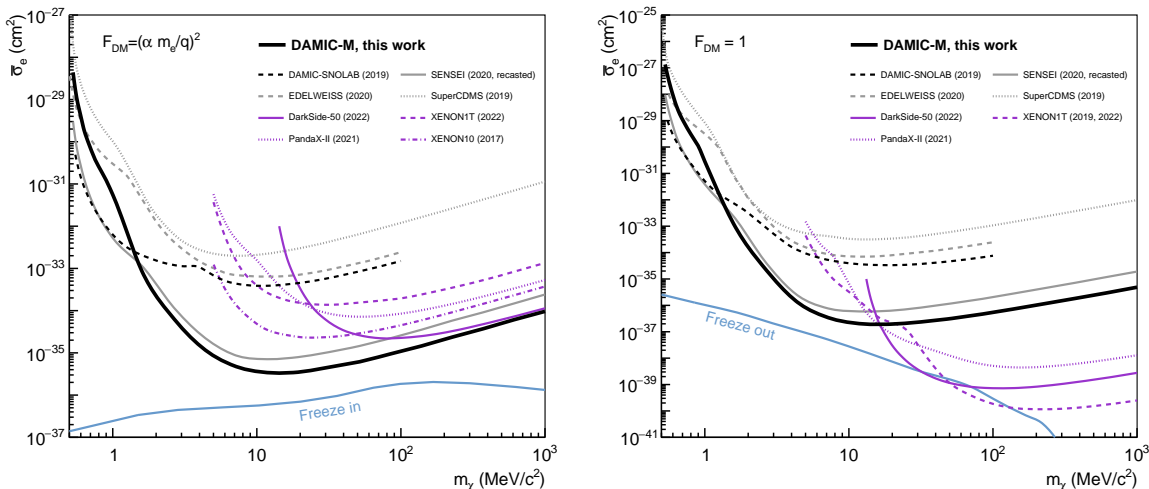


Figure 5.5-1. Exclusion limits on the dark matter-electron scattering cross section $\bar{\sigma}_e$ under the scenarios where the interaction occurs via an ultra-light (left) or heavy (right) hidden-photon mediator. The solid dark lines are the recent results from DAMIC-M¹.

5.6 Response of CCDs to surface events

A.E. Chavarria, K.J. McGuire, X. Ni, A. Piers*, and M. Traina

Particle interactions that occur within the first few microns from the back surface of a DAMIC CCD represent the dominant source of uncertainty in the CCD response, due to the presence of a micron-thick dead layer and a few microns-thick partial charge collection (PCC) region. A fraction of the ionization that originates in this region will undergo recombination, distorting the energy spectrum at low energies. Numerical simulations performed by the DAMIC Collaboration¹ show that the spectral shape of events at low energy vary significantly depending on the precise thickness and location of the PCC region relative to the CCD backside.

Using a test setup that allows for the controlled irradiation of the back and front surfaces of a CCD, Fig. 5.6-1, we have begun studying the effects of this PCC region on energy spectra and on dark count rates using radioactive sources to generate low-energy surface events. For example, we are using this setup to compare the performance of DAMIC CCDs to a new batch of CCDs that have undergone a back-thinning process to remove the PCC region. Later this year, we plan to install two of the new back-thinned CCDs in our cryochamber at SNOLAB for testing in a low-background environment.

This setup also allows us to validate our charge diffusion model, which relates the spread of a charge cluster in a CCD image (σ_{xy}) to the depth of the particle interaction in the

*Presently at RKF Engineering, Bethesda, MD, 20814-6198.

¹DAMIC Collaboration, Phys. Rev. D **105**, 062003 (2022).

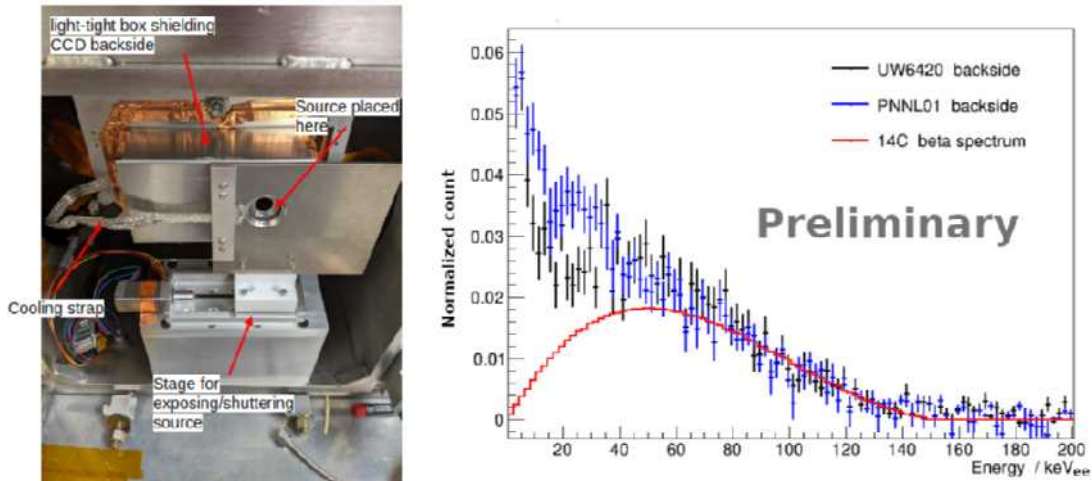


Figure 5.6-1. *Left*: Test setup for CCD surface calibration studies performed at UW. *Right*: Reconstructed energy spectra from irradiating the backside of two skipper CCDs with low-energy β rays from a ^{14}C source. UW6420 is a typical DAMIC CCD with PCC region. PNNL01 has undergone backside processing to remove the PCC region.

CCD. We use this model in dark matter searches to identify and reject surface events, which constitute a significant component of our background. In particular, we recently used a ^{14}C β source to explore the DAMIC at SNOLAB low-energy excess, observed in both the 2017-2019 WIMP search¹ and recently in the 2022 skipper CCD upgrade² (Sec. 5.4). By operating a skipper CCD in our PAB lab with the same parameters used in the SNOLAB skipper upgrade, we verified that the excess bulk events are unlikely to be surface events misclassified by our diffusion model, Fig. 5.6-2.

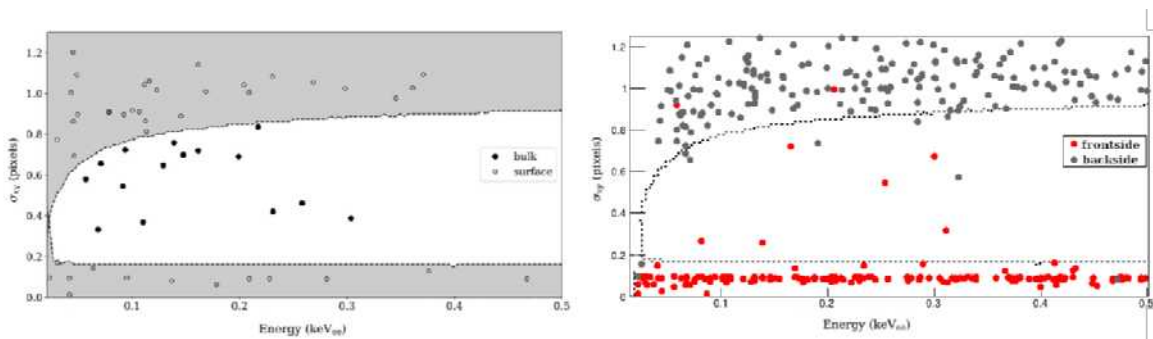


Figure 5.6-2. *Left*: Ionization events observed in the DAMIC at SNOLAB skipper upgrade that pass selection cuts, showing an excess of bulk events above known backgrounds. *Right*: Data obtained in our PAB surface lab using a CCD from the same batch and a ^{14}C source to generate low-energy surface events. The rate of surface events leaking into the bulk region is $\sim 4\%$, consistent with the expectation from our diffusion model.

¹DAMIC Collaboration, Phys. Rev. Lett. **125**, 241803 (2020).

²DAMIC Collaboration, arXiv:2306.01717 (2023).

5.7 Low-energy electronic recoils from Compton scattering in silicon

A.E. Chavarria and outside collaborators*

The minimum energy deposited in a target when a γ ray incoherently scatters off an atomic electron is the electron’s binding energy. Thus, when a target is exposed to a γ ray source, there are a series of “steps” in the electronic recoil spectrum at the binding energy of each of the atomic shells. These features have proven to be useful in the calibration of the energy response of detectors at low energies.

A first measurement was performed in 2017 by illuminating with γ rays a silicon charge-coupled device (CCD) with conventional readout from the DAMIC experiment¹. Spectral features corresponding to the atomic L_{2,3}, L₁ and K shells were observed at 0.10, 0.15 and 1.8 keV, respectively. The L-shell step was much softer than expected, and it was not clear whether this was caused by the response of the CCD.

The measurement was recently repeated at The University of Chicago with a skipper CCD², with significantly improved pixel noise of $\sigma_{\text{pix}} = 2.8$ eV compared to 7.0 eV of the first measurement. The CCD, front-end electronics, readout and control software were contributed by CENPA. The resulting spectrum (Fig. 5.7-1) confirms the previous measurement, with a clear softening of the L-step in the data (black) compared to the standard particle-physics simulation package Geant4 (purple). The red line shows the theoretical prediction performed at CENPA using the FEFF10 code³ from Prof. John Rehr’s group at the UW, which has previously shown to reproduce the correct nonresonant inelastic x-ray scattering (NRIXS) spectrum in silicon. Both the predicted Geant4 and FEFF10 spectra include our model of the energy response of the CCD. The FEFF10 result shows good agreement with the data, which suggests that the CCD response model is accurate down to the 23 eV threshold of the measurement, and that the simulation of atomic effects is inadequate in Geant4.

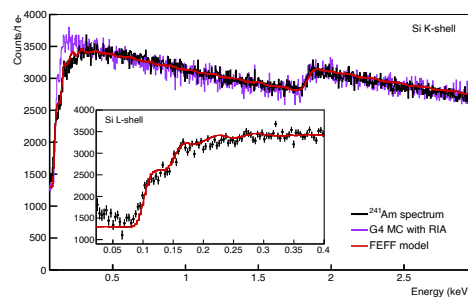


Figure 5.7-1. The measured ^{241}Am Compton spectrum (black) from the 23 eV detection threshold to 2.1 keV. The K-step is observed at 1.8 keV. The simulated spectra with Geant4 (purple) and FEFF10 (red) include the detector energy response. The inset shows the data comparison to the FEFF prediction in the L-shell energy range.

*DAMIC-M Collaboration

¹K. Ramanathan *et al.*, Phys. Rev. D **96**, 042002 (2017).

²DAMIC-M Collaboration, Phys. Rev. D **106**, 092001 (2022).

³J.J. Rehr *et al.*, The FEFF Project, <https://feff.phys.washington.edu/feffproject-portal.html> (2022).

6 Education

6.1 Use of CENPA facilities in education and coursework at UW

B. W. Dodson

CENPA continues to offer unique opportunities for students to become involved in a wide range of applied methods in modern physics experimentation. Undergraduate and graduate students contribute to a variety of experimental operations from design to data analysis both on site and in many of the international collaborations CENPA is involved in.

CENPA lab operations are conducted with strong consideration for best lab safety practice – all students receive specialized lab training mandated through UW’s Environmental Health & Safety (EH&S)¹ training programs. Access to the electronics shop, student machine shop, chemistry and a variety of other laboratory spaces gain students advantageous skills relevant in engineering and technical industries. CENPA also continues to offer a graduate-level laboratory course on nuclear physics with special interest in accelerators and radiation detection, PHYS 575/576 *Radiation: Sources, Detectors and Safety*(Sec. 6.2).

CENPA offers educational group tours to schools and organizations adapted for a range of grade levels to inspire interest in experimental physics. CENPA organized group tours for the 2023 Conference for Undergraduate Women in Physics² and hosted a table at the CUWiP career fair. Classes from other departments such as the Environmental and Occupational Health Sciences have toured CENPA facilities to learn about lab safety practices at a diverse research institution.



Figure 6.1-1. Conference for Undergraduate Women in Physics visits CENPA in 2023.

¹Environmental Health & Safety, <https://ehs.washington.edu/training>

² Conference for Undergraduate Women in Physics, <https://www.aps.org/programs/women/workshops/cuwip.cfm>

6.2 Accelerator-based lab class in nuclear physics

B. W. Dodson, A. García, and E. B. Smith

As part of UW physics evening master's program, CENPA hosts *PHYS576 Radiation: Sources, Detectors and Safety*¹. PHYS 576 offers uniquely immersive instruction in nuclear theory, research, and application in the local workforce. Emphases on relevant applied methods of nuclear physics experimentation supports professional development for students already working or interested in growing aerospace and technical industries. PHYS576 is offered every 18 months and continues to be a popular class. Weekly 90-minute laboratory sessions offer hours of hands-on experience with unique experimental equipment including the Van De Graff accelerator, associated ion sources, an array of particle detectors, nuclear instrumentation electronics, and data acquisition systems.



Figure 6.2-1. *Left:* Student tuning the Direct Extraction Ion Source during a lab. *Right:* Students use mass analyzing magnet to focus a beam of ions.

Supported by professional engineers, the following list of subjects are covered:

¹PHYS 576, Radiation: Sources, detectors, and Safety, <https://phys.washington.edu/courses/2022/spring/phys/576/b>

1. The atomic nucleus. Basic nuclear physics, nuclear energy, orders of magnitude.
2. Attenuation of photon radiation. Solid state detectors (Ge and Si).
3. Ranges of ions and electrons. The weak interaction. Radioactivity, radiation damage, and health risks (α , β , γ , and neutron activity).
4. Counting statistics.
5. Deciphering a mystery γ spectrum measured using a Ge solid-state detector. Gauging the level of radioactivity and assessing health risks.
6. 9 megavolt tandem accelerator operation, duoplasmatron ion source function, and ion beam optics. Tuning beam through our own tandem Van de Graaff accelerator.
7. Rutherford back-scattering (RBS) spectra, measured by scattering accelerated protons off of foil targets and into Si solid-state detectors. Deciphering a mystery spectrum to determine the material contents of a mystery foil (Fig. 6.2-2 *Left*).
8. Fission and fusion. Nuclear reactors, nuclear astrophysics (nucleosynthesis in stars).
9. Basics of the Shell Model. Approximate predictions using simple models, using quantum numbers, predicting decay rates.
10. Searching for new physics with ${}^6\text{He}$.
11. Nuclear Resonance. Resonance energy of ${}^{27}\text{Al}(p,\gamma){}^{28}\text{Si}$ nuclear reaction determined by irradiating an aluminum target with accelerated protons and detecting the resulting γ 's in a high purity germanium (HPGe) solid-state detector (Fig. 6.2-2 *Right*).
12. Tour of Seattle's Boeing accelerator facilities. A glimpse of accelerator science in the modern workforce.



Figure 6.2-2. *Left*: RBS setup indicating 2 MeV protons (orange) incident on a thin foil target yielding back-scattered protons (green) detected in Si solid-state detectors. *Right*: ${}^{27}\text{Al}(p,\gamma){}^{28}\text{Si}$ nuclear resonance setup indicating 1 MeV incident protons (orange) incident on Aluminum target yielding in resonance emission γ 's (green) detected in an HPGe solid-state detector.

7 Facilities

7.1 miniSciFi development for g-2

T. Burritt, C. Claessens, L. Dippel, P. Kammel, B. MacCoy, N. Miedema, and
R. Roehnelt

Hardware engineering for experimental physics is continual learning. A good example of this is the miniSciFi motion mechanism for the g-2 experiment. The initial description of the task was relatively simple: take this working two position fiber harp motion system and turn it into a mechanism that can sweep through the full range of motion. (That doesn't sound too difficult, right?) Then you get into the details. Conventional stepper motors are not allowed as the whole mechanism needs to be non-magnetic to not distort the g-2 magnetic field. So maybe pneumatic position control using aluminum and non-magnetic stainless cylinders? No, that's only good to about $\pm 0.25\text{mm}$, and better precision is needed.

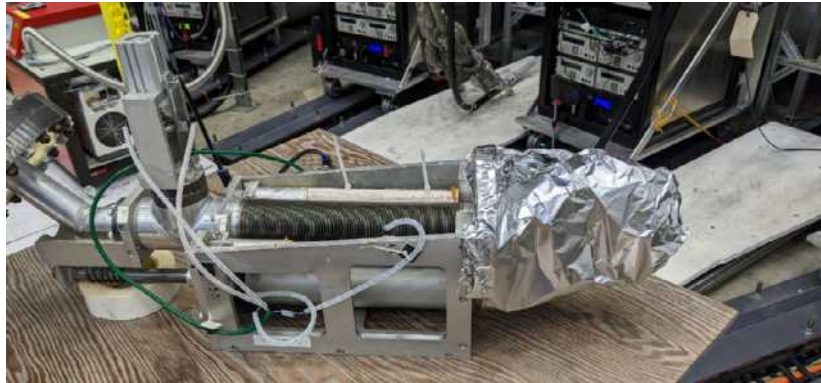


Figure 7.1-1. The initial mechanism given to engineering to modify.

After some consideration, the first attempt was to remove the pneumatic cylinder below the bellows and bolt on a lead screw to the back of the device. To keep this non-magnetic, the drive motor used was a rotary piezo motor, a spare from the g-2 trolley. To make sure the lead screw was non-magnetic a titanium $3/8'' - 40$ ACME thread lead screw was custom machined at UW. Initial testing showed it moved, but how much linear motion depended on nut position on the lead screw. So, maybe inadequate lubrication? We made sure to apply lots of grease. Still didn't work as well as needed and, worse, it started getting stuck.

Add in a gearbox with a 3.8:1 reduction. Things looked much better! Well, initially. After installation and use in the g-2 experiment, the performance slowly degraded. The friction got so high the motor had to be removed, and a manual wrench attached to the end of the lead screw, driven by a high torque non-magnetic human. Closer examination revealed the Titanium lead screw was shedding fiber like particles that were getting embedded in the plastic lead screw nut. For the short term fix, the plastic nut was replaced with another plastic nut. Temporary fix enabled, a longer term solution was researched.

Thinking the plastic nut could be breaking down and adding to the friction, it was replaced with a brass nut. However, the big find was Titanium has a high coefficient of friction. As the lead screw is on the back of the mechanism, farther away from the g-2 ring, it was decided to try a standard 300 series stainless lead screw and check if that would perturb the magnetic field too much. New parts installed, the mechanism was shipped back to Fermilab, installed and tested. The magnetic field perturbation was small, but the motion was only slightly better. So keep the standard lead screw, but more change was needed.



Figure 7.1-2. Piezo motor, gear box, brass ACME nut.

Going through the load path to the lead screw, there were two components: an axial load from the vacuum of the g-2 experiment and a torque load from the offset between the vacuum center of force and the lead screw axis. The torque on the lead screw was mitigated by design, allowing only force transmission to the lead screw. However, the torque on the guide rods could not be similarly mitigated. So how to balance the vacuum force? The first suggestion of attaching Lead weights to the back of the motion mechanism with a rope and pulleys was dismissed as too difficult to get past the safety inspection at a national research lab. Then we recalled we had this left over non-magnetic pneumatic cylinder from the original mechanism. Of course! All we needed to do was mount that inline with the motion axis, eliminating the torque, and regulate the gas pressure to mostly offset the force from the vacuum. A completely obvious solution in retrospect. Preliminary testing showed promise.

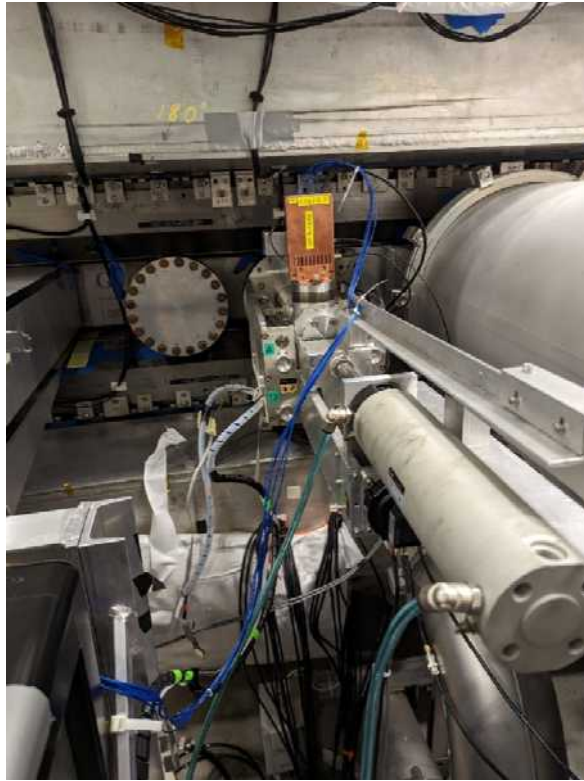


Figure 7.1-3. miniSciFi installed at g-2 in final configuration.

Installation of the g-2 ring went smoothly, pressure was adjusted, and the mechanism was reported as being so reliable it had become boring. In a normal motion application, sweeping from one end of the travel to the other would have been simple, buy a lead screw and an appropriately sized motor. The unique constraint of using non-magnetic components and the desire to keep the motion system as simple as possible created an initial design that was not adequate to the task. As the design space was explored, the design improved with additional knowledge. Complexity was also added as it was seen to be needed.

7.2 Instrument Shop

N. Miedema

The CENPA Instrument shop is manned by highly skilled instrument makers with decades of experience working in the research environment. With the help of our engineering team, the shop fabricates ultrahigh vacuum systems, cryogenic components, equipment operating in high magnetic fields, and mechanical devices for high and low voltage applications, hydraulics and gas handling systems. Tom Burritt, before his retirement in June, assisted faculty, staff and students, gave advice and suggestions and made sure what they wanted was feasible and cost effective. Nate Miedema is the primary CNC operator, welder and trainer of students in the student shop. Together we solve mechanical problems and give CENPA the ability to

be a leading force in Physics. In addition to supporting CENPA we also machine parts for other groups at the University and have helped with an experiment taking place at Western Washington University. Some notable fabrications are shown in the images below.

ADMX



5pt)

Figure 7.2-1. *Left:* Gold-plated attenuator mounting block. *Right:* Heat sinks made from OFHC copper, copper braid and silver solder.

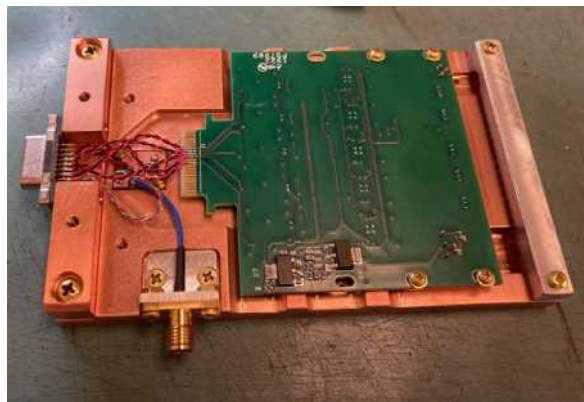


Figure 7.2-2. Electronics box heat sink, made from copper.

Project 8

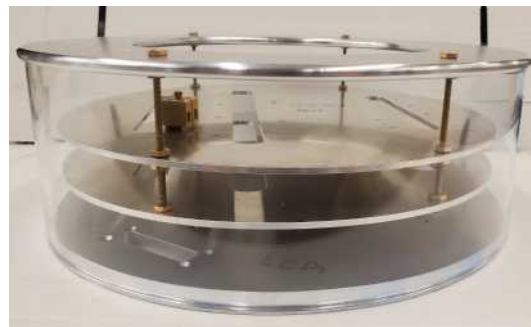


Figure 7.2-3. *Top left:* 4-to-1 CF flange with vacuum-tight welds, inner View *Top right:* 4 to 1 CF flange, outer view *Bottom left:* 2mm Tungsten ball *Bottom right:* LED ring with aluminum rings and acrylic body.

PIONEER



Figure 7.2-4. Acrylic light guides, polished to an optical finish.

DAMIC-M

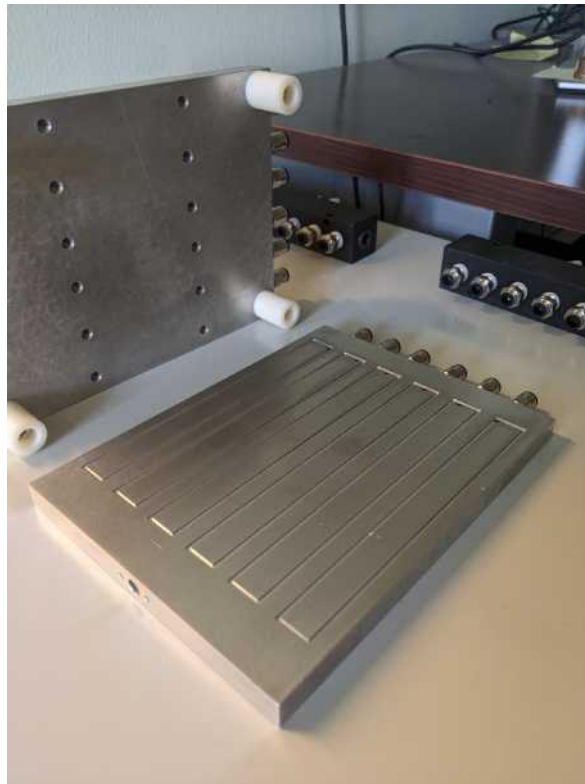


Figure 7.2-5. Heated vacuum chuck made from aluminum.

Western Washington University



Figure 7.2-6. Liquid nitrogen reservoir for ultrahigh vacuum chamber.

Miscellaneous

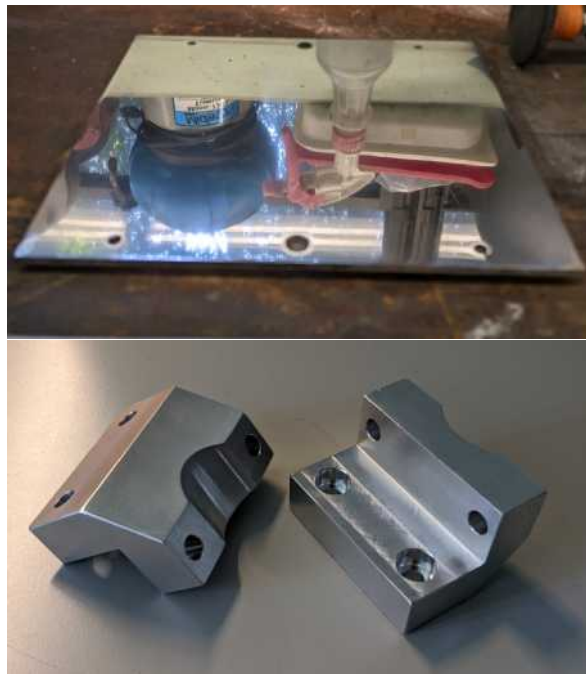


Figure 7.2-7. *Top*: Aluminum plate polished to a mirror finish *Bottom*: Motor brackets made of 316 stainless steel.

7.3 CENPA electronic shop

D. A. Peterson and T. D. Van Wechel

The electronics shop is responsible for the design and construction of new laboratory electronic equipment as well as the maintenance and repair of existing CENPA electronics. Projects undertaken by the electronics shop in the past year include the following:



Figure 7.3-1. Typical cable assembly. Several adapter boards and cable harnesses were made for the DAMIC-M and Selena projects.



Figure 7.3-2. Constructed 15 channels of single ended to differential converters for the Pioneer project.



Figure 7.3-3. Designed and built a new faster five channel amplifier for the $g - 2$ MiniSciFi fiber harp.

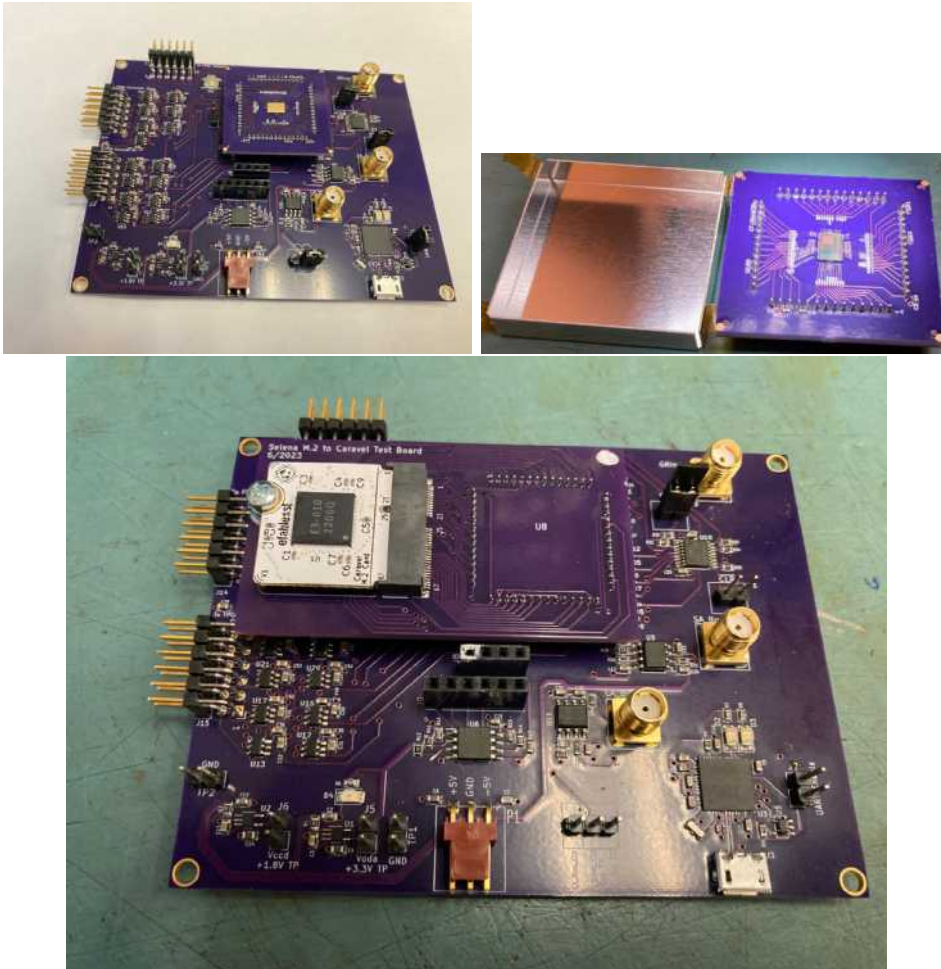


Figure 7.3-4. Caravel ASIC test board for the Selena project. The board accommodates a Caravel die or M.2 carrier.

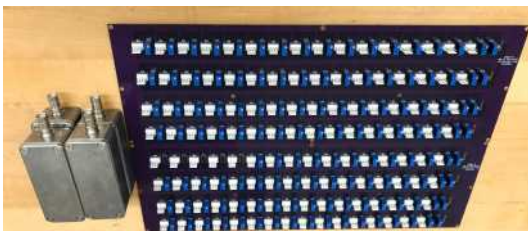


Figure 7.3-5. COHERENT Photomultiplier tube (PMT) voltage divider.

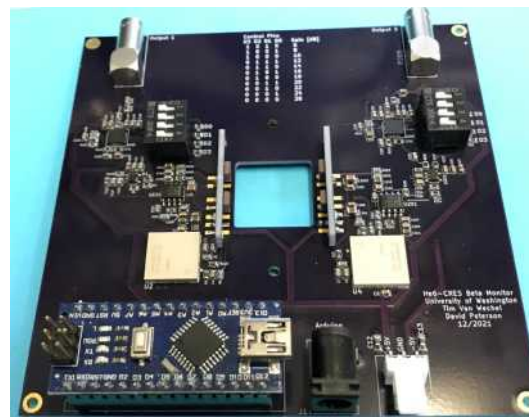


Figure 7.3-6. Designed and built a beta radiation monitor for He6-CRES.

7.4 Operation of the cenpa-rocks computer cluster

G. Holman

We continue to operate the cenpa-rocks Linux cluster as a computing resource for CENPA. This is a heterogeneous cluster consisting of roughly 130 nodes. These compute nodes are DELL Power Edge R410 blades of three types: one with 12 cores and 48 GB of memory per node, one with eight cores and 24 GB of memory per node and one with eight cores and 16 GB of memory per node. The cluster is managed with rocks cluster software¹. Users connect to a login node and interact with the compute nodes using Sun Grid Engine (SGE). In addition to the compute nodes, we have significant data storage in three large raid systems offering a total of 175 TB of storage. The raid systems are connected to DELL Power Connect 6248 switches with paired 10 Gb/s fiber connections, and the switches are connected to the compute nodes via 1 Gb/s ethernet. There are also hard drives distributed throughout the compute nodes managed as a single 40 TB filesystem using XRootD.

We have been able to operate the cluster inexpensively by relying on the infrastructure (and some of the compute nodes) left from the previous Athena cluster, which was installed in 2009. This infrastructure includes the power and power distribution, the cooling and the racks and physical setup. Two years ago, we reported on augmenting our compute nodes with nodes surplussed from NERSC². These nodes and our original Athena nodes are all over ten years old, and over the past year a number of them have gone offline. We acquired 150 Dell R620 servers from the generous donation by Bryce Livingston at The Institute for Health Metrics and Evaluation (IHME). These were acquired through an inventory transfer UW form 1024. Lastly, Some of the Power Connect switches are showing signs of age. We plan to replace these with refurbished units at less than \$200 each or upgrade the backplane to 10GBE.

At over 1000 cores and significant data storage, cenpa-rocks offers a powerful computing platform at very low cost. As much of the infrastructure is quite old, there are a number of possible failure points. Among these are the switches, power strips and cooling fans. These can be replaced at low cost. We expect to be able to maintain and, with new nodes obtained from surplus, enhance the cenpa-rocks cluster as a computing resource for CENPA over the next year and hopefully beyond.

¹<https://www.rocksclusters.org/>

²CENPA Annual Report, University of Washington (2019) p. 161.

7.5 Van de Graaff accelerator and ion-source operations and development

Y. Chowdhury, A. Chu, B. W. Dodson, K. Hansen, A. McKeirnan, D. A. Peterson, E. B. Smith, and T. D. Van Wechel

Since the previous Annual Report we saw an increase in tandem accelerator and direct extraction ion source (DEIS) demand. The tandem accelerator was vented 5 times for repairs.

An entry was made due to observed column sparking resulting in replacement of damaged column resistor jumpers and some associated jumper jacks for column 1 resistors #81-#82 and #83-#84, column 2 #153-#154, and column 4 #61-#62.

Two ventings, both without entry, were necessary to replace all of the viewport flange gaskets, view glass and flange port, on the top of the tandem tank, which included re-machining the farthest west flange to properly secure the view glass gasket.

A failure of the corona fixture gate valve gasket that makes contact with the tandem corona port hole flange required a third venting without entry, during which the entire corona fixture (corona assembly, gate valve, mounting extension ring) was removed. Gaskets were cut from new rubber material and installed for the three round flange gaskets and for the rectangular gate valve bonnet gasket.

A final entry was made to address the unchangeable VERT steerer voltage, erroneous and random foil counter number incrementing (actual foil mechanism not incrementing, just the counter), and high pitch chain noise. Marginal fiber optic communications transmission was localized to the Low Energy (LE) bulkhead fiber optic feedthrough filaments, which appeared to have micro-cracks and glue "crazing". Fabrication and installation of a new fiber optic feedthrough still using epoxy for potting, but properly crimping the fiber optic connectors instead of using glue, resulted in a good fiber optic communication that restored the VERT steerer control and eliminated the erroneous foil counter number incrementing. Tension springs were installed on the VERT steerer variac motor mount screws reducing motion binding caused by motor and variac shaft mis-alignments, and matching springs installed previously on the HORIZ variac motor mounting.

During this reporting period from April 1, 2021, to March 31, 2023, the tandem pelletron chains operated 427 hours, the sputter-ion-source (SpIS) operated 0 hours, and the duoplasmatron direct-extraction-ion source (DEIS) operated 673 hours. Tandem accelerator produced ion beams originated from the DEIS, and were 12 MeV $^1\text{H}^+$ for the ^6He -CRES ^{19}Ne experiment and 17.8 MeV $^2\text{H}^+$ for the ^6He -CRES ^6He experiment.

ACTIVITY SCHEDULED	DAYS SCHEDULED	PERCENT of TIME
Nuclear-physics research, accelerator	25	3.4

Table 7.5-1. Tandem Accelerator Operations April 1, 2021, to March 31, 2023.

8 CENPA Personnel

8.1 Faculty

Eric G. Adelberger ¹	Professor Emeritus
Alvaro Chavarria	Assistant Professor
Jason Detwiler	Professor
Peter J. Doe ²	Research Professor
Sanshiro Enomoto	Research Professor
Alejandro García	Professor
Jens H. Gundlach ¹	Professor
David W. Hertzog	Professor; Director
Peter Kammel	Research Professor
Elise Novitski	Research Assistant Professor
R. G. Hamish Robertson	Professor Emeritus
Leslie J Rosenberg ¹	Professor Emeritus
Gray Rybka	Associate Professor
Derek W. Storm ¹	Research Professor Emeritus

8.2 Postdoctoral Research Associates

Svende Braun	Muon $g - 2$ / PIONEER
Nicholas Buzinsky	He-6 CRES
Christine Claessens	Project 8 / Muon $g - 2$
Conner Gettings ¹	Gravity
Zachary Hodge ³	Muon $g - 2$
Heng Lin ⁴	DAMIC-M / Selena
Brynn MacCoy ⁵	Muon $g - 2$ / PIONEER
Alexander Marsteller	KATRIN / Project 8
Emily Miller ⁶	LEGEND / Project 8
Michael Ross ¹	Gravity
Patrick Schwendimann	Muon $g - 2$ / PIONEER
Michaelangelo Traina ⁷	DAMIC / Selena
Louis Varriano	LEGEND
Clint Wiseman	LEGEND
Dan Zhang ¹	ADMX

¹Not supported by DOE CENPA grant.

²Retired July 2023.

³Departed February 2023.

⁴Arrived May 2023.

⁵Graduated July 2023. Started Postdoc Appt. July 1, 2023.

⁶Arrived June 2023.

⁷Arrived January 2023.

8.3 Predoctoral Research Associates

Shoshana Apple ¹	Gravity
Omar Beesley	Pioneer
Sam Borden	LEGEND
Jackson Busch ¹	DAMIC
Thomas Braine ¹	ADMX
William (Drew) Byron	He-6 CRES
Sabrina Cheng	LEGEND
Madison Durand	COHERENT
Michaela Guzzetti ¹	ADMX
Heather Harrington	He-6 CRES
Alexandru Hostiuc	MAJORANA
Joshua La Bounty	Muon $g - 2$
Kellie McGuire ¹	DAMIC
Ethan Muldoon ²	MuSun
Christian Nave	LEGEND
Xiaochen Ni ¹	Selena
Alexander Piers ^{1,3}	DAMIC
Nicholas Ruof ³	MAJORANA / LEGEND
Erik Shaw ^{1,4}	Gravity
Grace Song	LEGEND
Meg Wynne	Project 8

¹Not supported by DOE CENPA grant.

²Graduated May, 2023.

³Graduated March, 2023.

⁴Graduated June, 2023.

8.4 Professional staff

Tom H. Burritt ¹	RS/Engr Sr	Precision design, machining
Marcel Conde ²	RS/E2	DAMIC fabrication & Jr. Engineer
Brittney Dodson	RS/E2	Jr. Engineer, ADMX safety officer
Cyrus Goodman	RS/E2	ADMX liquification operator
Charles Hanretty	RS/E3	ADMX engineer project manager
Gary T. Holman	Associate Director	Computer systems
Michael Huehn	RS/E2	Jr. Engineer, Project 8, DAMIC
Matthew Kallander	RS/E1	Jr. Engineer, Project 8
Duncan J Prindle ³	RS/E4	MuSun research, Cluster admin
Ryan Roehmelt	RS/E4	Sr. Mechanical Engineer
Eric B. Smith ⁴	RS/E3	Accelerator, ion sources
H. Erik Swanson	RS/Engr Sr	Precision experimental equipment
Timothy Van Wechel	RS/E4	Analog and digital electronics design

8.5 Technical staff

Nate Miedema ⁵	Instrument Maker
David A. Peterson	Electronics Technician

8.6 Administrative staff

Katherine Nishihama ⁶	Fiscal Specialist 2
Kyle Fitzsimmons	Fiscal Specialist 2

¹Retired June, 2023.

²Not supported by DOE CENPA grant.

³Retired March, 2023.

⁴Departed for Sandia National Lab, NM in October, 2023.

⁵Arrived May, 2022.

⁶Arrived July, 2022.

9 Publications

Published papers

1. Hong, R. *et al.* Systematic and statistical uncertainties of the Hilbert-transform based high-precision FID frequency extraction method. *Journal of Magnetic Resonance* **329**, 107020. ISSN: 1090-7807.
<https://www.sciencedirect.com/science/article/pii/S1090780721001099> (2021). DOE Supported.
2. Kamil, M. *et al.* Isospin mixing and the cubic isobaric multiplet mass equation in the lowest $T = 2$, $A = 32$ quintet. *Phys. Rev. C* **104**, L061303.
<https://link.aps.org/doi/10.1103/PhysRevC.104.L061303> (6 2021). DOE Supported.
3. Müller, P. *et al.* β -Nuclear-Recoil Correlation from ${}^6\text{He}$ Decay in a Laser Trap. *Phys. Rev. Lett.* **129**, 182502.
<https://link.aps.org/doi/10.1103/PhysRevLett.129.182502> (18 2022). DOE Supported.
4. Byron, W. *et al.* First observation of cyclotron radiation from MeV-scale e^\pm following nuclear β decay. *Phys. Rev. Lett.* <https://journals.aps.org/prl/accepted/04079Y86Jbb1ab73011e1c32d5da2feec6545cc26> (2023). DOE Supported.
5. Cervantes, R. *et al.* Search for 70 μeV Dark Photon Dark Matter with a Dielectrically Loaded Multiwavelength Microwave Cavity. *Phys. Rev. Lett.* **129**, 201301.
<https://doi.org/10.1103/PhysRevLett.129.201301> (20 2022). DOE Supported.
6. Cervantes, R. *et al.* ADMX-Orpheus first search for 70 μeV dark photon dark matter: Detailed design, operations, and analysis. *Phys. Rev. D* **106**, 102002.
<https://doi.org/10.1103/PhysRevD.106.102002> (10 2022). DOE Supported.
7. Arnquist, I. *et al.* First Constraints from DAMIC-M on Sub-GeV Dark-Matter Particles Interacting with Electrons. *Phys. Rev. Lett.* **130**, 171003. arXiv: 2302.02372 [hep-ex] (2023).
8. Norcini, D. *et al.* Precision measurement of Compton scattering in silicon with a skipper CCD for dark matter detection. *Phys. Rev. D* **106**, 092001. arXiv: 2207.00809 [physics.ins-det] (2022).
9. Adari, P. *et al.* EXCESS workshop: Descriptions of rising low-energy spectra. *SciPost Phys. Proc.* **9** (eds Fuss, A., Kaznacheeva, M., Reindl, F. & Wagner, F.) 001. arXiv: 2202.05097 [astro-ph.IM] (2022).
10. Aker, M. *et al.* New Constraint on the Local Relic Neutrino Background Overdensity with the First KATRIN Data Runs. *Physical Review Letters* **129**, 011806 (June 2022). DOE Supported.
11. Aker, M. *et al.* Direct neutrino-mass measurement with sub-electronvolt sensitivity. *Nature Physics* **18**, 160–166 (Feb. 2022). DOE Supported.

12. Aker, M. *et al.* Improved eV-scale sterile-neutrino constraints from the second KATRIN measurement campaign. *Physical Review D* **105**, 072004 (Apr. 2022). DOE Supported.
13. Aker, M. *et al.* KATRIN: status and prospects for the neutrino mass and beyond. *Journal of Physics G: Nuclear and Particle Physics* **49**, 100501 (Sept. 2022). DOE Supported.
14. Marsteller, A. *et al.* Operation modes of the KATRIN experiment Tritium Loop System using $^{83\text{m}}\text{Kr}$. *Journal of Instrumentation* **17**, P12010 (Dec. 2022). DOE Supported.
15. Aker, M. *et al.* Search for Lorentz-invariance violation with the first KATRIN data. *Physical Review D* **107**, 082005 (Apr. 2023). DOE Supported.
16. Gauda, K. *et al.* An active transverse energy filter to differentiate low energy particles with large pitch angles in a strong magnetic field. *The European Physical Journal C* **82** (Oct. 2022). DOE Supported.
17. Lokhov, A. *et al.* Probing the Neutrino-Mass Scale with the KATRIN Experiment. *Annual Review of Nuclear and Particle Science* **72**, 259–282 (Sept. 2022).
18. Hillesheimer, D. *et al.* Four Years of Tritium Operation of the KATRIN Experiment at TLK. *Fusion Science and Technology*, 1–7 (June 2023). DOE Supported.
20. Arnquist, I. J. *et al.* Search for Spontaneous Radiation from Wave Function Collapse in the Majorana Demonstrator. *Phys. Rev. Lett.* **129**, 080401. arXiv: 2202.01343 [nucl-ex] (2022). DOE Supported.
21. Abe, S. *et al.* A Search for Correlated Low-energy Electron Antineutrinos in KamLAND with Gamma-Ray Bursts. *Astrophys. J.* **927**, 69. arXiv: 2112.04918 [astro-ph.HE] (2022).
22. Akimov, D. *et al.* Monitoring the SNS basement neutron background with the MARS detector. *JINST* **17**, P03021. arXiv: 2112.02768 [physics.ins-det] (2022).
23. Abgrall, N. *et al.* The Majorana Demonstrator readout electronics system. *JINST* **17**, T05003. arXiv: 2111.09351 [physics.ins-det] (2022). DOE Supported.
24. Akimov, D. *et al.* Measurement of scintillation response of CsI[Na] to low-energy nuclear recoils by COHERENT. *JINST* **17**, P10034. arXiv: 2111.02477 [physics.ins-det] (2022).
25. Arnquist, I. J. *et al.* Signatures of muonic activation in the Majorana Demonstrator. *Phys. Rev. C* **105**, 014617. arXiv: 2110.14796 [nucl-ex] (2022). DOE Supported.
26. Akimov, D. *et al.* First Probe of Sub-GeV Dark Matter beyond the Cosmological Expectation with the COHERENT CsI Detector at the SNS. *Phys. Rev. Lett.* **130**, 051803. arXiv: 2110.11453 [hep-ex] (2023).
27. Akimov, D. *et al.* Measurement of the Coherent Elastic Neutrino-Nucleus Scattering Cross Section on CsI by COHERENT. *Phys. Rev. Lett.* **129**, 081801. arXiv: 2110.07730 [hep-ex] (2022).

28. Akimov, D. *et al.* Simulating the neutrino flux from the Spallation Neutron Source for the COHERENT experiment. *Phys. Rev. D* **106**, 032003. arXiv: 2109.11049 [hep-ex] (2022).
29. Abe, S. *et al.* Limits on Astrophysical Antineutrinos with the KamLAND Experiment. *Astrophys. J.* **925**, 14. arXiv: 2108.08527 [astro-ph.HE] (2022).
30. Abe, S. *et al.* Search for Solar Flare Neutrinos with the KamLAND Detector. *Astrophys. J.* **924**, 103. arXiv: 2105.02458 [astro-ph.SR] (2022).
31. Arnquist, I. J. *et al.* α -event characterization and rejection in point-contact HPGe detectors. *Eur. Phys. J. C* **82**, 226. arXiv: 2006.13179 [physics.ins-det] (2022). DOE Supported.
32. Elliott, S. *et al.* Variable energy X-ray fluorescence source. *Journal of Instrumentation* **18**, P01004 (2023).
33. Abe, S. *et al.* KamLAND's search for correlated low-energy electron antineutrinos with astrophysical neutrinos from IceCube. *Astropart. Phys.* **143**, 102758. arXiv: 2202.07345 [astro-ph.HE] (2022).
34. Abe, S. *et al.* Search for the Majorana Nature of Neutrinos in the Inverted Mass Ordering Region with KamLAND-Zen. *Phys. Rev. Lett.* **130**, 051801. arXiv: 2203.02139 [hep-ex] (2023).
35. Arnquist, I. J. *et al.* Experimental study of $C13(\alpha,n)O16$ reactions in the Majorana Demonstrator calibration data. *Phys. Rev. C* **105**, 064610. arXiv: 2203.14228 [nucl-ex] (2022). DOE Supported.
36. Arnquist, I. J. *et al.* Search for Solar Axions via Axion-Photon Coupling with the Majorana Demonstrator. *Phys. Rev. Lett.* **129**, 081803. arXiv: 2206.05789 [nucl-ex] (2022). DOE Supported.
37. Abe, S. *et al.* Abundances of uranium and thorium elements in Earth estimated by geoneutrino spectroscopy. *Geophys. Res. Lett.* **49**, e99566. arXiv: 2205.14934 [physics.geo-ph] (Aug. 2022).
38. Akimov, D. Y. *et al.* COHERENT constraint on leptophobic dark matter using CsI data. *Phys. Rev. D* **106**, 052004. arXiv: 2205.12414 [hep-ex] (2022).
40. Abe, S. *et al.* First measurement of the strange axial coupling constant using neutral-current quasielastic interactions of atmospheric neutrinos at KamLAND. *Phys. Rev. D* **107**, 072006. arXiv: 2211.13911 [hep-ex] (2023).
41. Detwiler, J. A. & Robertson, R. G. H. Shake-up and shake-off effects in neutrinoless double- β decay. *Phys. Rev. C* **107**, L042501. arXiv: 2210.08722 [nucl-ex] (2023).
42. Arnquist, I. J. *et al.* Charge trapping correction and energy performance of the Majorana Demonstrator. *Phys. Rev. C* **107**, 045503. arXiv: 2208.03424 [physics.ins-det] (2023). DOE Supported.
43. Arnquist, I. J. *et al.* Interpretable boosted-decision-tree analysis for the Majorana Demonstrator. *Phys. Rev. C* **107**, 014321. arXiv: 2207.10710 [physics.data-an] (2023). DOE Supported.

44. Arnquist, I. J. *et al.* Final Result of the Majorana Demonstrator's Search for Neutrinoless Double- β Decay in Ge76. *Phys. Rev. Lett.* **130**, 062501. arXiv: 2207.07638 [nucl-ex] (2023). DOE Supported.

Papers submitted or to be published

45. Nitta, T. *et al.* Search for a dark-matter induced Cosmic Axion Background with ADMX. *Phys. Rev. Letters* **N/A**, N/A. N/A (N/A N/A). DOE Supported.
46. Bartram, C. *et al.* Dark Matter Axion Search Using a Josephson Traveling Wave Parametric Amplifier. *Phys. Rev. Letters* **N/A**, N/A. N/A (N/A N/A). DOE Supported.
47. Aker, M. *et al.* Search for keV-scale Sterile Neutrinos with first KATRIN Data 2022. DOE Supported.
48. Wydra, J. *et al.* Viscosity measurements of gaseous H_2 between 200 K to 300 K with a spinning rotor gauge 2022.
49. Wydra, J. *et al.* ViMA – the spinning rotor gauge to measure the viscosity of tritium between 77 and 300 K 2022.
52. Abe, S. *et al.* Measurement of cosmic-ray muon spallation products in a xenon-loaded liquid scintillator with KamLAND. arXiv: 2301.09307 [hep-ex] (Jan. 2023).
53. An, P. *et al.* Measurement of $^{nat}\text{Pb}(\nu_e, Xn)$ production with a stopped-pion neutrino source. arXiv: 2212.11295 [hep-ex] (Dec. 2022).
54. Arnquist, I. J. *et al.* Exotic dark matter search with the Majorana Demonstrator. arXiv: 2206.10638 [hep-ex] (June 2022). DOE Supported.
55. Arnquist, I. J. *et al.* Search for charge nonconservation and Pauli exclusion principle violation with the Majorana Demonstrator. arXiv: 2203.02033 [nucl-ex] (Mar. 2022). DOE Supported.
56. Agostini, M. *et al.* Toward the discovery of matter creation with neutrinoless double-beta decay. arXiv: 2202.01787 [hep-ex] (Feb. 2022).

Invited talks

57. Garcia, A. Beta decay of ^{32}Ar WISArD Meeting, Caen, France, presented virtually. 2021. DOE Supported.
58. Graner, B. Precision Nuclear Physics with Microwaves: the He6-CRES experiment National Postdoctoral Seminar Series: Previews of the Future in Low-Energy Experimental Nuclear Physics, presented virtually. 2021. DOE Supported.
59. Garcia, A. Microwaves for nuclear spectroscopy Matter's Origin from Radioactivity Workshop, Jyväskylä, Finland, presented virtually. 2022. DOE Supported.
60. Garcia, A. The ^8B neutrino spectrum from the Sun Solar Fusion Cross Sections III Conference at Berkeley, CA. 2022. DOE Supported.

61. Harrington, H. *Searching for Chirality Flipping Interactions via Microwaves* 14th Conference on the Intersections of Particle and Nuclear Physics. 2022. DOE Supported.
62. Byron, W. *He6-CRES: Experimental Overview and Recent Progress* Fall 2022 Meeting of the APS Division of Nuclear Physics at New Orleans, LA. 2022. DOE Supported.
63. Chavarria, A. E. *Even Lighter Particle Dark Matter* Invited talk, 14th International Conference on Identification of Dark Matter (IDM 2022), Vienna, Austria. 2022.
64. Chavarria, A. E. *Searching for Light Dark Matter with DAMIC DAMIC-M* Invited talk, GUINEAPIG Workshop on Light Dark Matter, TRIUMF, Vancouver, Canada. 2022.
65. Chavarria, A. E. *The search for dark matter with DAMIC and DAMIC-M* Invited talk, Lake Louise Winter Institute 2023, Lake Louise, Canada. 2023.
66. Chavarria, A. E. *Dark matter search results from DAMIC-M* Invited talk, Rencontres de Moriond Electroweak Interactions Unified Theories, La Thuile, Italy. 2023.
67. Detwiler, J. A. *Searching for the Creation of Matter (Without Antimatter) in the Laboratory* Physics Colloquium, Brookhaven National Laboratory, Upton, NY. 2023.
68. Detwiler, J. A. & Gruszko, J. *What's the Matter with Neutrinos?* SURF Deep Talk, Sanford Underground Research Facility Visitor's Center, Lead, SD. 2023.
69. Detwiler, J. A. *Searching for the Creation of Matter (Without Antimatter) in MAJORANA and LEGEND* Nuclear Physics Seminar, University of California Los Angeles, Los Angeles, CA. 2023.
70. Detwiler, J. A. *Creating Matter (Without Antimatter) in the Laboratory* Physics Department Colloquium, University of Washington, Seattle, WA. 2022.
71. Detwiler, J. A. *Double-Beta Decay and Neutrino Mass* Seattle Snowmass Summer Meeting 2022, University of Washington, Seattle, WA. 2022.
72. Detwiler, J. A. *Report from the US: Double Beta Decay* UGAP 2022, Noda, Chiba, Japan. 2022.
73. Nave, C. J. *Supernova Neutrinos in LEGEND-1000* Workshop on Neutrino Interaction Measurements for Supernova Neutrino Detection, Oak Ridge National Lab, Oak Ridge, TN. 2023.
74. Wiseman, C. *Exotic dark matter search with the MAJORANA DEMONSTRATOR* Neutrinos and Dark Matter (NDM) 2022, Asheville, NC. 2023.
75. Wiseman, C. *The broad physics program of the MAJORANA DEMONSTRATOR at SURF: Final results and new directions* Sanford Underground Research Facility, Lead, SD. 2023.
76. Wiseman, C. *Searching for Matter Creation* PHYS 576 guest lecture. 2022.

Abstracts and contributed talks

77. Byron, H. *An Introduction to the He6-CRES Experiment* Contributed talk, APS-DNP meeting, virtual. 2021.

78. Harrington, H. *Report of First Data from the He6-CRES Experiment and Future Outlook* Contributed talk, APS-DNP meeting, virtual. 2021.
79. Graner, B. *Recent improvements to the He6-CRES apparatus, data acquisition system, and analysis methods* Contributed talk, APS-DNP meeting, virtual. 2021.
80. Taylor, R. J. *$E \times B$ trap emptying design and simulations for the He6-CRES* Contributed talk, APS-DNP meeting, virtual. 2021.
81. Taylor, R. J. *He6-CRES: How to interpret the cyclotron radiation of betas in the He6-CRES waveguide* Contributed talk, APS-DNP meeting, NOLA. 2022.
82. McClain, D. *Toward the Future: Upgrading the He6-CRES Experiment with an Ion Trap* Contributed talk, APS-DNP meeting, NOLA. 2022.
83. Guzzetti, M. *ADMX Run 1C Design and Status* Contributed talk, APS April Meeting, New York, NY. 2022. DOE Supported.
84. Sinnis, J. *ADMX Orpheus - first results and future operations* Contributed talk, APS April Meeting, New York, NY. 2022. DOE Supported.
85. Braine, T. *Superconducting Cavity Development for ADMX* Contributed talk, APS April Meeting, New York, NY. 2022. DOE Supported.
86. Braine, T. *Superconducting Radio Frequency (SRF) Cavities for the Axion Dark Matter eXperiment (ADMX)* Contributed talk, Applied Superconductivity Conference, Honolulu, HI. 2022.
87. Braine, T. *An overview of the Axion Dark Matter eXperiment* Contributed talk, Lake Louise Winter Institute, Lake Louise, Alberta Canada. 2022.
88. Guzzetti, M. *ADMX Run 1C Extended Receiver Noise Calibration* Contributed talk, APS April Meeting, Minneapolis, MN. 2023. DOE Supported.
89. Sinnis, J. *Design and development of high-frequency resonant structures for future axion searches* Contributed talk, APS April Meeting, Minneapolis, MN. 2023. DOE Supported.
90. Braine, T. *Superconducting Cavity Development for ADMX* Contributed talk, APS April Meeting, Minneapolis, MN. 2023.
91. Zhang, D. *Run 1C Extended Preliminary Results* Contributed talk, APS April Meeting, Minneapolis, MN. 2023. DOE Supported.
92. Zhang, D. *An overview of Axion Dark Matter eXperiment: current status and future plans* Contributed talk, UCLA Dark Matter 2023, Los Angeles, CA. 2023. DOE Supported.
93. Chavarria, A. E. *The low-energy spectrum in DAMIC at SNOLAB* Contributed talk, 14th International Conference on Identification of Dark Matter (IDM 2022), Vienna, Austria. 2022.
94. Piers, A. *DAMIC at SNOLAB Results* Contributed talk, 7th Symposium on Neutrinos and Dark Matter in Nuclear Physics, Asheville, NC. 2022.
95. McGuire, K. J. *Status of the DAMIC-M dark matter experiment* Contributed talk, APS April Meeting, Minneapolis, MN. 2023.

96. Marsteller, A. *KATRIN Status Update* Contributed talk, APS-DNP meeting, New Orleans, LA. Oct. 2022. DOE Supported.
97. Robertson, R. G. H. *Project 8: a new approach to measuring neutrino mass* Contributed talk, APS-DNP meeting, Pittsburgh, PA. Oct. 2017.
98. Wiseman, C. *Exotic dark matter search with the MAJORANA DEMONSTRATOR* Conference on the Intersections of Particle and Nuclear Physics (CIPANP), Lake Buena Vista, FL. 2022.
99. Wiseman, C. *Exotic dark matter search with the MAJORANA DEMONSTRATOR* APS Division of Nuclear Physics meeting (DNP), New Orleans, LA. 2022.
100. Wiseman, C. *Testing principles of quantum mechanics with low-background germanium detectors* CENPA Seminar for Art McDonald. 2022.
101. Wiseman, C. *New limits on the sterile neutrino transition magnetic moment from the MAJORANA DEMONSTRATOR Neutrino 2022*, Seoul, South Korea (poster). 2022.
102. Wiseman, C. *The lowest radiation environments in the Solar System* CENPA Seminar. 2023.

Ph.D. degrees granted

112. MacCoy, B. *Beam Dynamics Challenges in the Muon $g-2$ Experiment* PhD thesis (University of Washington, Department of Physics, June 2023).
113. Hostiuc, A. *Search for Neutrinoless Double Beta Decay Using the Full Majorana Demonstrator Dataset* PhD thesis (University of Washington, Department of Physics, Aug. 2023).
114. Shaw, E. A. *Equivalence Principle Tests and Direct Searches for Ultra-Light Dark Matter with Fused-Silica Torsion Fibers* PhD thesis (University of Washington, Department of Physics, Aug. 2023).
115. Piers, A. *Results from a 3.1 kg day Target Exposure with Skipper CCDs from DAMIC at SNOLAB and other Beyond the Standard Model Searches with Semiconductor Detectors* PhD thesis (University of Washington, Department of Physics, Apr. 2023).
116. Ruof, N. W. *Natural Radioactive Background Suppression in ^{76}Ge Neutrinoless Double- Decay Experiments* PhD thesis (University of Washington, Department of Physics, Apr. 2023).
117. Binney, H. *Precession frequency analysis for Run-2 and Run-3 of the Muon $g-2$ experiment* PhD thesis (University of Washington, Department of Physics, Apr. 2023).